Subsurface Imaging with Reverse Vertical Seismic Profiles

by

Mary L. Krasovec

B.S. Physics and Math, University of Nebraska at Lincoln

Submitted to the Earth Resources Laboratory,
Department of Earth, Atmospheric, and Planetary Sciences
in partial fulfillment of the requirements for the degree of

Doctor of Philosophy in Geophysics

at the

MASSACHUSETTS INSTITUTE OF TECHNOLOGY

June 2001

Signature of Author ....
Earth Resources Laboratory,
Department of Earth, Atmospheric, and Planetary Sciences
May 16, 2001

Certified by ....
M. Nafi Toksöz
Professor
Thesis Supervisor

Accepted by ....
Ronald G. Prinn
TEPCO Professor of Atmospheric Chemistry
Department Head

Abstract

This thesis presents imaging results from a 3D reverse vertical seismic profile (RVSP) dataset measured at a hydrocarbon bearing pinnacle reef in northern Michigan. The study presented many challenges in seismic data processing and imaging, as the survey geometry was unique in several ways.

Reverse VSP, which uses seismic sources in a borehole and receivers on the earth's surface, is fairly rare. RVSP in 3D with a random distribution of surface geophones is unprecedented. At the time this data was collected, no commercially available processing tools existed to address this geometry, so a processing scheme had to be developed.

The data processing sequence presented in this thesis, which includes amplitude corrections, first break picking, deconvolution, wavefield separation, and application of statics, takes advantage of the repeatible signature of the new downhole source (Paulsson et al., 1998). Since the data can be handled in common-receiver gathers instead of the usual common-source gathers, it can be treated like several single offset VSPs during the processing sequence. Issues related to the 3D geometry and the random distribution of the receiver array need not be addressed until the imaging step.

The generalized Radon transform (GRT) migration method of Miller et al. (1987) provides a high resolution image of a portion of the target reef at 4600 feet (1400 meters) depth. The high resolution of the image is largely due to the downhole source, which generated a high powered signal at frequencies up to several hundred Hertz. Another factor in the high resolution of the image is the success of receiver consistent model-based Wiener deconvolution (Haldorsen et al., 1994), possible because the source signature was repeatable.

Due to adverse conditions and power system failure, a large portion of the surface array did not record data. The reduced spatial coverage limits the extent of the migrated image, precluding an evaluation of the effectiveness of the random receiver spread.

The limited nature of the receiver array also caused artifacts resembling migration smiles in the image. These artifacts are partially suppressed by limiting the aperture of the migration, but this also removes dipping reflectors from the image.

To maximize the imaging capibilities of the data, a second approach complimenting the GRT method is developed. This approach, termed vector image isochron (VII) migration, removes array artifacts from the image without losing energy from dipping reflectors. This allows artifacts in the conventional image to be identified, aiding interpretation of the GRT images. VII images also show more even illumination than conventional images, although an effect similar to NMO stretching reduces the resolution of the VII image as compared to the GRT image.

The VII scheme is an extension of the GRT migration process of Miller et al. (1987), but involves forming an image which depends on the imaged plane orientation, transforming the image based on the array geometry, then finishing the GRT summation over plane orientations. The VII imaging method is derived in both 2D and 3D with the assumption that the ray paths are straight and that at least one of the arrays, source or receiver, is horizontally oriented. The surface array can have any distribution, regular or random. The other array can have any orientation in general, although this thesis assumes that it will be either another surface array or a vertically oriented borehole array. Borehole surveys in deviated wells, or in multiple wells, can be imaged with VII migration, at the cost of more computation time.

In this thesis, the VII imaging method is tested on synthetic examples as well as the Michigan RVSP data. Is is found that, when used to compliments eachother, GRT and VII images provide 3D information about the subsurface structure which far surpasses surface seismics in terms of resolution. These images are directly tied to depth, but are not limited to a slice as are crosswell studies.

The combination of the new downhole source with the processing and imaging schemes in this thesis provide a valuable new tool for the task of reservoir delineation.

Acknowledgements

First, I must thank the people of ERL who provided me with the opportunity to do this research: my advisor Nafi Toksöz, always positive and supportive, always full of good ideas, who cannot have enough nice things said about him. My pseudo-advisors Bill Rodi, Dan Burns, and Roger Turpening, who were always available to provide direction and support. Dale Morgan for his help with my general exams, and for involving me in his environmental research in the Caribbean. Many thanks go to Arthur Cheng for recruiting me to MIT-ERL, and for lending me his hockey stick, though maybe he wouldn't have if he knew where that would lead!

The ERL support staff, Liz Henderson, Sara Brydges, and Jane Maloof, keep it all running. And Sue Turbak provides a motherly ear and word of advice when it's needed.

The postdocs at ERL, Felix Hermann, Stig Hestholm, John Olson, Rama Rao, Zhenya Zhu, Bertram Nolte, and John Olson, have been a valuable source of expertise. And there are many fun and helpful grad students I've encountered in my years at ERL: Xiaojun Huang, Jonathan Kane, Youshun Sun, Oleg Mikhailov, Weiqun Shi, Elliot Ebie, Phil Reppert, Margaret Eddie, Carolyn Bischoff, Shirley Rieven, Edmond Sze, Maria Perez, Jie Zhang and Xiang Zhu.

The research in this thesis started while I was a summer intern at Schlumberger in Ridgefield, Connecticut, and would not have been possible without the guidance, expertise and support of Richard Coates, Jakob Haldorsen, Doug Miller, and Micheal Schoenberg.

Other people who have had valuable input to my education are Ken Tubman, Melanie Marquardt, and Arcangelo Sena, who I worked with at ARCO.

Then there's all the people who keep me sane outside of school: my friends Alisyn, Nicole, Alisha, Rich, Lara, Kate, Rick, and Adam. The MIT women's hockey club and the MIT pottery studio deserve many thanks for putting the fun in grad school (yes, it's in there!), as well as making it last much longer than it might have.

And finally, my fabulous family: mom and dad, otherwise known as Tom and Ruth, my sister Karen, and nephew Josh, who have always been supportive and loving, even when I'm at my stressed out worst.

Contents

Chapter 1

Introduction

1.1 Overview

1.1.1 The contributions of the thesis

Many geophysical applications rely on high resolution seismic imaging of the earth's interior: petroleum exploration, development of geothermal resources, earthquake location, and near surface mapping of pollutants, to name a few. The portfolio of tools available for such characterization of the near surface has been recently expanding, especially within the petroleum industry where imaging goals have shifted from the identification of new targets to the development of known reservoirs. This thesis embodies a new approach in seismic reservoir delineation which allows for high resolution subsurface imaging.

In order to increase resolution, it is desirable to put either the source array or the receiver array in a wellbore. The decreased distance traveled by the seismic energy means less attenuation of high frequencies resulting in more detailed images. On the down side, these images tend to cover only a small portion of the desired target. The location of illuminated areas depends on the structure of the subsurface, and images produced with borehole seismic data tend to have artifacts caused by the limited illumination of the borehole seismic array. This thesis proposes a method of recognizing and minimizing array artifacts by accounting for the survey geometry, which in turn increases the extent and quality of the image. These techniques are applied to a reverse vertical seismic profile (RVSP) attained at MIT's Michigan Test Site.

1.1.2 The structure of the thesis

Chapter 1 describes the place of this research in the field of seismic imaging. For those unfamilar with VSP, the basics of borehole seismic methods are discussed and compared to surface seismics. There is also a discussion of the development of VSP methodology in the published literature.

Chapter 2 shows the pre-migration processing steps applied to the Michigan data. Although borehole seismics have been in use for at least 30 years, many of the techniques involved are still being developed. Recent advances in field methods, such as those which lead to the field data used in this thesis, require processing techniques which are not currently available in commercial seismic data processing packages. The processing scheme presented in Chapter 2 handles VSP or reverse VSP data. Given a distribution of downhole stations, which need not be regular, this scheme can work with any geometrical distribution of surface stations: regular or irregular distributions for 2D or 3D datasets. Special attention is paid to first break picking, deconvolution, and statics corrections, as these steps have contributed greatly to the quality of the final image.

Chapter 3 derives the new imaging process, and illustrates the method with several synthetic examples.

Chapter 4 is a detailed look at the images produced with field RVSP data. The field data was collected in Manistee County, Michigan in December 1998, a part of a research program funded by MIT-ERL's Reservoir Delineation Consortium headed by Roger Turpening.

Chapter 5 contains conclusions and plans for future work.

Appendix A summarizes the geology of the Michigan test site, MIT's prior research projects there, and the motivation for the 1998 research program.

Appendix B describes the method used to find the traveltimes for the migration of the Michigan field data.

1.2 A review of VSP imaging

1.2.1 The advantages of VSP

The petroleum industry gains knowledge of the earth's structure predominantly through downhole measurements (well logs) and seismic studies with source and receiver arrays both located on or near the surface. Well logs provide ground truth directly tied to depth, while surface seismics contain lower resolution information, often in 3 dimensions, as a function of time. Structures identified with well logs can be tied to events on surface seismic images, then mapped away from the borehole.

However, it is often difficult to tie well logs to surface seismic images because the measurements are made on such greatly different scales. Synthetic seismograms used in tying well logs to seismics are calculated by convolving a seismic wavelet with a reflectivity series developed from the well logs (and, if available, from checkshots); the resulting synthetic trace may vary greatly depending on how the well logs are blocked and what frequency wavelet is used. More importantly, small scale structures, such as layer pinchouts and fractures which allow fluid flow between reservoir pockets, are often lost in the lower resolution of surface seismic data. In fact, the whole reservoir may be thinner than the seismic wavelet. Clearly, a higher resolution method is needed, and needed in 3 dimensions.

The most obvious way to increase seismic resolution is by decreasing the seismic wavelength. Downhole seismic methods, such as vertical seismic profiling (VSP), involve a shorter ray path than surface seismics, meaning less attenuation of the higher signal frequencies. The use of VSP as a 3D imaging tool has often been proposed in the literature, and studies performed on synthetic 3D VSP data (Chen and McMechan, 1992) have been promising, but there have not been many published field results to support this. In practice, processing and imaging with 3D VSP data has proven difficult: quality field data are rare, the necessary computational tools are not commercially available, and field experiments are costly.

Because of the these difficulties, 3D VSP surveys do not contribute as much as they could to the task of reservoir characterization. The industry relies most heavily on surface seismics, well logs, and checkshot surveys, while VSPs, offset VSPs, and 3D VSPs remain secondary. It is hoped that the results presented in this thesis are part of a trend towards branching out into new methods.

1.2.2 Terminology

Checkshot surveys were among the first applications of geophysical techniques to the exploration of the subsurface, and developed into VSPs in the 1950s. Checkshot surveys are used to form velocity models of the earth from the arrival times of vertically propagating seismic waves, as shown in Figure 1-1. This provides an important tie between well logs and surface seismics, since checkshots use the same kind of source as surface seismics, but are directly tied to depths in the earth (Hardage, 1985).

Vertical seismic profiling (VSP) is the general term for seismic studies where seismic sources are located on or near the surface of the earth and receivers are placed at various depths in drilled wells (Kennett et al., 1980).

In general, VSP surveys differ from checkshot surveys in that they extract information from the entire wavetrain, and not just the first break times. VSP usually involves a smaller separation between downhole receivers than checkshots, meters or tens of meters as opposed to hundreds of meters.

Checkshot sources must be located close to the wellhead in order for the ray paths to be vertical; however, tube waves are generated when surface (Rayleigh) waves are incident on the wellhead, and may mask reflected and shear wave energy, posing a serious problem in VSP applications. Therefore, VSPs usually have sources offset some distance from the wellhead.

In the early days of borehole seismics, when there could be only a single downhole receiver, VSP surveys could be sorted into two classes: offset and walkaway.

Offset VSPs have one source located some distance from the wellhead to decrease tube wave noise and to illuminate regions of the earth away from the wellhead. Each downhole receiver station is referred to as a *level*, so OVSPs can be thought of as multilevel and single source, as shown in Figure 1-2. OVSP is usually used for land surveys, where the total number of shot locations is limited by expense or logistics (Hardage, 1985).

Walkaway VSPs, as shown in Figure 1-3, deploy a receiver in the well and an array of shots on the surface. WVSPs are used in both land and marine environments, but are most common in the marine environment for practical reasons: the ease of multiple airgun shots and the difficulty of shooting repeatedly in a stationary position while the downhole receiver is repositioned, which would be required for an OVSP (Hardage, 1985).

As field technology improves, VSP studies are tending toward *multioffset OVSP* or *multilevel WVSP*; the two classes expanding to the desired case of both multiple shots and multiple receivers.

Throughout the remainder of this thesis, the term *VSP* will refer to any OVSP or WVSP configuration, or a combination of the two.

Reverse VSPs (Jackson et al., 1989) places sources in the wellbore and receivers on the earth's surface, as in Figure 1-4. RVSP field data has been rare because of the lack of sources which can operate in the downhole environment without damaging the wellbore. The benefits and drawbacks of RVSP will be discussed later in this chapter.

Throughout this thesis, the term *borehole seismic* will be used when speaking generally of both VSP and RVSP (as opposed to surface seismics).

Seismic while drilling (SWD), which involves using the drillbit as the RVSP seismic source (Haldorsen et al., 1995), (Aleotti et al., 1999) was introduced in the 1990s. This is the strongest possible source to use for RVSP, since any other downhole source cannot actually break rock. SWD is extremely cheap, requiring less rig time than other borehole seismic methods. However, the resolution is limited because of the attenuation of drillstring vibrations, making the source signature difficult to measure: SWD is also limited because it is not effective in deviated wells, in soft formations, or for some drillbits.

Reverse VSP has not been as common in the literature as VSP, so a few of the common terms used in the handling of borehole seismic data cannot be used. For instance, the main signal wavefields of VSP data are commonly referred to as the *upgoing* and *downgoing* fields. However, with RVSP data all measured body waves are upgoing. The terms initially downgoing and initially upgoing are more applicable to RVSP, but unwieldy and misleading. In this thesis the terms *direct field* and *reflected field* will be used, where the direct field is understood to contain all initially upgoing energy which arrives at the receiver as P waves, including multiples of the direct first arrival.

Figure 1-5 shows the raypath differences between the direct and reflected wavefields. The direct wavefield has the dashed paths, the reflected wavefield follows the solid lines. Figure 1-6 shows synthetic RVSP data generated in a flat layered earth. The direct wavefield contains all energy which is parallel to the first breaks, including the direct arrival and its multiples.

1.2.3 Borehole seismics versus surface seismics

A comparison of borehole seismics to surface seismics must take into account the different uses of the two methods.

Surface seismics are used for mapping large scale structure, identifying new targets, and characterizing reservoirs. (Yilmaz, 1988) Surface seismic wavelengths are generally in the range of a hundred to a thousand feet, (tens to a few hundred meters) with smaller wavelengths lost due to attenuation. This limits the detail that can be resolved with surface seismic data, especially for deep reflectors.

The early role of borehole seismic surveys was to support surface seismics by identifying reflectors and multiples, estimating seismic wavelet behavior, and providing a depth tie between well logs and surface seismics. More recently, borehole seismics are becoming tools for reservoir delineation, producing high resolution images over relatively small zones of illumination.

One of the obvious advantages of borehole seismics is the shorter ray path from source to reflector to receiver, which means less attenuation and a smaller Fresnel zone than surface seismics. In addition, the seismic energy passes through the surface weathering layer only once, so that static traveltime errors, attenuation, and shallow multiples are less severe. Downhole seismic data generally has wider scattering angles than surface seismics, which ideally means there is more rock property information in VSP data than in surface seismics. In practice, the nature of the raypaths involved makes it difficult to extract this information. In fact, the raypath geometry of borehole seismics is an additional difficulty to be addressed to the imaging process.

Downhole surveys also have the disadvantage of limited spatial and dip illumination. Exampes in Chapter 3 and fold maps in Chapter 4 will show that even with a large, dense receiver spread, fold coverage is uneven, leading to difficulty in recovering true amplitudes. This is especially problematic where the downhole array is close to the subsurface target.

1.2.4 VSP versus RVSP

A comparison between VSP and RVSP could best be made by producing 3D VSP and RVSP datasets with geometrically identical borehole and surface arrays, an experiment which, to the author's knowledge, has yet to be performed. (Chapter 5 contains a discussion of planned future field work at the Michigan Test Site which will allow such a comparison.) The major differences between the datasets would include ambient noise, source coupling, tube wave noise, and the use of 3 component data.

In general, VSP surveys have little ambient noise because the receivers are located far from the surface of the earth, and source power is usually not an issue. RVSP, on the other hand, places receivers in a noisy environment on the earth's surface, and the source power is limited because the borehole must not be damaged. RVSP does have the advantage of better source coupling, since with VSP the source is often located in shallow, poorly consolidated sediments.

VSP studies suffer greatly from tube wave noise. In the past, RVSP sources have also generated tube waves, but new sources which do not move the borehole fluid, such as the vertical vibrator used to generate the data in this thesis, likely cause minimal tube waves. If this is true, RVSP could solve the biggest noise problem faced by borehole seismic studies.

VSP has advantages which come with multicomponent data. Downhole receivers often must be 3 component because the wellbore is not ideally vertical, and the incident body waves may be propagating nearly horizontally. This means the VSP data can be separated into compressional and shear wavefields, not only increasing imaging capabilities but determining medium velocities (Esmersoy, 1990), anisotropy (Ahmed, 1990) or even reflector dip from hodogram analysis (Spencer et al., 1988).

RVSP studies can make use of shear wave information, both direct S wave arrivals and converted waves, by using multicomponent geophones. However, ray paths at the surface of the earth tend to be nearly vertical because of the low velocities of shallow sediments, making the use of multicomponent data for hodogram analysis impractical.

In any case, a direct comparison between VSP and RVSP would require a 3 component downhole source to reciprocate a 3 component VSP survey, and such sources are rare.

As for illumination issues, if the arrays in the VSP and RVSP studies are indeed identical, then their subsurface illumination should be identical. However, practical issues often limit the extent of the source and receiver arrays. Payne et al. (1994), uses synthetic data to show that multiple surface stations are necessary to optimize subsurface illumination. This is not a surprising result, as illustrated in Figure 1-7: a ray diagram of single shot VSP versus a single shot RVSP. Since shots are more expensive than receivers, RVSP has a more desirable ratio of illumination-to-cost.

The above qualitative comparison of VSP and RVSP is difficult to substantiate because there have been few direct field comparisons of VSP to RVSP. Zimmerman and Chen (1993) compared VSP to RVSP, using surface dynamite sources with downhole geophones and hydrophones to collect two VSP datasets. The RVSP data was generated with surface geophones and downhole dynamite sources, which generate problematic tube waves. They found that the RVSP source saw higher frequency signals, (40-240 Hz, versus 15-110 Hz for the geophone VSP, and 60-160 Hz for the hydrophone VSP.) but the "geophone VSP stacked section produced an interpretable subsurface image at much greater depths" than the other data. They conclude that "if a high-powered, nondestructive source is developed, RVSP could be a practical alternative to VSP."

1.3 Units

The petroleum industry tends to use British units, and the Michigan research program, being planned and executed by people with petroleum backgrounds, is most conveniently described in feet and feet/second. Corresponding values in SI units will be given whenever possible, and Figure 1-8 provides a table to convert most of the basic numbers of importance in this research.

1.4 VSP development in the literature

The following is a brief discussion of the development of borehole seismics in the literature. Much of this discussion has been taken from Hardage (1985).

The first documented application of VSP was a patent by R. A. Fessenden in 1917, which is usually chosen as the starting point for the development of borehole seismic measurements into present day VSP (Hardage, 1985). Barton (1929) built on Fesseden's work, describing further uses of seismic measurements in boreholes. McCollum and Larue (1947) suggested that geological structures could be mapped by measuring traveltimes from surface sources to receivers located in boreholes. Despite these papers, the major use of seismic studies in boreholes remains the measurement of seismic velocities, mainly checkshot surveys which use only first break arrival times to calculate apparent velocity between receivers at different depths.

Papers by Jolly (1953), Riggs (1955), Lynn (1963) and Levin and Lynn (1958) brought attention to the information content of the full geophone response. They showed that much could be learned from the recorded reflections and multiples, and not just the first break arrival times. These papers developed most of the fundamental concepts used in VSP today.

Geophysicists in the former Soviet Union took to VSP in the late 1950s, with a vigorous program of borehole seismic studies over the next 20 years as documented by Galperin (1974). Geophysicists in the Western hemisphere, however, showed little serious interest in VSP until the late 1970's.

At this time, support for VSP by non-Soviet geophysicists was led by Anstey (1980), Balch et al. (1982), Kennett et al. (1980), and Omnes (1978). The late 70s also saw an outburst of patents covering VSP and RVSP technologies such as geophone designs, borehole energy sources, proposed field geometries and exploration ideas (Hardage, 1985).

This lead to a resurgence of VSP in the Western hemisphere in the form of technical conferences and continuing education courses in the early 1980s. The issues of discussion at this time included the acquisition and processing of 3 component VSP data, fracture detection, seismic attenuation, and shear wave interpretation. These meetings raised the industry's awareness of VSP as a tool, and resulted in an increase in the number of VSP experiments done by non-Soviet petroleum companies.

The 1980s saw the development of many of the current VSP processing tools, such as wavefield separation techniques by Suprajitno and Greenhalgh (1985), Moon et al. (1986) and Aminzadeh (1986), and methods of detecting reflectors and their orientation, such as Disiena et al. (1981), Spencer et al. (1988), and Dillon and Spencer (1988). Shear wave separation and processing techniques were developed by Knecht and Edelmann (1987), among others.

VSP data has the potential to alleviate the difficulty of shear wave processing and imaging. With surface seismics, it is difficult to identify the source of P to S converted waves. VSP provides snap shots of the wavefield in the earth, allowing P and S waves recorded at the surface to be traced back to the reflectors that caused them. Papers that deal with shear waves are Gut et al. (1994) for discussion of shear wave sources and Meadows and Winterstein (1994) for an example of shear wave data used to detect a hydraulic fracture.

Because VSP seismic events can be directly tied to depth, inversion for velocities and other parameters such as attenuation and dispersion is a good method of developing and improving earth models, which in turn can be applied to the processing of surface seismics (Johnstad and Ahmed, 1991). A great number of VSP papers in the 1980s to the present have dealt with the inversion of VSP traveltimes for rock properties. Many of these methods use only the first break arrival times, basically applying advances in computing and data quality to the checkshot methodology.

Another application of VSP which has received attention in the literature is imaging. One of the first VSP imaging methods was the VSP-CDP transform of Wyatt and Wyatt (1981) or later versions by Dillon and Thomson (1984) and Chen and Eriksen (1988). However, it wasn't long before surface seismic prestack migration techniques were adapted to VSP, which will be discussed in Chapter 3 of this thesis.

Since the resurgence of VSP in the 1970s, it has been greatly limited by the hardware available. Early VSP studies could have only one receiver in the well, so each level required a separate surface shot. This results in great expense in aquiring the data, as well as problems with data processing, as the shot signature could vary for each trace. In the late 80s receiver strings became available, but still only allowed 2-3 levels per shot. Cutting edge wireline VSP receiver strings in the year 2001 don't go above a dozen levels while tubing conveyed receiver strings go up to 80 levels of three component receivers (240 channels).

The important issues of VSP have not changed drastically in recent years. Despite advances in computing power and the great number of tools introduced for processing, imaging, and interpreting multicomponent, multilevel, multioffset VSP data, the field data results have not shown the drastic improvement that has been seen in surface seismics and other geophysical methods over the past few decades.

The data presented in this thesis, however, shows that advances in borehole seismic hardware and field methods are now leading to higher quality 3D borehole seismic data than has been seen before. The high frequency content, power, and repeatability of the source yields images of unprecedented resolution.

However, the limited aperture of the array causes artifacts which make the image difficult to interpret. The following chapters of this thesis present an imaging method which may solve this problem, making borehole seismics a more effective tool for 3D imaging.

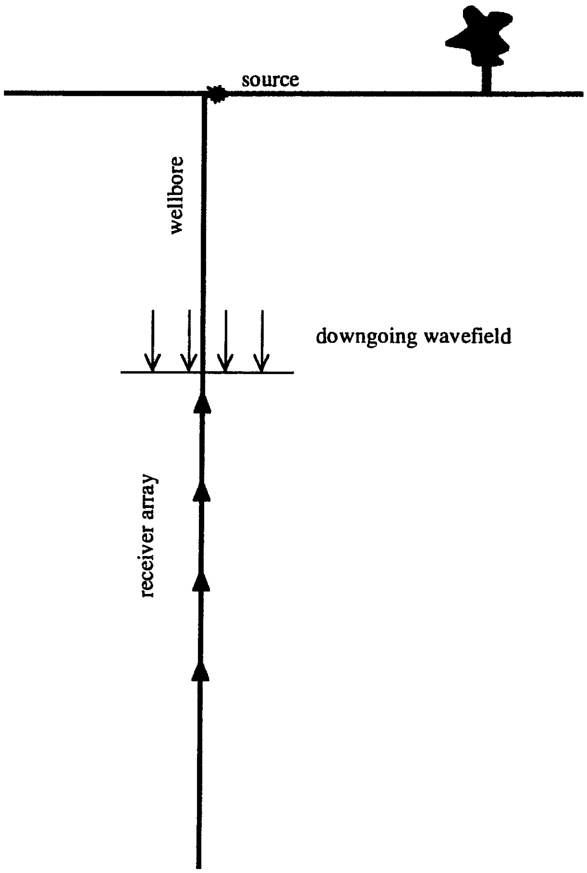

Figure 1-1: Checkshot survey. The velocity is calculated by dividing the distance between receivers by the difference in arrival times of the first breaks.

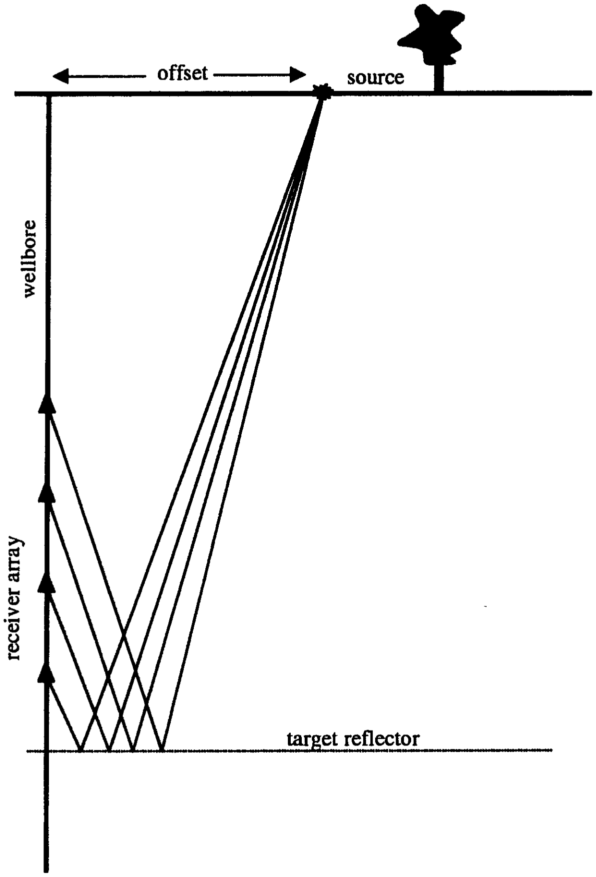

Figure 1-2: Multilevel offset VSP. The downhole receivers tend to be more closely spaced than they would be in checkshot surveys.

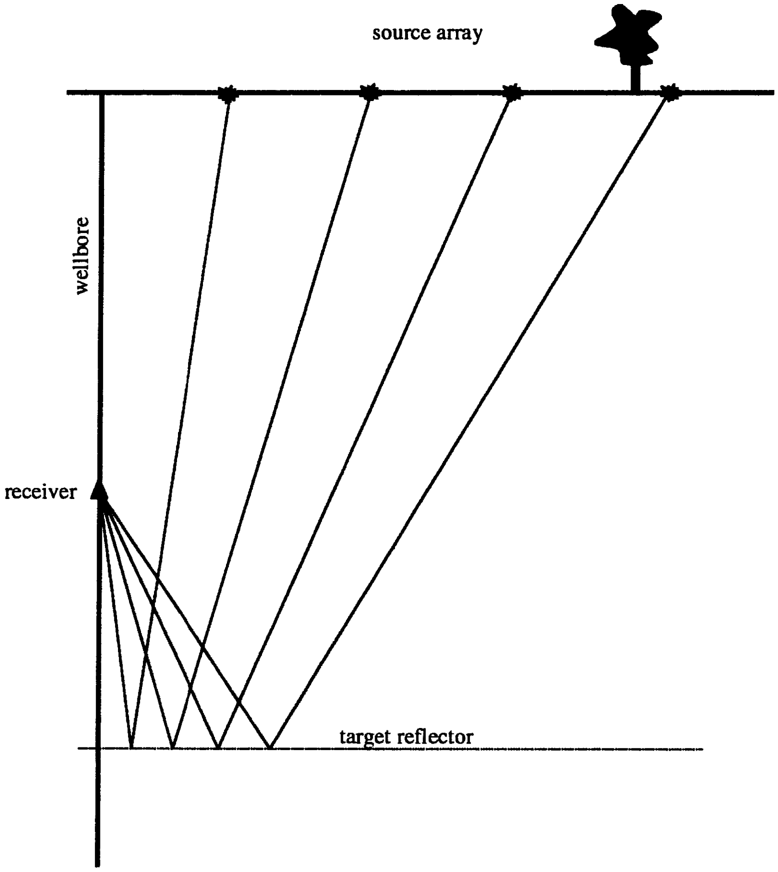

Figure 1-3: Walkaway VSP. These are most practical to do in marine environments.

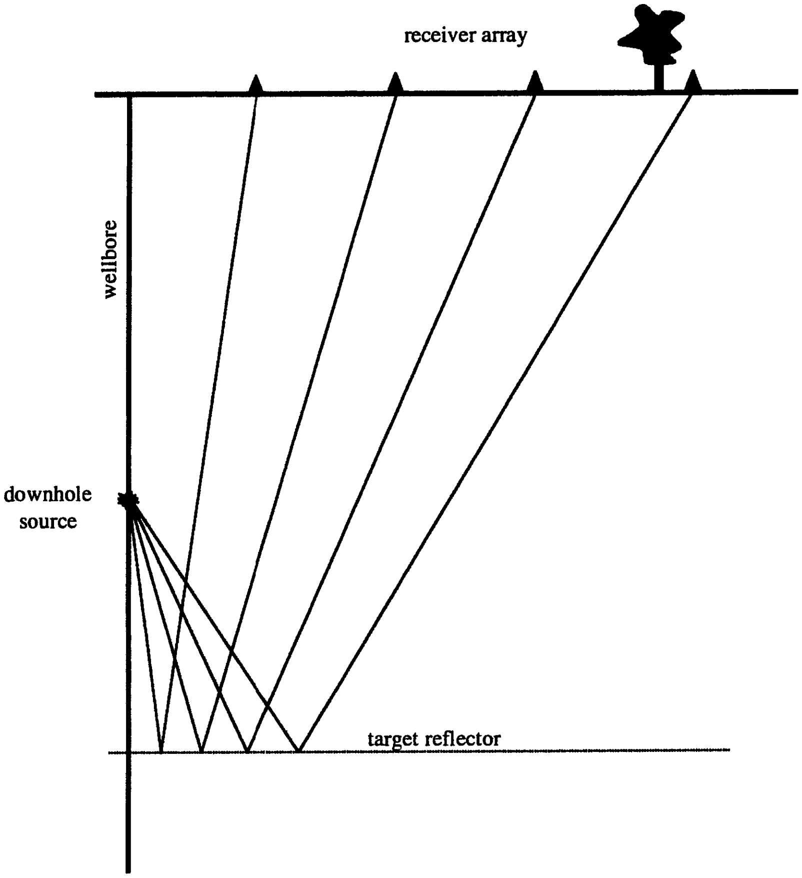

Figure 1-4: Reverse VSP. This survey geometry has been uncommon because a high powered source could damage the wellbore.

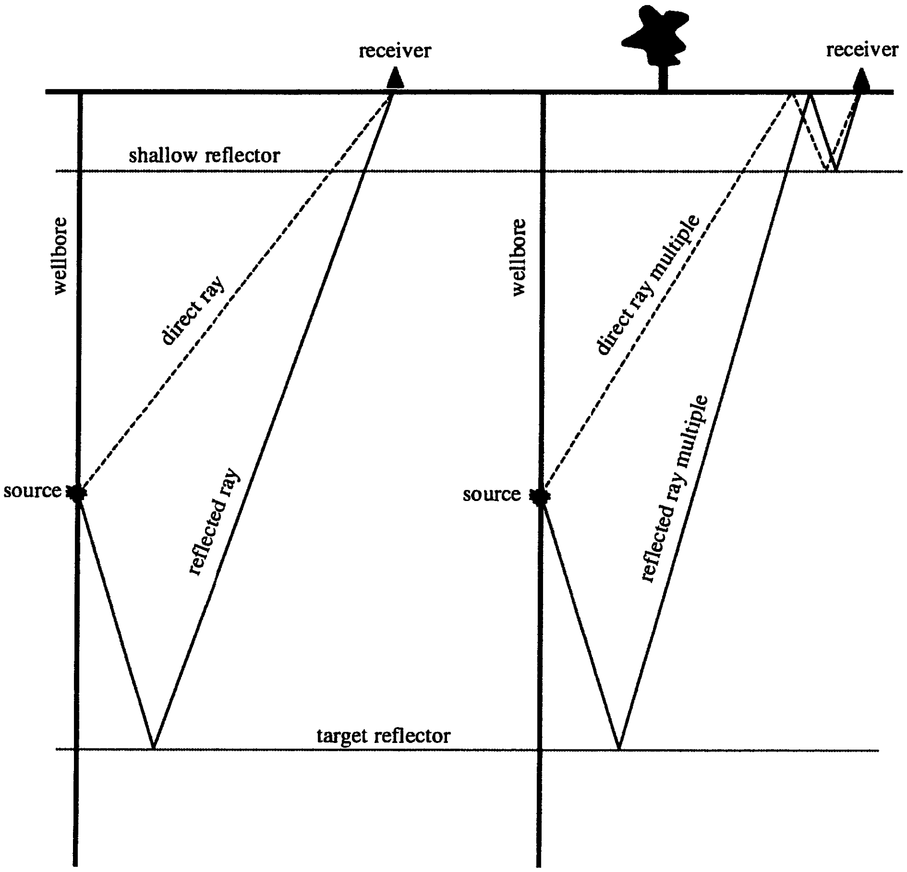

Figure 1-5: Direct field and reflected field ray paths and multiples.

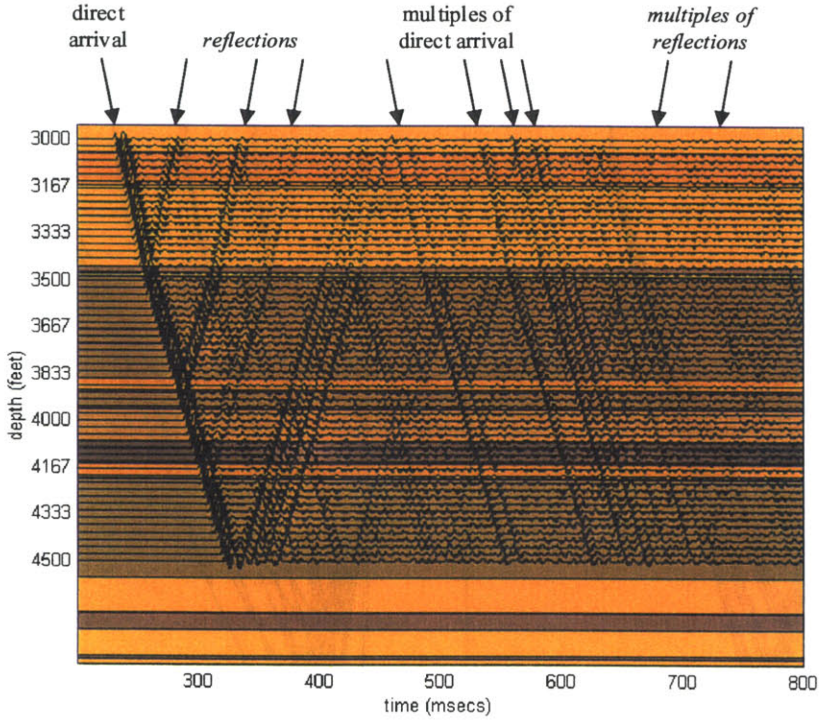

Figure 1-6: Synthetic data generated by the flat layered model shown in the background. The direct field includes the direct arrival as well as its multiplies.

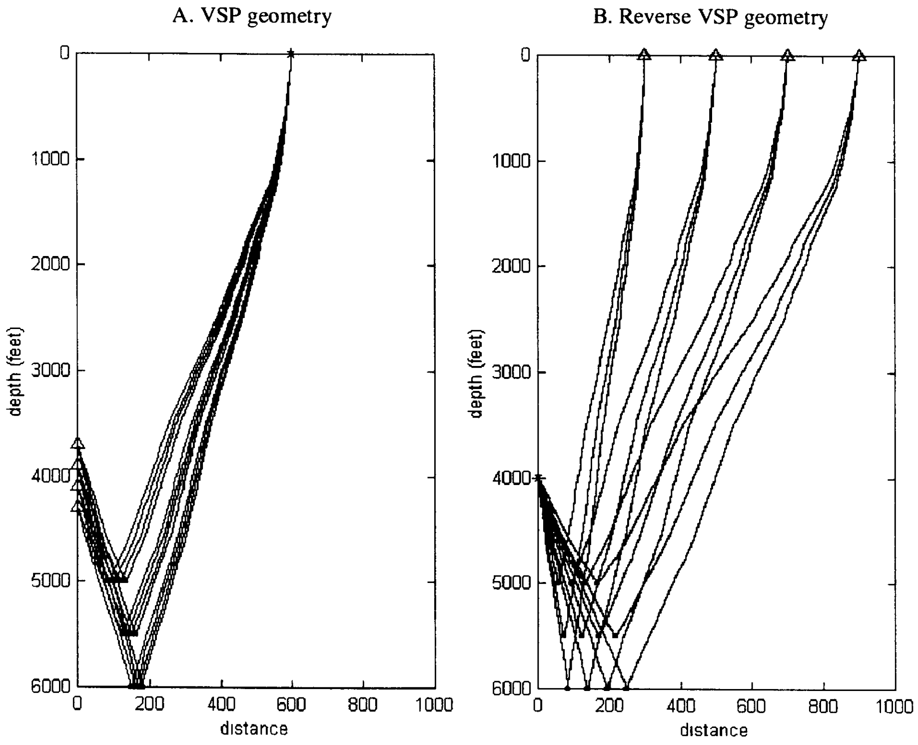

Figure 1-7: Illumination of VSP versus RVSP. In both plots the receiver spacing is 200 feet. The Reverse VSP reflection points cover a larger portion of the subsurface.

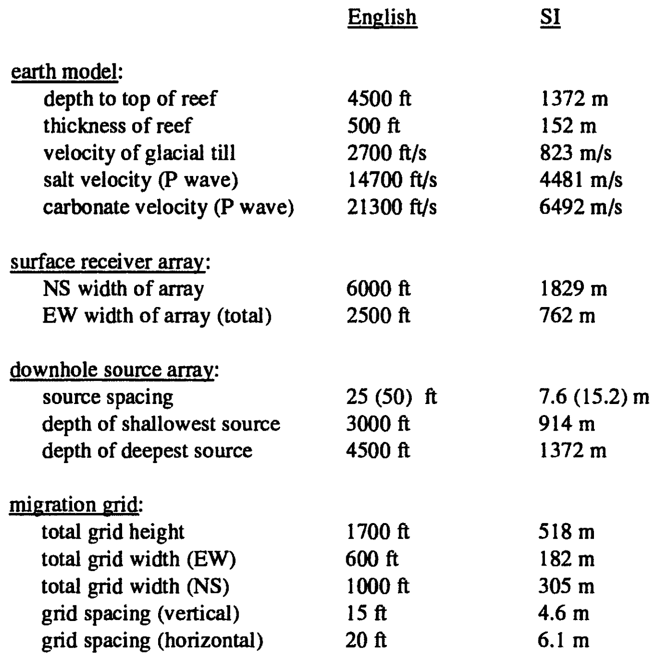

	English	SI
earth model:		
depth to top of reef	4500 ft	1372 m
thickness of reef	500 ft	152 m
velocity of glacial till	2700 ft/s	823 m/s
salt velocity (P wave)	14700 ft/s	4481 m/s
carbonate velocity (P wave)	21300 ft/s	6492 m/s
surface receiver array:		
NS width of array	6000 ft	1829 m
EW width of array (total)	2500 ft	762 m
downhole source array:		
source spacing	25 (50) ft	7.6 (15.2) m
depth of shallowest source	3000 ft	914 m
depth of deepest source	4500 ft	1372 m
migration grid:		
total grid height	1700 ft	518 m
total grid width (EW)	600 ft	182 m
total grid width (NS)	1000 ft	305 m
grid spacing (vertical)	15 ft	4.6 m
grid spacing (horizontal)	20 ft	6.1 m

Figure 1-8: Unit conversions of the more relevant values in the thesis.

Chapter 2

The Reverse VSP Data Processing Sequence

2.1 Introduction

This chapter discusses the processing steps applied to the reverse vertical seismic profile (RVSP) data collected at the MIT Michigan Test Site in Manistee County, Michigan. The RVSP data was part of a larger research program shot in December, 1998 (Turpening, 1995). The program, headed by MIT-ERL's Roger Turpening (now at Michigan Technological University) and funded by the MIT Reservoir Delineation Consortium, provided a field test of the new Paulsson downhole source (Paulsson et al., 1998).

Other goals of the program were to test the feasibility of using randomly located arrays, to define field methods necessary for the deployment of such arrays, and to develop algorithms for the processing and imaging of random 3D RVSP and surface seismic data. The details of the fieldwork and hardware, as well as discussion of the geology of the test site and the results of previous studies, are left to Appendix A.

The RVSP dataset used in this thesis presents some unique challenges: it is a three dimensional borehole seismic survey with random surface geophone locations. The processing of 3D borehole seismic data is a wild card in itself, with no such processing tools commercially available. The reverse geometry means that even existing 2D VSP processing steps can't be blindly applied, and the random geometry of the surface spread is a formidable complication.

Figure 2-1 shows the processing sequence which has been developed for the Michigan RVSP data. The sections in this chapter cover the particulars of each processing step. It will be shown that the downhole source gave a repeatable signature, making it possible to process the data in receiver gathers with common VSP processing steps. In addition, the spatial sampling is nearly regular in the common-receiver domain, so the effects of the incomplete random spread need not be addressed during the pre-migration processing of the data.

Vibroseis deconvolution and receiver group summing were done in the field. The source swept from 1 to 360 Hertz in 12 seconds: the vibroseis signature was deconvolved in the field. The receiver stations were groups of nine receivers spread in a square about 5 feet (1.5 meters) on a side. This grouping was intended to strengthen the signal and minimize random noise; low frequency surface waves were not attenuated by this receiver group stacking.

2.2 Survey Geometry

Figure 2-2 is a map of the planned geometry of the 1998 RVSP. The red triangles are source locations for the 3D surface seismic, which was recorded with the same receiver spread as was used for the RVSP. The receiver stations are black dots; the colored lines show the cable layout. The heavy black line is a creek, which had to be included in the planning because the cables could not be allowed to cross it.

The receivers were connected into 8 "lines" as indicated by the cable colors on Figure 2-2. Adverse conditions led to battery failure in the receiver spread, so that only 3 of the planned 8 lines were in operation (lines 6, 7 and 8). Of the 828 planned receivers, 275 recorded enough data to be useful. The resulting receiver spread has a crescent shape, shown in Figure 2-3.

The reef is approximately circular, located between the Stech and the Burch wells as shown in Figure 2-3. The producing well, owned by Shell, is located over the center of the reef. Appendix A contains a discussion of the Test Site and the results of previous MIT studies.

The downhole sources for the RVSP were located in the Stech well, just off the eastern edge of the reef. There were a total of 50 shots, at a 25 foot spacing from 3000 to 4000 feet depth and 50 foot spacing from 4050 to 4500 feet. The shot level at 4300 feet was skipped because of concerns with the well casing.

2.3 Trace sorting

Often, seismic data is processed in common-shot gathers, since the signature of the shot can vary. With the Michigan RVSP data, it was preferable to work with common-receiver gathers for several reasons. In general,

- Reflected body waves are more easily separated from direct arrivals.
- When sorted into common-receiver gathers, RVSP data can be processed using existing VSP processing tools. The only possible difficulty is that the data needs to be transformed to correct for polarity according to the types of sources and receivers which were used (Hokstad et al., 1998).
- Issues relating to the 3D geometry need not be addressed until the imaging process, since the data can be treated as if it were many individual offset VSPs.

In particular for the Michigan RVSP data:

- Ground roll noise caused by the source support equipment is randomized in common-receiver gathers.
- Deconvolution on common surface station gathers is preferable because the seismic wavelet appears to depend primarily on "ringing" in the near surfaces layers, and not on the signature of the source itself.
- The downhole spatial sampling is regular, while the surface array is highly irregular. For example, applying an FK filter to a common shot gather of this data would be difficult.

At the time that the RVSP data was collected, it was not known whether processing the data in the common-receiver domain would be made difficult by a varying source signature. The results of the deconvolution, shown in Section 2.7, laid this question to rest.

Figure 2-4 is every other trace in a single shot gather of the raw data, sorted along the cable lines. The first break is visible at between 280 and 380 milliseconds, depending on the receiver offset. Coherent low frequency noise is obvious, especially where the traces are close to the wellhead. This noise will be discussed in Section 2.6.

Figure 2-5 are single receiver gathers of the data, for the two receivers marked on the field map in Figure 2-3. The receiver 261 gather is one of the cleanest in the study and images the reef structure: reflections from about 4500 feet depth, which corresponds to the depth of the A2 carbonate overlying the reef, are clearly visible.

The bottom gather in Figure 2-5 was one of the more distant from the wellhead, and contains reflections from off reef structures as well as converted shear waves. These gathers will be used throughout this chapter to illustrate the processing sequence.

2.4 Receiver gain correction

The preamplifier gains were adjusted in the field after the first four shots. To correct for this variation, the individual recorded traces are normalized in a shot consistent basis. The power of each shot is found by averaging over all receivers in each common-shot gather, measured in a window around the first-break time. Figure 2-6 shows the power of each of the 50 shots. Figure 2-7 is a common receiver gather before and after the amplitude correction, which had already been applied to the traces shown in Figures 2-4 and 2-5.

The shots were done at 50 foot intervals as the tool was lowered into the the well, then filling in the 25 feet coming back up. This accounts for why the first four shots are every other shot station.

2.5 First break picking

To take advantage of the high frequencies present in the reflected signal, the first break picks must be as accurate as possible. The picking was done in three steps:

1. An automated process picks the maximum envelope of the traces within a 50 millisecond time window. The central time of the window depends on the source depth and the receiver distance, as estimated roughly by observing a few gathers.

2. The time picks are manually corrected for cycle skipping and errors due to noise. At this point the picks are correct to within a millisecond or two.

3. The deconvolution process discussed below allows shifts of fractions of milliseconds to optimize the deconvolution output.

Because of the low frequency noise in the gathers near the wellhead, a low-cut filter is used to block frequencies below 35 Hertz so the automated first break picking has a better chance at success. The "time pick honing" in Step 3 is carried out on the unfiltered data, to avoid error due to changes in the wavelet shape caused by the noise filtering in Step 1. The filtered data was used only to obtain the rough time picks in Step 2.

Because of research previously done at this test site, (See Appendix A), detailed models of the earth's structure in this area are available: the earth overlying the target reef is known to consist of flat horizontal layers. Therefore, the first break times could be modeled by ray tracing through a flat layered model. Comparing the modeled first break times to the first break picks allow us to check the validity of the earth model, and, as discussed in Section 2.9.2, to apply migration statics. Both the modeled and the picked first break times are shown on Figure 2-7.

2.6 Noise

2.6.1 Surface noise

Figure 2-8 is a spatial map of the semblance quality of the data interpolated from the receiver locations into a regular spatial grid. Semblance quality is calculated in the deconvolution process, which will be discussed in Section 2.7, and is a measure of signal to noise ratio.

The source of most of this noise are generator trucks near the wellhead powering the downhole source and logging equipment. The noise falls off quickly with distance from the wellhead, but in the near offset traces (less than 100 feet from the wellhead), the noise completely masks even the first breaks. The 4 receivers nearest the wellhead are abandoned for this reason.

As mentioned in Section 2.3, sorting the data in common receiver gathers randomizes the noise, making it possible to separate ground roll noise from the body wave signal in the deconvolution process.

2.6.2 Shear waves

Shear wave arrivals are clearly visible in receivers 1200 feet (360 meters) and further from the wellhead. This arrival distance corresponds to a critical P to S conversion angle for a shale-limestone interface located at about 1800 feet (540 meters) depth. For the most distant receivers, the shear arrivals become quite strong, partially masking the reflected wavefield. The processing sequence applied to this data does not address the converted waves because they cancel out in the migration summation.

Since the shape of the converted wave arrival depends on the same glacial till seen by the P wave, the deconvolution process also spikes the converted wave arrival. This suggests that the converted waves could be used as further information in the imaging process, but that is beyond the scope of this thesis.

2.7 Deconvolution

Downhole seismic data, usually checkshot surveys and VSPs, have long been used to estimate the seismic wavelet. This is possible because the direct wavefield and the reflected wavefield are easily separated for an array in a vertically oriented wellbore. The direct wavefield is used to estimate the seismic wavelet, including both the wavelet shape and raypath multiples.

There have been several variations of the VSP deconvolution step published in the literature, (Haldorsen et al., 1994), (Smidt, 1989). The model based Wiener deconvolution method of Haldorsen et al. (1994), produces excellent results by giving the deconvolution step two objectives: to spike the wavelet and to minimize energy which does not resemble the direct wavefield. The method is referred to as semblance deconvolution since it directly involves the semblance of the data gathers.

Semblance deconvolution is applied to the raw, unfiltered traces from Figure 2-5 using the first break time picks. The results are shown in Figure 2-9. The direct arrivals, both P waves and converted waves, have been collapsed to sharper wavelets. Reflected arrivals have also been collapsed into sharper wavelets.

The data in Figure 2-9 may not be cleaner in appearance than Figure 2-5, but the images that result from the deconvolved data are much better: without deconvolution, most reflectors would be masked by the ringing of earlier arriving energy. Without the ringing, resolution improves.

2.8 Wavefield separation

The last step of data processing is to isolate the reflected wavefield. There are several methods availble for wavefield separation; a median filter (Hardage, 1985) is used on the Michigan data because it works well on irregular trace spacing and high levels of noise, with little damage to the shape of the wavelets.

Figure 2-10 illustrates the method used to separate the wavefields: after the traces are aligned according to the first break times, the median filter isolates the direct field. This is subtracted from the gather. The resulting gather in Figure 2-10E shows a fair amount of energy remaining at the first break, but later events parallel to the first breaks, which would actually be more problematic to the imaging process, have been suppressed. A top mute can be used to get rid of the residual first break energy, which although this energy shouldn't affect the imaging process at all.

Figure 2-11 shows the reflected wavefields for the two gathers. Note that the converted shear wave in the bottom gather has not been removed. Given shear wave first break time picks, a median filter could used to remove these shear wave arrivals.

As discussed in Section 2.6.2, the converted wave arrivals are quite strong in the far offset receiver gathers, such as in the bottom plot of Figure 2-11. Since the converted arrivals are not coherent with the reflected wavefield, and in fact move out in the opposite direction, they will act as random noise in the imaging summation. No further processing in used to suppress them.

2.9 Statics

2.9.1 Elevation statics

Elevation statics are calculated using the receiver elevations and the near surface velocity of 2700 ft/s (823 m/s). Figure 2-12 shows the first break time picks and the elevation statics. There are a few odd spots in the picked times, especially near the wellhead where the noise was bad enough to mask the first breaks.

The early times south of the wellhead are due to a topographic low at a creek, and are corrected by elevation statics. The bottom plot of Figure 2-12 shows the elevation statics calculated from the measured elevations and the till velocity. The first break times with the elevation statics are shown in the top left plot of Figure 2-13, and are more symmetrical about the wellhead than the raw first break times.

2.9.2 Migration statics

As mentioned in Section 2.5, first break times are modeled using a flat-layered velocity model derived from previous studies at the MIT Test Site; this velocity model will be used in migrating the data. Differences between the real earth and this velocity model will lead to error in the migrated image, so a receiver consistent static shift is used to align the picked first breaks with the modeled first breaks. This shift will be referred to as the migration static correction.

Figure 2-13 shows the first break picks with the elevation static, the modeled first breaks, and the migration static found by subtracting the two. There are larger statics around the wellhead where the signal to noise ratio is low. The high statics on the northern part of the survey seem to correspond to a feature in the elevation, and are most likely due to a related structure in the near-surface weathered layer. Other than these two features, the migration statics tend to become more negative to the north. This is probably due to a slight regional tilt in the basin.

2.10 The signal spectrum

Figures 2-14, 2-15,and 2-16 show the f-k transform of the two example gathers at each of the main processing steps discussed in this chapter. The f-k transform is taken only at the shot depths above 4000 feet, where the spatial sampling is regular. Figure 2-14 corresponds to the gather in Figure 2-5, Figure 2-15 is the data after deconvolution, corresponding to Figure 2-10. Note that although no noise filtering has been used, the low frequency noise has been greatly reduced because it is not coherent with the shape of the direct wavefield.

Figure 2-16 corresponds the the gathers in Figure 2-11, with the direct wavefield suppressed by the wavefield separation step.

Figure 2-17 shows the spectrum of the direct field before and after deconvolution. Before deconvolution the 20 dB down bandwidth goes up to nearly 200 Hz, an unprecedented high frequency to get in this area where signals of 100 Hz are rare. After deconvolution, the bandwidth extends nearly to the top of the sweep at 360 Hertz. The wide notch at 200 Hertz is present in most of the gathers, and could be due to some interference pattern in the glacial till layer.

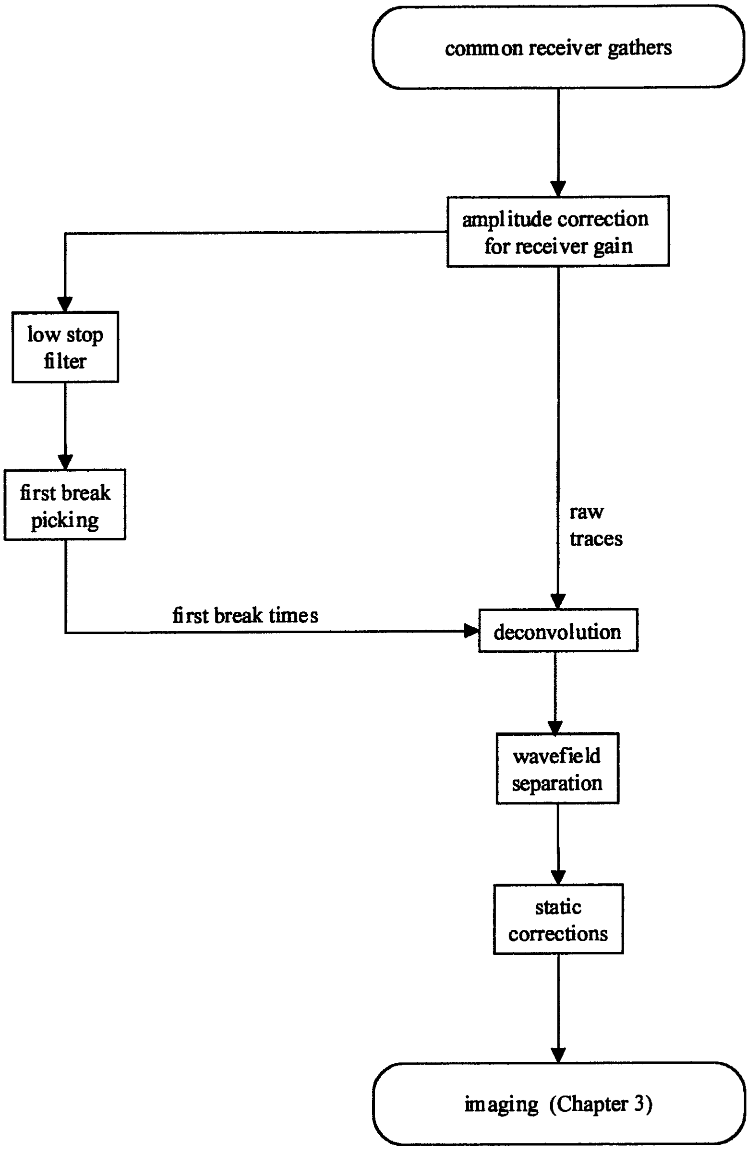

Figure 2-1: The processing scheme applied to the Michigan RVSP data.

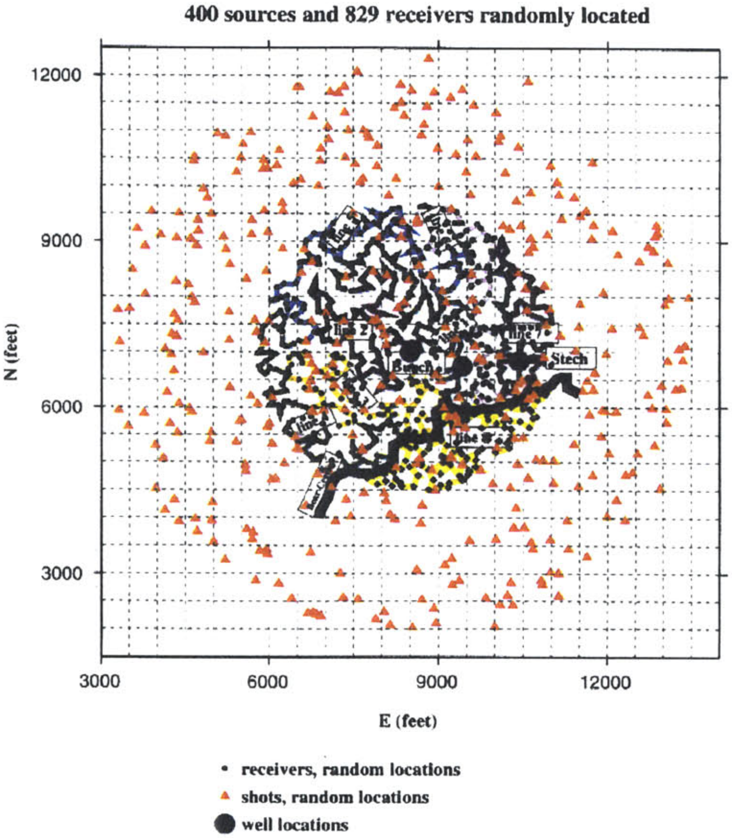

Figure 2-2: The layout of the 1998 program. The random array of shot locations from the surface seismic, which is not considered in this thesis. The sources for the RVSP data were located in the Stech well. The heavy black line is a stream, which had to considered in the cable layout.

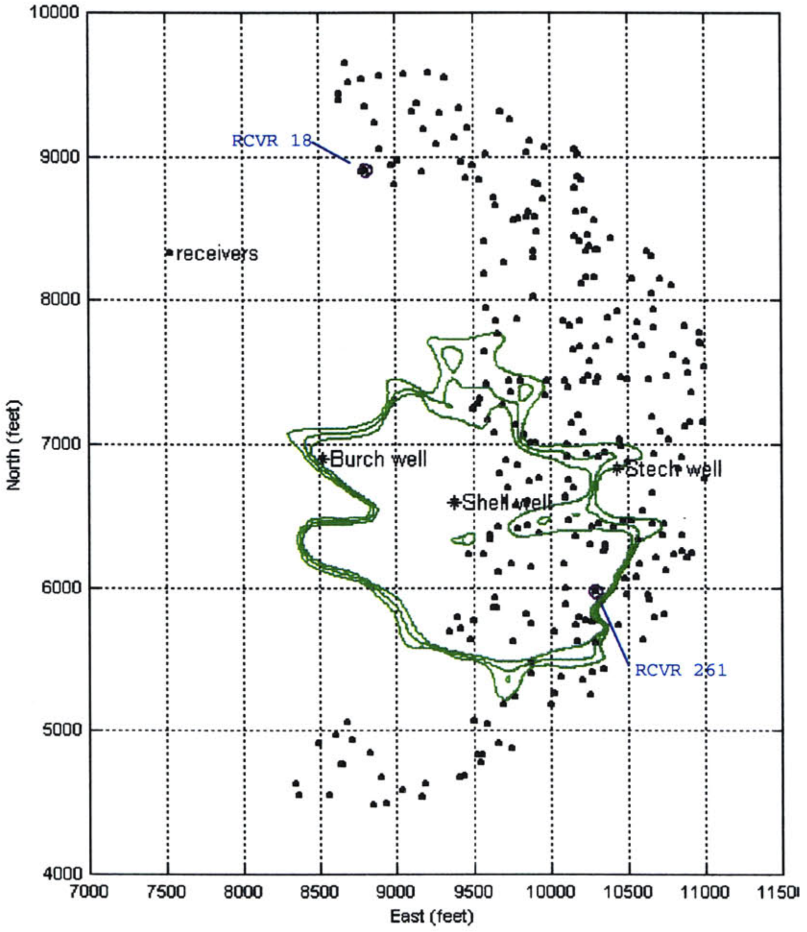

Figure 2-3: The receiver spread of the final survey, the downhole shots were in the Strech well. The contour lines are an estimation of the reef shape from 3D seismics shot in 1983. Gathers form the two indicated receivers are used throughout this chapter to illustrate the processing steps.

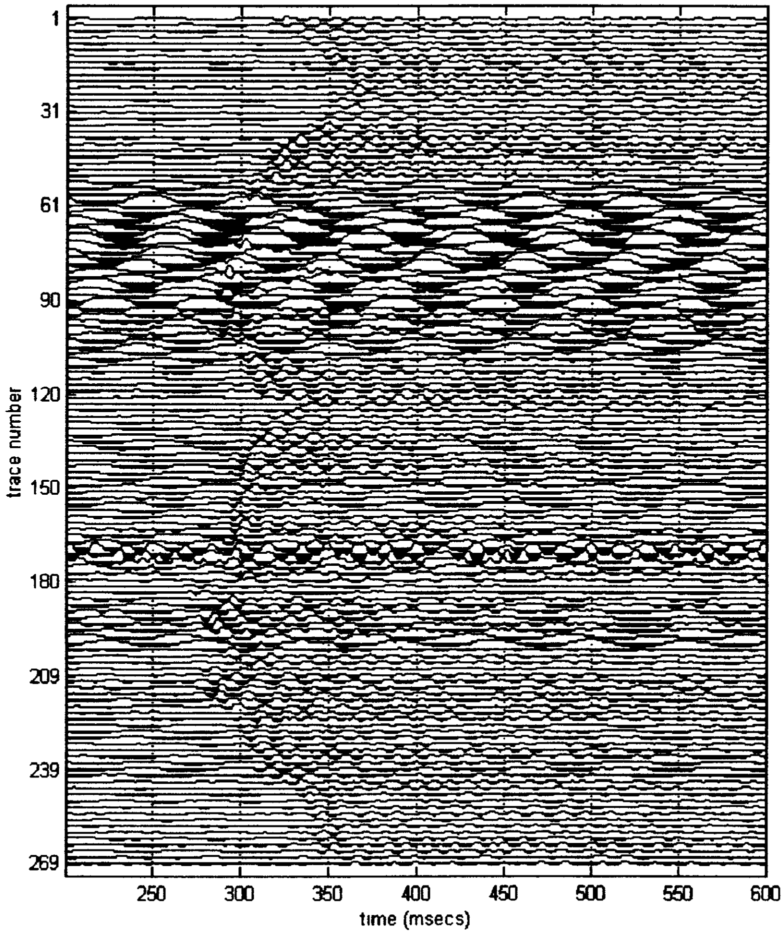

Figure 2-4: Every other trace in a single shot gather, arranged along the cables. The first breaks are visible from 280 to 380 milliseconds. The bands of low frequency energy are ground roll due to equipment near the wellhead.

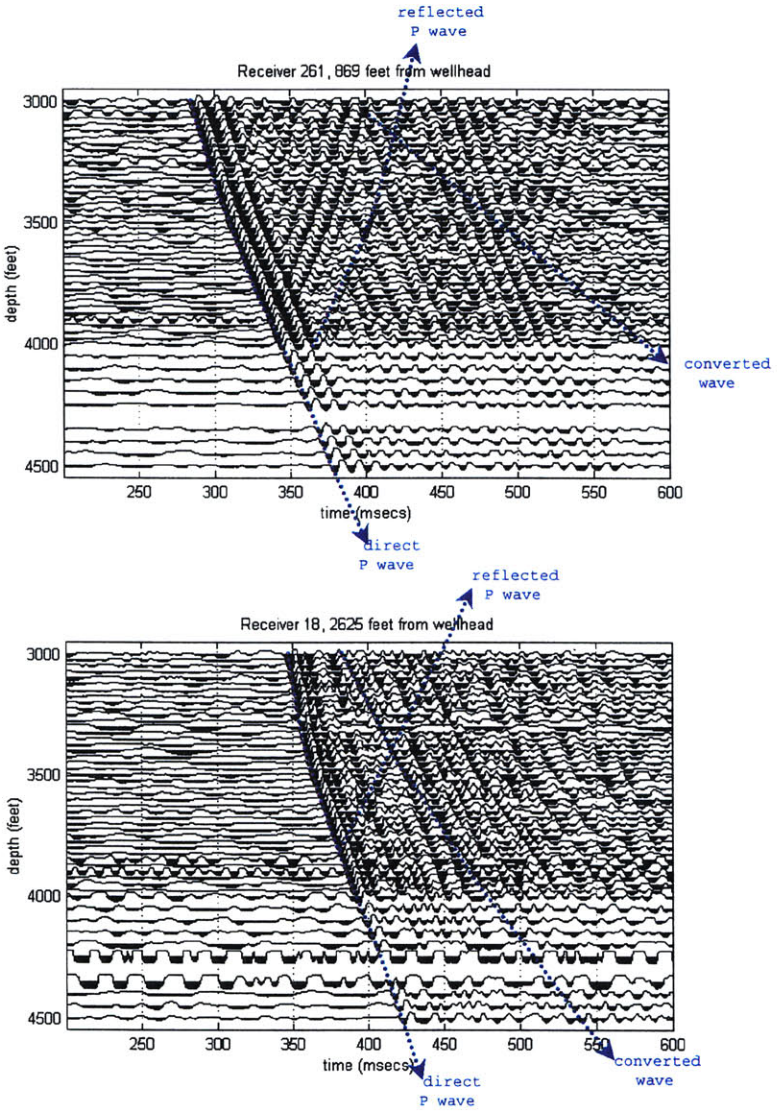

Figure 2-5: Single receiver gathers. The top plot shows one of the cleanest gathers in the survey. The bottom plot is one of the furthest from the wellhead, and has converted shear wave arrivals The noise is randomized, as compared to the single shot gather in Figure 2-4.

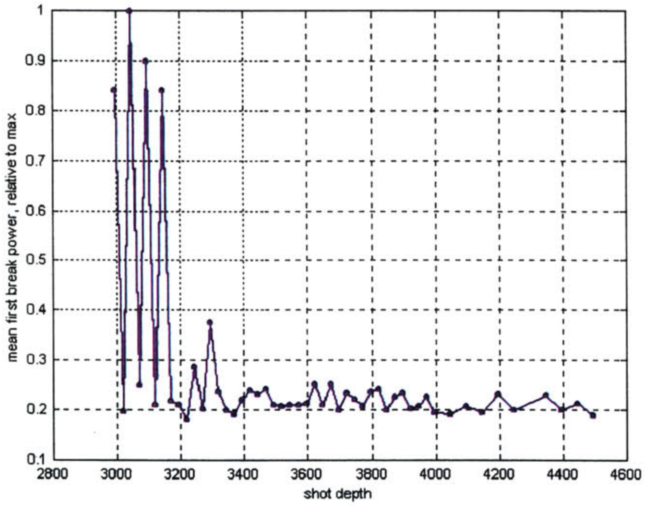

Figure 2-6: The average power of the first breaks for each shot. This is used to correct for receiver gain, which was adjusted after the first four shots. The shots were made every 50 feet going down, then filled in coming back up, which is why the first four shots are every other station in depth.

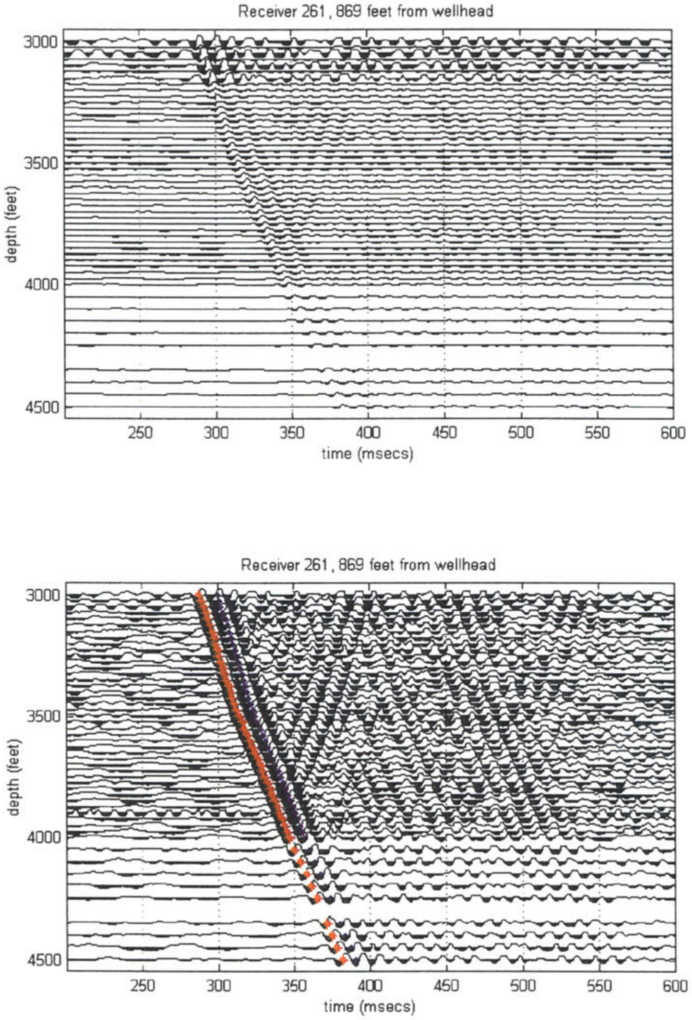

Figure 2-7: A common receiver gather before and after the receiver gain correction. The bottom plot also shows the picked first breaks (picked at the first zero crossing) as stars and the modeled first breaks as dots.

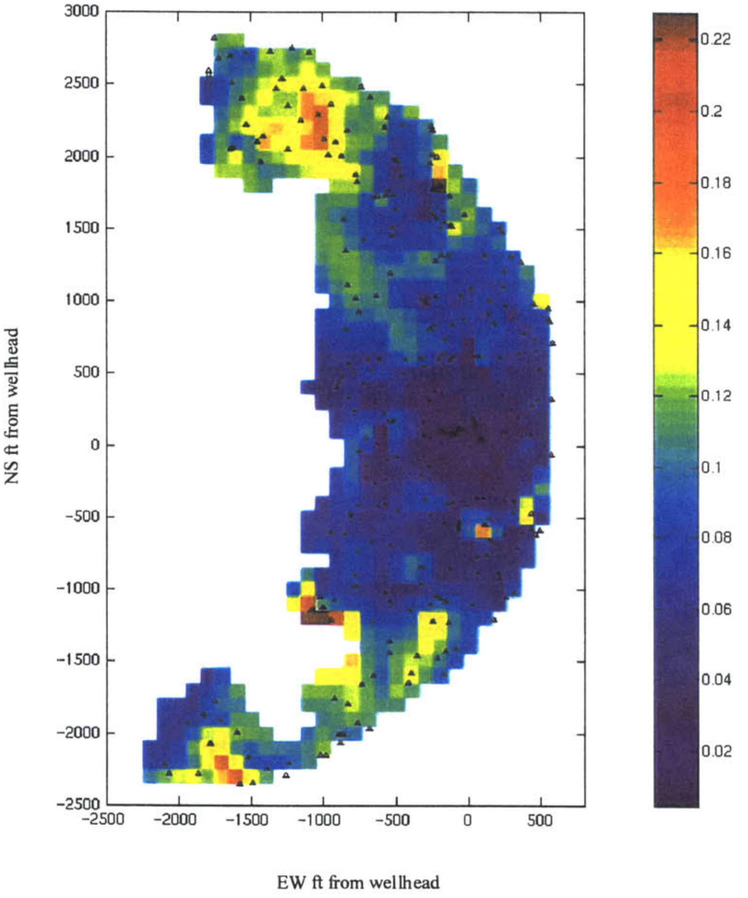

Figure 2-8: Semblance quality (a measure of signal to noise) of the data as a function of surface receiver position. Electric generators near the wellhead are the main source of noise,. The noise has relatively low frequency: below 35 Hz.

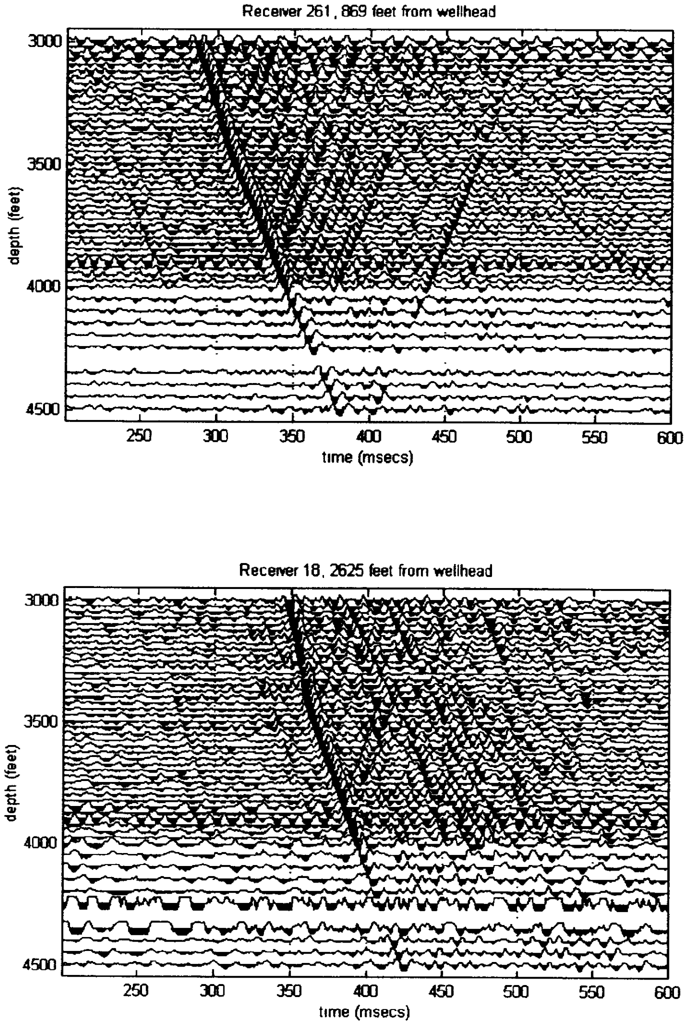

Figure 2-9: Common receiver gathers after deconvolution of gathers in Figure 2-5. This data will lead to much sharper images than the gathers in Figure 2-5, as ringing of strong reflectors won't mask weaker reflectors.

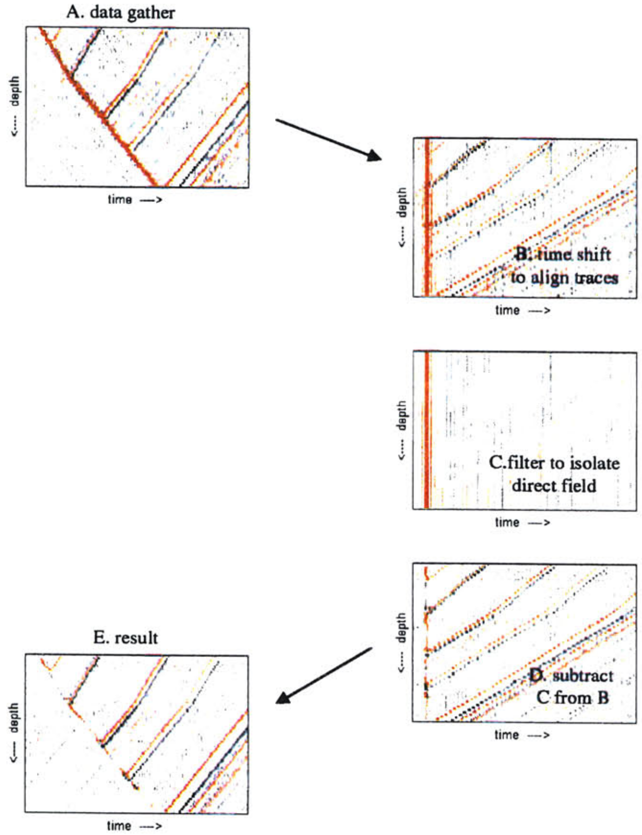

Figure 2-10: Steps in median filter separation of direct and reflected wavefields.

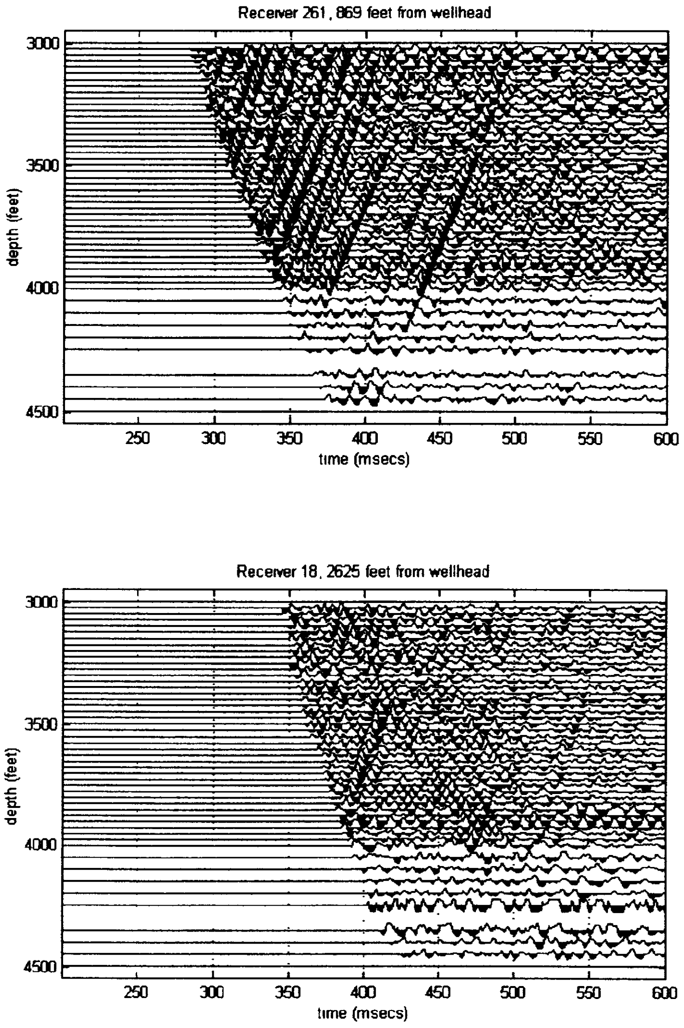

Figure 2-11: Result of median filtering to remove the direct wavefield. A top mute is applied to make the reflected energy more visible.

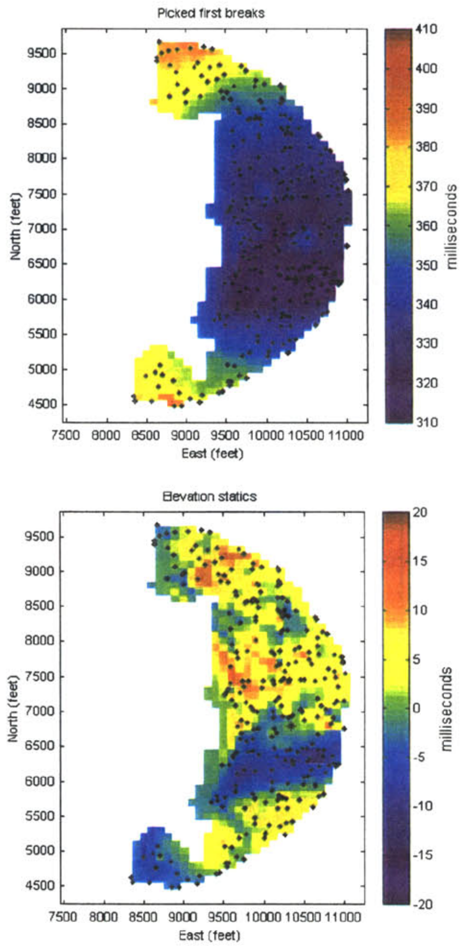

Figure 2-12: The top plot shows the first break times picked from a single shot gather. The bottom plot shows the elevation statics, calculated assuming vertical ray paths and a velocity of 2700 ft/s.

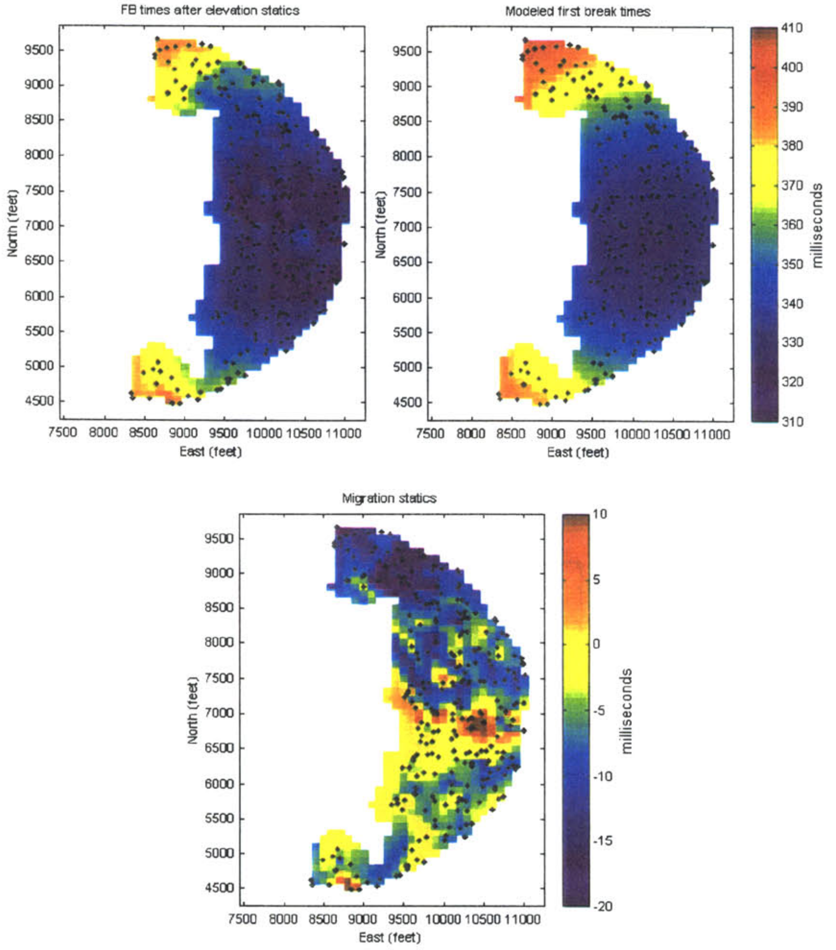

Figure 2-13: The difference between FB picks with elevation statics and the modeled first breaks are the migration statics. These are averaged over all shots and applied on a receiver consistent basis to minimize error due to inaccuracies in the velocity model.

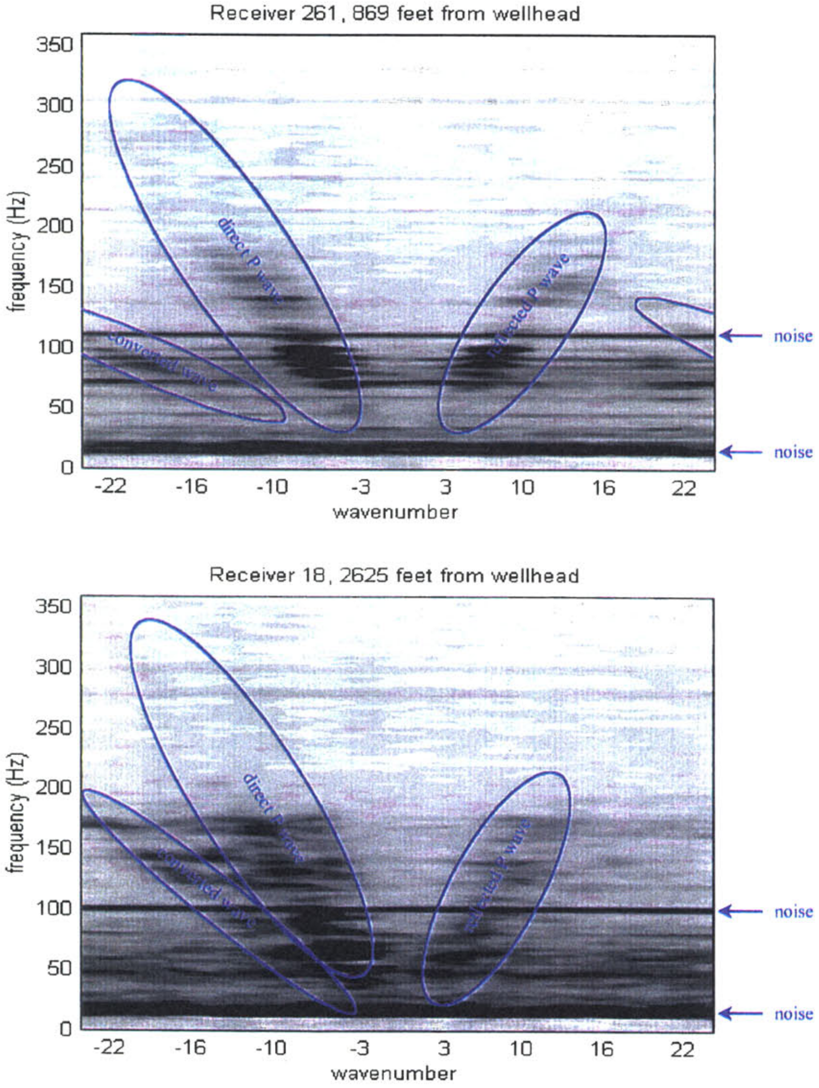

Figure 2-14: F-K transform of the gather in Figure 2-5. Only the portion of the data with regularly spaced shot locations (above 4000 feet) are used. The direct P wave has two lobes, especially in the receiver 18 gather, because of the change in velocity of the direct arrival at about 3500 feet depth.

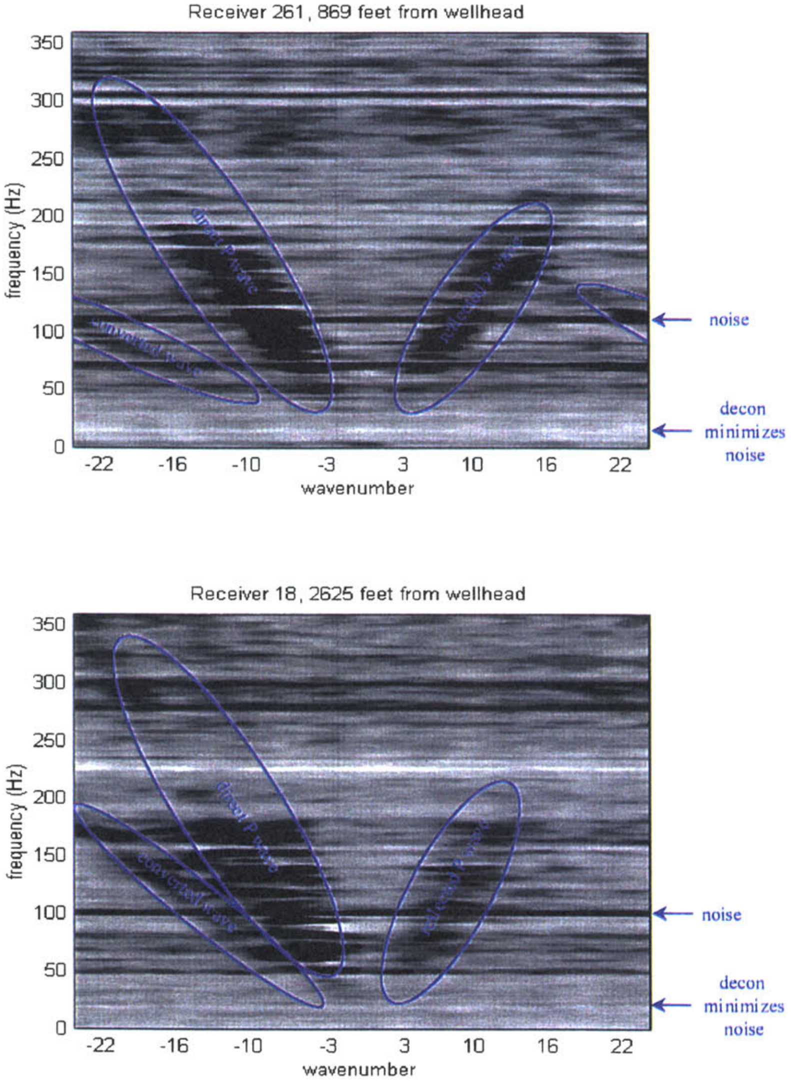

Figure 2-15: F-K transform of gathers after deconvolution. Below 40 Hertz, where there is not much coherent signal, the noise has been almost entirely removed.

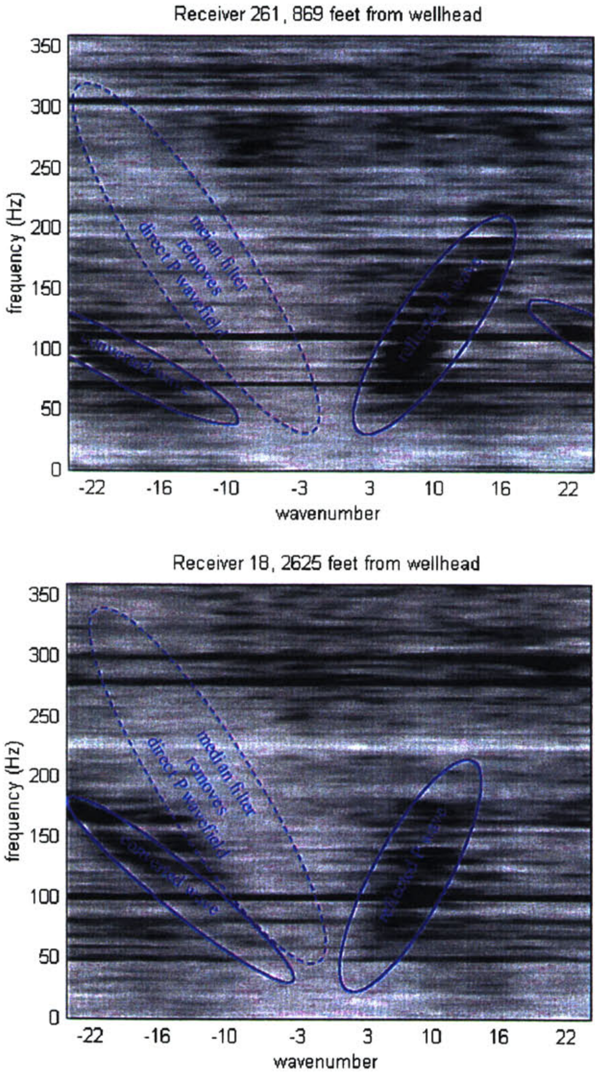

Figure 2-16: F-K transform of gathers after aplying the median filter to suppress the downgoing waves, without the top mute applied. The converted wave arrivals are still present.

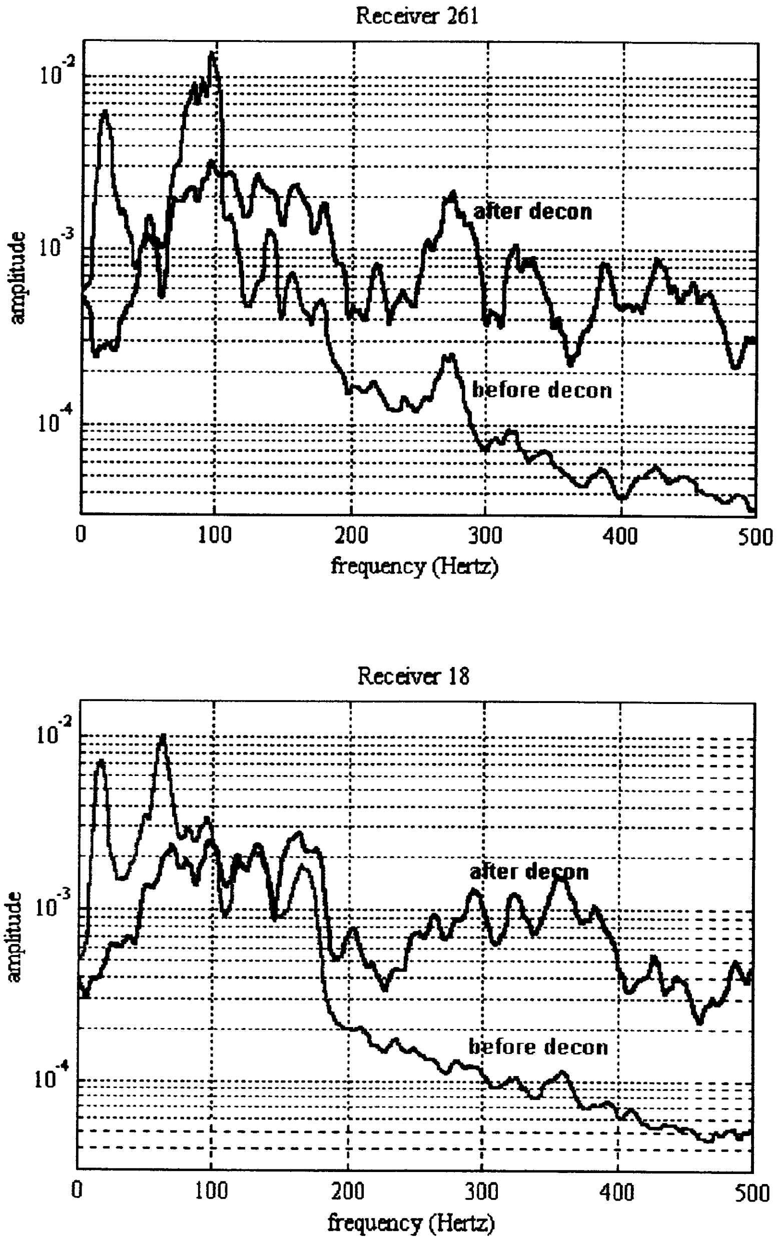

Figure 2-17: The normalized spectra of the gathers, before and after deconvolution.

Chapter 3

The Migration method

3.1 Introduction

3.1.1 Overview

To date, most published VSP imaging case studies have used migration techniques which were originally developed for data collected with surface seismic arrays, such as methods based on Stolt (1978) or Gazdag (1978). Few methods have been tailored specifically to the needs of borehole seismic data. This chapter introduces such a method.

Section 3.1 discusses VSP imaging techniques in the literature. Some of the assumptions made in the initial derivations of these migration methods do not apply to borehole seismic data. Section 3.2 is devoted to illustrating the shortcomings of conventional methods when applied to borehole seismic data, and identifying the assumptions which do not apply.

In Section 3.3, a new imaging process which addresses the issues identified in Section 3.2 is introduced in four steps. First, Section 3.3.1 shows how a *vector image* of the earth is formed. Second, Section 3.3.2 describes the derivation of *vector im-*

age isochrons, which define the shape of reflection events in the vector image space. Section 3.3.3 defines the vector image isochron (VII) transformation, which sums the vector image along the isochrons. Finally, Section 3.3.4 finishes the process by summing the transformed image over reflector orientations to form a scalar image.

The assumptions behind vector image isochrons are different for surface arrays than for borehole arrays, so the explicit derivations are presented in separate sections. Section 3.4 handles surface arrays, Section 3.5 borehole (VSP and RVSP) arrays.

Section 3.6 shows single reflector synthetic examples of transformed images for both types of array, as well as an example of the effect of multiple shot depths in RVSP studies.

Section 3.7 presents another example: synthetic data from a 3D model designed to be a simplified version of the Michigan test site. Images are produced with 3 different receiver arrays, two with the surface coverage of the intended 1998 RVSP study, (one regularly and one randomly distributed) and one array with the crescent shape of the 1998 RVSP receiver spread. This example provides a more realistic test of the VII imaging method, and suggests what can expected from the Michigan field data.

A small section at the end of the chapter, Section 3.8, derives an expression which is needed for the 3D vector image isochron derivations.

3.1.2 VSP migration methods in the literature

Until the 1980s, VSP datasets were generally either single level or single offset, with relatively small regions of illumination and low stacking fold. This limitation in hardware made VSP data poorly amenable to extensive imaging. Early imaging schemes by Dillon and Thomson (1984), Hardage (1985), and Wiggins et al. (1986) applied a VSP-CDP binning step to map time to depth. However, such binning techniques involve assumptions which apply only to reflectors close to the wellbore, causing increasing errors if one attempts more extensive imaging, especially in the presence of dip. Accurate VSP-CDP binning would be computationally demanding enough to approach the expense of prestack migration.

It has only been in the past 10 to 15 years that VSP datasets have had high enough fold to merit the type of migration schemes which are regularly applied to surface seismic data. These techniques have generally fallen into two classes: finite difference and Kirchhoff summaton.

Finite difference schemes have been fairly rare. A few examples are Lines et al. (1984) and Chang and McMechan (1986), both of which use finite difference reverse time migration techniques with the excitation time imaging condition.

Hokstad et al. (1998) found that wave-equation based migration schemes are more efficient on reverse VSP geometry, allowing for complicated model geometry and 3 component data, forming images from both P and S wave arrivals. To accommodate this, Hokstad et al. (1998), develops a reciprocity relation to transform the marine walkaway VSP data to RVSP. The resulting 2D images are similar in resolution to the surface seismics in the same region, but show better signal to noise.

Ray based Kirchhoff migration methods have the most common in the literature. Keho and Beydoun (1989) use paraxial Kirchhoff ray tracing to make 2D images of single source offset VSPs at the same test site in Michigan where the field data presented later in this thesis were collected. Dillon (1988) applied the Kirchhoff integral with Claerbout (1971)'s imaging condition, determining the image extent and resolution from the receiver array dimensions and source location.

Sun and McMechan (1988) used a combined inversion and migration technique to solve for earth parameters. Beydoun and Mendes (1987) used ray-born modeling in an iterative technique which both imaged the subsurface and inverted for seismic parameters.

Only a few applications of VSP imaging in 3D have appeared in the literature.

Chen and McMechan (1992) applied the reverse time method of Chang and McMechan (1986) to 3D RVSP synthetic data to test the feasibility of salt dome imaging, with promising results.

A 3D walkaway VSP is presented in van der Pal et al. (1996). They found the data processing to be cumbersome, taking 11 months. A large part of the processing time was spent developing software to cope with "complications caused by the structural configuration." They used the weighted Generalized Radon Transform method of Miller et al. (1987), the same basic method used in this thesis, but they needed "to choose a narrow dip aperture (1-2°) to generate a crisp image." The final image "demonstrates an improved resolution when compared to conventionally acquired (surface) 3D seismic."

Despite such promising results, images created from 3D borehole seismic data are still uncommon. The past year has seen advances in field hardware, such as downhole sources and receiver strings, which will hopefully lead to a flood of quality borehole seismic data. This would in turn push data processors to develop better and faster imaging techniques.

3.2 The conventional migration method

This section illustrates the shortcomings of a conventional migration method when applied to borehole seismic data. The conventional method is applied in 2D to synthetic data measured with a surface array in Section 3.2.1, and borehole seismic (RVSP) array in Section 3.2.2.

These examples show that the assumptions made in surface seismic data migration are not generally true of borehole seismic surveys. The difference is due to the illumination of the arrays, as discussed in Section 3.2.3.

3.2.1 GRT migration with a surface seismic array

Figure 3-1 shows a simple 2D earth model. The interfaces are density contrasts; the velocity is constant. This avoids any ray bending, making traveltime calculations trivial. There are three flat reflectors interspersed with two dipping reflectors; the shallowest dipping reflector has a dip of 5^o to the negative x direction, which is taken to be the negative dip direction. The deeper dipping reflector has a maximum dip of 15^o.

Figure 3-2 shows the geometry of a 2D surface seismic survey. The array of sources extends beyond the figure to the left and right, while the receiver array rolls along so that it is always centered on the shot location; the receiver array is shown at its location for the shot at distance $x = 0$ feet.

Figure 3-3 shows a common shot gather of the surface seismic data. A Ricker wavelet was used, with amplitudes based on ray path distance and transmission and reflection amplitudes. The triplication due to the bottom of the stepping reflector is included, but no special attention has been paid to the exact phase and amplitude behavior of the wavefield near caustics. This data is intended purely for illustration, not as a rigorous test of the method. No deconvolution or any other processing was done, so the wavelet shape will be apparent in the images.

The unlimited aperture image for the surface seismic synthetic data is shown in Figure 3-4. The aperture limit is a limit on the dip of the imaged plane. The reflectors are imaged evenly, although the triplication has lead to an artifact at the bottom of the stepping reflector.

A limited aperture image, with the aperture of $\pm 15^o$, is shown in Figure 3-5. The aperture limitation reduces the triplication artifact, but also causes the most steeply dipping reflector to fade significantly. Note that there is some loss of resolution, as the reflectors are slightly broader and the top of the stepping reflector is slightly less well defined than in Figure 3-4.

3.2.2 GRT migration with a borehole seismic array

Figure 3-6 shows a borehole seismic array. In keeping with the final goal of this thesis, the sources are located in the well and the receivers on the surface, although for this simple synthetic example the source and receiver positions are interchangeable.

Figure 3-7 contains a single shot gather of the synthetic data made with the RVSP array. As with the surface seismic, the triplication is visible in the stepping reflector.

Figure 3-8 shows the result of wide aperture (45^o) Kirchhoff migration of the synthetic RVSP data. Note that there are artifacts in even the flat reflectors. In addition, uneven illumination leads to variable amplitudes along the reflectors.

Figure 3-9 shows a limited aperture image made with the RVSP data, with the maximum aperture of 15^o. The aperture limitation reduces the artifacts and slightly evens the reflector brightnesses, but also causes a loss of amplitude along the most steeply dipping reflector.

Comparison of Figures 3-4 and 3-5 with Figures 3-8 and 3-9 suggests that there are issues related to borehole seismic arrays which are not addressed by conventional migration techniques.

3.2.3 The Differing assumptions

The artifacts in Figure 3-8 are caused by the geometry of the borehole seismic array. As will be shown in the next few sections, surface seismic data migration assumes that the ray coverage of each subsurface point is symmetric: for each ray that images a plane dipping to the left, another ray will image a plane dipping the same angle to the right. With borehole seismics this is not the case.

To allow a comparison, the result of imaging with the new migration technique is shown in Figure 3-10. Compared to Figure 3-8, migration smiles have been almost completely eliminated. Compared to Figure 3-9, the most steeply dipping reflector hasn't been lost. The variance in amplitudes due to the inherent fold of the borehole array are less severe than both of the conventional borehole seismic migration images.

After the terminology of the new method is defined in the next section, this example will be returned to, and the cause of the artifacts more explicitely shown (Section 3.6.3.)

3.3 The Vector Image Isochron (VII) imaging method

Section 3.2 showed a example in which the geometry of a borehole seismic array caused image artifacts. A new migration scheme is needed which can identify and minimize such artifacts without significant loss to the correctly located reflectors in the image. This section presents such a method.

The new method is described in four parts. Section 3.3.1 uses conventional summation migration to form an image of the earth which depends not only on subsurface location but also on the orientation of the imaged plane. This image will be referred to as a *vector image.*

Section 3.3.2 shows how *vector image isochrons*, which define the shape of reflection events in the vector image space, are derived. Explicit derivations depend on the array geometry, and are left to Sections 3.4 and Section 3.5.

The vector image is transformed in Section 3.3.3 by summing it along the isochrons, focusing reflected energy to the depth and plane from which it reflected. The transformed image therefore depends on subsurface location and *reflector* orientation, rather than *imaged plane* orientation. This process is referred to as vector image isochron (VII) transformation.

Finally, Section 3.3.4 collapses the transformed vector image to a scalar image by summing over reflector orientations.

3.3.1 The vector image migration integral

Let $\mathbf{x}$ be a point in the image grid, and let a plane P passing through $\mathbf{x}$ be described by its upward pointing normal $\mathbf{p}$. Seismic energy is incident on P at $\mathbf{x}$, and reflects according to Snell's law. The incident and reflected rays are described by unit vectors $\mathbf{s}$ and $\mathbf{r}$, respectively, which both point upward, away from the image point $\mathbf{x}$.

Two sets of angles will be used to describe $\mathbf{s}$ and $\mathbf{r}$. First, a vector angle $\phi = [\phi_a, \phi_d]$

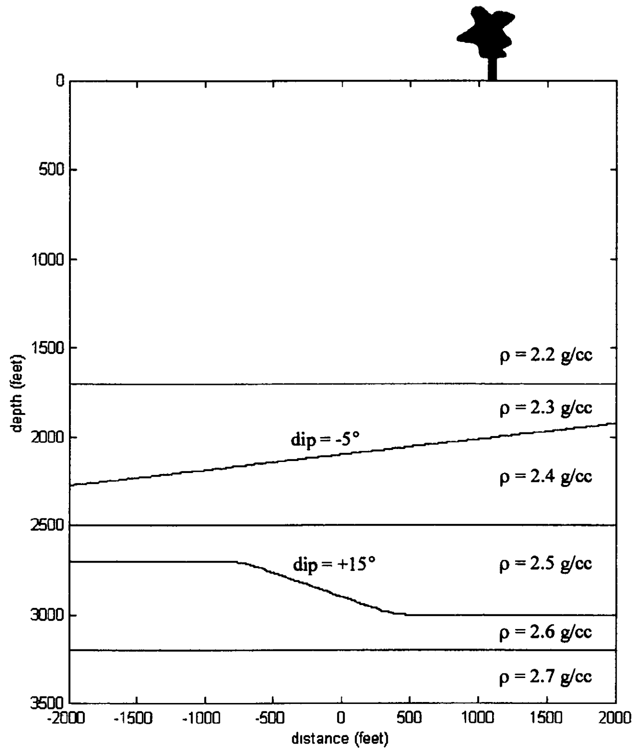

Figure 3-1: Simple constant velocity earth model used to illustrate the method.

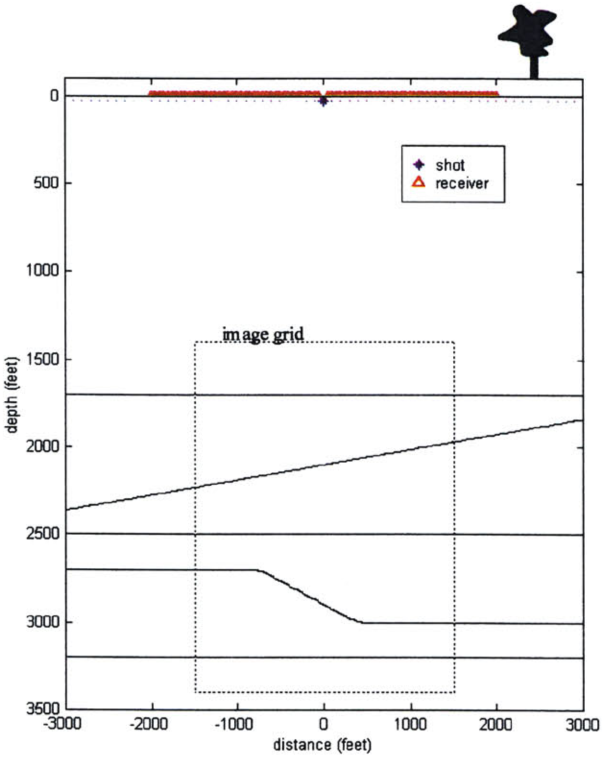

Figure 3-2: Geometry of a synthetic 2D field survey. The source positions, marked as blue stars, extend off the figure to the left and right. The receiver spread rolls along with the shots, so it is always centered on the shot locations. It is shown in position for the shot at distance 0.

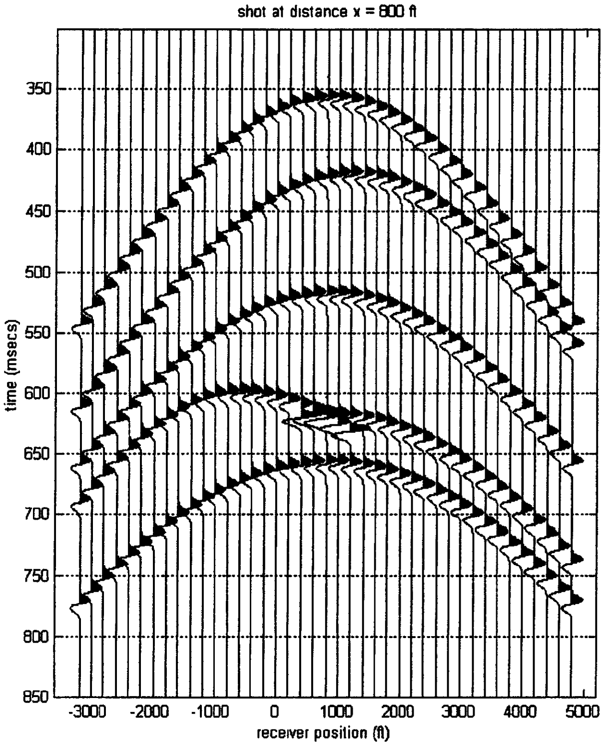

Figure 3-3: Synthetic surface seismic data: a single shot gather for the shot at x = 800 feet. The fourth reflector has a triplication where it flattens out.

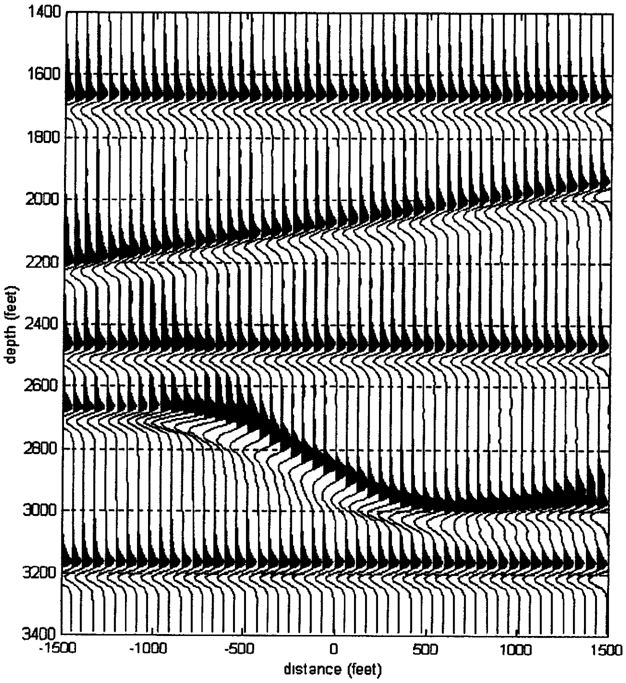

Figure 3-4: Wide aperture migration result with the surface seismic array. Note the artifact due to the triplication in the fourth reflector.

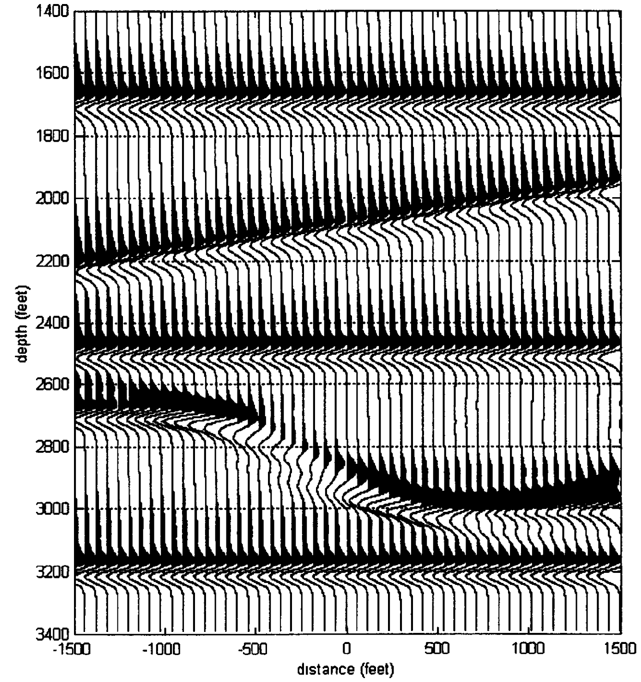

Figure 3-5: Surface seismic imaging result with an aperture limit of ±15°. The triplication artifact is reduced, but the steeply dipping reflector is worse.

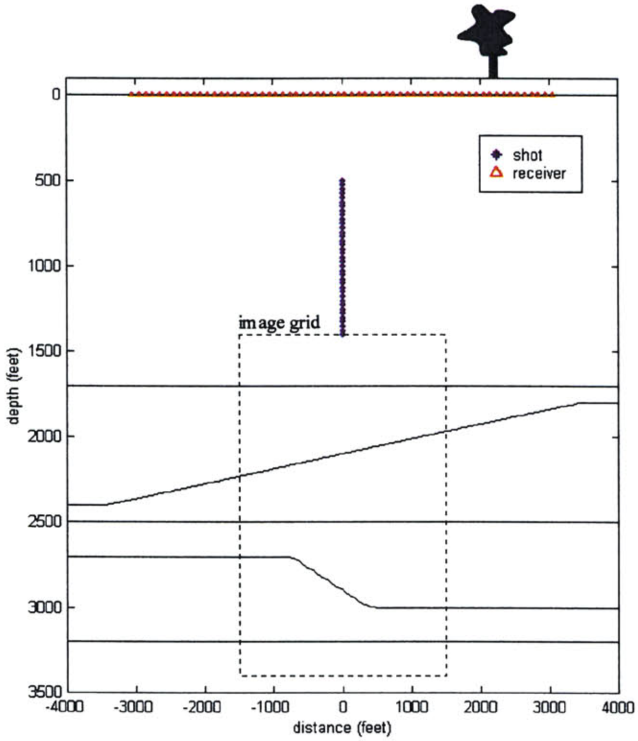

Figure 3-6: Geometry of the synthetic RVSP study.

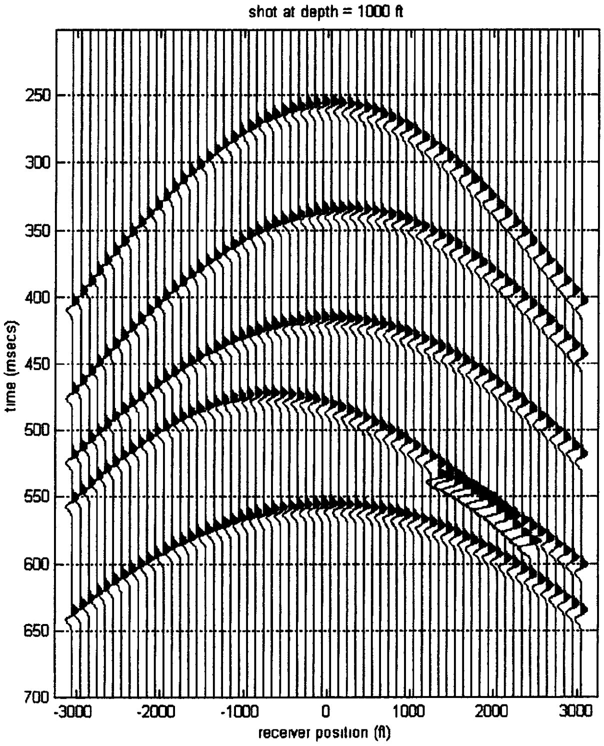

Figure 3-7: Example of synthetic RVSP data for the shot at 1050 ft depth.

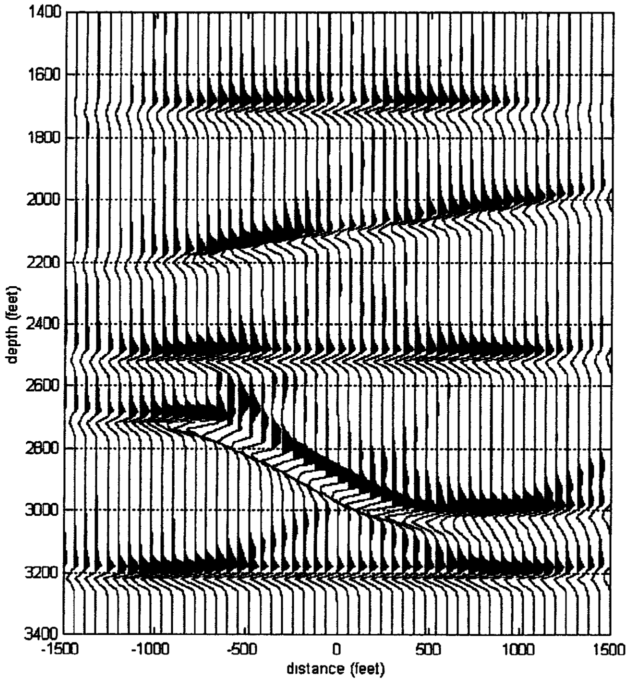

Figure 3-8: Wide aperture (45^o) RVSP imaging result. The triplication causes an artifact, but there are also artifacts in even the flat reflectors caused by the uneven coverage of the array. The vertical dashed line is referred to Figure 3-11.

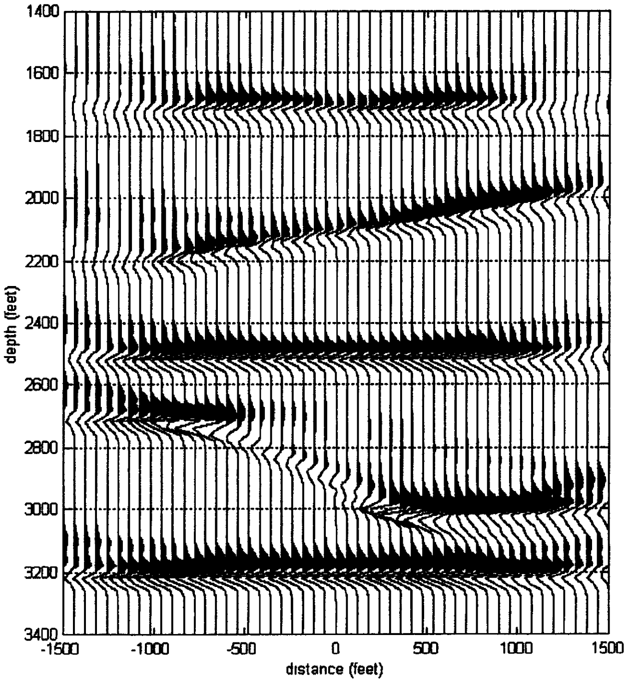

Figure 3-9: Limited aperture RVSP imaging result, with an aperture of 15°. The artifacts are reduced and amplitudes evened out somewhat, but at the cost of loss of brightness on the problematic fourth reflector.

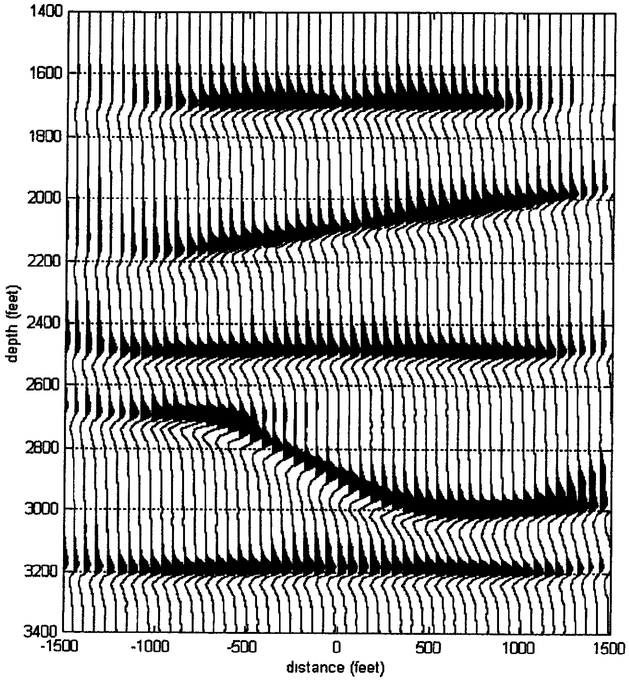

Figure 3-10: The image from the new imaging technique.

describes the imaged plane normal $\mathbf{p}$, as shown in Figure 3-11. ϕ_a is an azimuth of $\mathbf{p}$ measured relative to the +x axis and ϕ_d is the angle $\mathbf{p}$ makes with the z axis.

Second, the vector angle $\iota = [\iota_a, \iota_d]$ will describe the angle at which energy is reflected from the imaged plane, as shown in Figure 3-12. ι_a is the azimuth of $\mathbf{r}$ measured relative to the azimuth of $\mathbf{p}$, and ι_d is the angle $\mathbf{r}$ makes with $\mathbf{p}$. ι_a is in the range [0^o, 180^o), and ι_d is in (-90^o, 90^o).

Given some earth model, i.e. the migration velocity model, the source and receiver locations can be found by ray tracing in the directions defined by $\mathbf{s}$ and $\mathbf{r}$. For a plane $(\mathbf{x}, \phi)$, each value of ι describes a unique source receiver pair, and a unique traveltime.

$$\mathbf{x_s} \equiv \mathbf{x_s}(\mathbf{x}, \phi, \iota) \tag{3.1}$$

$$\mathbf{x_r} \equiv \mathbf{x_r}(\mathbf{x}, \phi, \iota) \tag{3.2}$$

$$t_{mig} \equiv t_{mig}(\mathbf{x}, \phi, \iota) \tag{3.3}$$

With this geometry, a migration process which forms a vector image $V(\mathbf{x}, \phi)$ can be expressed as a sum over the incidence angle ι. In an idealized experiment where the seismic displacement is known at every point along the source and receiver arrays, the summation can be written as an integral:

$$V(\mathbf{x}, \phi) = \int c_{mig} u(\mathbf{x_s}, \mathbf{x_r}, t_{mig}) d\iota \tag{3.4}$$

where $u(\mathbf{x_s}, \mathbf{x_r}, t_{mig})$ represents the displacement measured at the time t_{mig} with the source and receiver at the points $\mathbf{x_s}$ and $\mathbf{x_r}$. The weighting factor c_{mig} corrects for path length differences, wavefront spreading, and reflection amplitudes.

3.3.2 Isochrons in the vector image

The impulse response of the migration integral in Equation 3.4 is found by letting the seismic displacement measured by a receiver at $\mathbf{x_r}$ due to a source at $\mathbf{x_s}$ be a delta function. If A_{sr} and t_{sr} are the amplitude and traveltime along a specularly reflected ray, the measured displacement is:

$$u(\mathbf{x_s}, \mathbf{x_r}, t_{sr}) = A_{sr}\delta(t - t_{sr}) \tag{3.5}$$

The traveltime t_{sr} depends on the source and receiver positions and the earth model. If the reflector is approximated to be planar at the point where the ray refects, and defined by its position at a point $\mathbf{x_{ref}}$ and orientation angle $\theta = [\theta_a, \theta_d]$, then

$$t_{sr} \equiv t_{sr}(\mathbf{x_s}, \mathbf{x_r}, \mathbf{x_{ref}}, \theta) \tag{3.6}$$

Given the data in Equation 3.5, Equation 3.4 becomes:

$$V(\mathbf{x}, \phi) = \int c_{mig} A_{sr} \delta(t_{mig} - t_{sr}) d\iota \tag{3.7}$$

and is nonzero only when

$$t_{mig}(\mathbf{x}, \phi, \iota) = t_{sr}(\mathbf{x_s}, \mathbf{x_r}, \mathbf{x_{ref}}, \theta) \tag{3.8}$$

Since $\mathbf{x_s}$ and $\mathbf{x_r}$ can be described as in Equation 3.1, the equality 3.8 leads to a relation between $\mathbf{x}$, ϕ, and ι for a given reflector $\mathbf{x_{ref}}$, θ. This relation describes *vector image isochron* surfaces; these surfaces are parameterized as functions of the imaged plane orientation ϕ and incidence angle ι_d:

$$\mathbf{x_{iso}} \equiv \mathbf{x_{iso}}(\phi, \iota; \mathbf{x_{ref}}, \theta) \tag{3.9}$$

Since the isochrons depend on ray paths, they cannot be explicitely derived for a general earth model. They also rely on different assumptions for borehole seismic arrays than for surface seismic arrays. Sections 3.4 and 3.5 will derive vector image isochrons for surface seismic and borehole seismic arrays given two assumptions; (1) a constant velocity earth, and (2) linear or, in 3D, planar reflectors.

3.3.3 Transforming the vector image

The previous section showed how the migration process in Equation 3.4 puts reflected energy along curves called vector image isochrons, Equation 3.9.

The vector image $V(\mathbf{x}, \phi)$ can be transformed by summing along the isochrons. The transformed image $V'(\mathbf{x}, \theta)$ is:

$$\begin{aligned} V'(\mathbf{x}, \theta) &= \int V(x, \phi)\delta(x - \mathbf{x_{iso}}(\phi; \mathbf{x_{ref}}, \theta)d\phi \\ &= \int V(\mathbf{x_{iso}}(\phi; \mathbf{x_{ref}}, \theta), \phi))d\phi \end{aligned} \tag{3.10}$$

This transform will be referred to as the vector image isochron (VII) transform. The transformed image can be thought of as a function of reflector orientation, whereas the untransformed vector image was a function of the imaged plane. Examples in later sections will illustrate the difference.

3.3.4 Summation over planes

To form a final scalar image, the transformed vector image is summed along reflector orientations:

$$I(\mathbf{x}) = \int V'(\mathbf{x}, \theta) d\theta \tag{3.11}$$

3.4 Surface seismic array isochrons

3.4.1 The isochron principle

Images made with surface seismic data tend not to have the kind of artifacts which the vector image isochron (VII) transform is designed to minimize. However, it is useful to derive the vector image isochrons for surface seismic arrays, for completeness and to illustrate the process.

As described in Section 3.3.2, isochron curves are derived by equating two traveltimes, illustrated in Figure 3-13. First, the *migration traveltime* is the traveltime of rays which reflect off each plane in the image space. For surface seismics, there are several traveltimes for each imaged plane, as there are several scattering angles. At the point the image location $\mathbf{x}$ in Figure 3-13, the imaged plane orientation ϕ and a specified incidence angle ι define a source receiver pair and a migration traveltime. This is true of every $(\mathbf{x}, \phi)$ point in the image space, and is purely a mathematical construct. It doesn't necessarily correspond to a physical reflector.

The second traveltime in the equality is the *specular traveltime*, and involves assuming that a certain plane, such as the one described by an angle θ at the point $\mathbf{x}$ in Figure 3-13, is an actual reflector. Therefore, the data recorded by the source receiver pair will contain reflected energy at a traveltime which is dependent on the source and receiver positions and the reflector parameters $\mathbf{x_{ref}}$ and θ. If the traveltime along the migration raypath equals the time along the specular ray path for any source-receiver pair, $\mathbf{x_{ref}}$ and $\mathbf{x}$ will lie on an isochron in the vector image, and the migrated image at the point $\mathbf{x}$ will contain energy from the reflector at $\mathbf{x_{ref}}$.

The derivation of the isochrons starts by setting up the geometry of the reflected ray at the imaged plane, which defines the source and receiver location and migration traveltime. Then the specular traveltime for that source-receiver pair is calculated, and finally the two times are set equal.

Since the isochrons depend on ray paths, they cannot be derived in a general earth model. The derivation presented here makes two assumptions; (1) a constant velocity earth, and (2) linear or, in 3D, planar reflectors. In the remainder of Section 3.4, expressions for the vector image isochrons will be derived for surface seismic arrays, in 2D and 3D. Section 3.5 derives vector image isochrons for borehole seismic arrays in 2D and 3D.

3.4.2 The geometry at the reflector

To describe the normal to the imaged plane $\mathbf{p}$ and the ray normals $\mathbf{s}$ and $\mathbf{r}$ in terms of the angles ι and θ, start in coordinate system rotated so that the z' axis is in the direction of the $\mathbf{p}$. In the prime coordinate system, as shown in Figure 3-12,

$$\begin{aligned}
\mathbf{p}' &= [0,0,1] \\
\mathbf{s}' &= [-\cos\iota_a \sin\iota_d, \quad -\sin\iota_a \sin\iota_d, \quad \cos\iota_d] \qquad (3.12)\\
\mathbf{r}' &= [\cos\iota_a \sin\iota_d, \quad \sin\iota_a \sin\iota_d, \quad \cos\iota_d]
\end{aligned}$$

These normals are rotated according to the imaged plane orientation. First, around the y axis by the imaged plane dip angle ϕ_d, then around the z axis by the imaged plane azimuth angle ϕ_a:

$$R_{zy} = R_z R_y = \begin{bmatrix} \cos\phi_a & -\sin\phi_a & 0 \\ \sin\phi_a & \cos\phi_a & 0 \\ 0 & 0 & 1 \end{bmatrix} * \begin{bmatrix} \cos\phi_d & 0 & \sin\phi_d \\ 0 & 1 & 0 \\ -\sin\phi_d & 0 & \cos\phi_d \end{bmatrix} \tag{3.13}$$

The resulting normals are:

$$\mathbf{p} = \mathbf{Rp}' = [\cos\phi_\mathbf{a} \sin\phi_\mathbf{d}, \sin\phi_\mathbf{a} \sin\phi_\mathbf{d}, \cos\phi_\mathbf{d}] \tag{3.14}$$

$$\begin{aligned} \mathbf{s} &= R\mathbf{s}' \\ &= \begin{bmatrix} \cos\iota_d \cos\phi_a \sin\phi_d + \sin\iota_a \sin\iota_d \sin\phi_a - \cos\iota_a \sin\iota_d \cos\phi_a \cos\phi_d \\ \cos\iota_d \sin\phi_a \sin\phi_d - \sin\iota_a \sin\iota_d \cos\phi_a - \cos\iota_a \sin\iota_d \sin\phi_a \cos\phi_d \\ \cos\iota_a \sin\iota_d \sin\phi_d + \cos\iota_d \cos\phi_d \end{bmatrix} \end{aligned} \tag{3.15}$$

$$\begin{aligned} \mathbf{r} &= R\mathbf{r}' \\ &= \begin{bmatrix} \cos\iota_d \cos\phi_a \sin\phi_d - \sin\iota_a \sin\iota_d \sin\phi_a + \cos\iota_a \sin\iota_d \cos\phi_a \cos\phi_d \\ \cos\iota_d \sin\phi_a \sin\phi_d + \sin\iota_a \sin\iota_d \cos\phi_a + \cos\iota_a \sin\iota_d \sin\phi_a \cos\phi_d \\ -\cos\iota_a \sin\iota_d \sin\phi_d + \cos\iota_d \cos\phi_d \end{bmatrix} \end{aligned} \tag{3.16}$$

In a constant velocity earth, the raypaths are straight and the source and receiver locations can be calculated from the image point $\mathbf{x}$ and the ray normals $\mathbf{s}$ and $\mathbf{r}$:

$$\mathbf{x} = [x, y, z] \tag{3.17}$$

$$\mathbf{x_s} = \mathbf{x} + (z_s - z)\frac{\mathbf{s}}{s_3} \tag{3.18}$$

$$\mathbf{x_r} = \mathbf{x} + (z_r - z)\frac{\mathbf{r}}{r_3} \tag{3.19}$$

where s_3 and r_3 are the z components of $\mathbf{s}$ and $\mathbf{r}$. The z components of $\mathbf{s}$ and $\mathbf{r}$ give the angle of the ray from the vertical, which leads to the migration ray path length:

$$\begin{aligned} s_{mig} &= \frac{z}{s_3} + \frac{z}{r_3} \\ &= \frac{2z\cos\iota_d\cos\phi_d}{\cos{\iota_d}^2\cos{\phi_d}^2 - \cos{\iota_a}^2\sin{\iota_d}^2\sin{\phi_d}^2} \end{aligned} \tag{3.20}$$

The specular traveltime is found by adapting a 2D VSP formula from Wyatt and Wyatt (1981), which finds the traveltime for a reflected ray for a source on the surface and a receiver in a well, given a linearly dipping reflector in a constant velocity earth. This expression is easily adapted to RVSP by switching the source and receiver positions, and also can be used for surface seismics by letting the depth of the downhole station go to zero.

In the RVSP case, given a surface receiver at $(x_r, 0)$, a downhole source at (x_s, z_s), and a planar reflector described by its dip angle θ_d and its depth d at the source x location, the path length of the specularly reflected ray in a constant velocity earth is:

$$\begin{aligned} s_{sr}^2 = (x_s - x_r)^2 + z_s^2 + 4d(d - z_s)\cos{\theta_d}^2 \\ +4(x_s - x_r)(d - z_s)\sin\theta_d\cos\theta_d \end{aligned} \tag{3.21}$$

Section 3.8 uses a coordinate rotation to apply Equation 3.21 to the 3D case when θ is vector valued, the receiver is at $(x_r, y_r, 0)$, and the source is at $(x_s, y_s, 0)$:

$$\begin{aligned} s_{sr}^2 = ((x_r - x_s)\cos\theta_a + (y_r - y_s)\sin{\theta_a}^2 + z_s^2 + 4d^2\cos{\theta_d}^2 \\ +4(z_s - d)((x_r - x_s)\cos\theta_a + (y_r - y_s)\sin\theta_a)\sin\theta_d\cos\theta_d \end{aligned} \tag{3.22}$$

At this point, the derivation is continued in 2D. Examination of the results in 2D leads to a simplifaction which is used in the derivation of 3D surface seismic array isochrons.

3.4.3 Surface seismic isochrons in 2D

To reduce the problem to two dimensions, take $\theta_a = \phi_a = \iota_a = 0$. Equations 3.14, 3.15 and 3.16 become:

$$\mathbf{p} = [\sin\phi_d, 0, \cos\phi_d], \tag{3.23}$$

$$\mathbf{s} = [-\sin\iota_d\cos\phi_d + \cos\iota_d\sin\phi_d, 0, \sin\iota_d\sin\phi_d + \cos\iota_d\cos\phi_d] \tag{3.24}$$

$$\mathbf{r} = [\sin\iota_d\cos\phi_d + \cos\iota_d\sin\phi_d, 0, -\sin\iota_d\sin\phi_d + \cos\iota_d\cos\phi_d] \tag{3.25}$$

Equations 3.17, 3.18, and 3.19 with $z_s = z_r = 0$ becomes:

$$\mathbf{x} = [x, 0, z] \tag{3.26}$$

$$\mathbf{x_s} - \mathbf{x} = [-z\tan(\iota_d + \theta_d), 0, -z] \tag{3.27}$$

$$\mathbf{x_r} - \mathbf{x} = [-z\tan(\iota_d - \theta_d), 0, -z] \tag{3.28}$$

From Eq. 3.20, the migration ray path length with $\theta_a = 0$ is:

$$\begin{aligned} s_{mig} &= 2z\frac{\cos\iota_d\cos\theta_d}{\cos\iota_d^2-\sin\theta_d^2} \\ &= z\left(\frac{1}{(\cos\iota_d+\theta_d)}+\frac{1}{(\cos\iota_d-\theta_d)}\right) \end{aligned} \tag{3.29}$$

Since the velocity is constant, the ray path lengths can be equated instead of traveltimes. Using the specular ray path length Equation 3.21, with the depth of the reflector at the source d, expressed in terms of the reflector depth at the image point z_{ref}, so $d = z_{ref} + (x_s - x)\tan\theta_d$:

$$\begin{aligned} s_{sr}^2 = (x_s - x_r)^2 + 4(z_{ref} + (x_s - x)\tan\theta_d)^2\cos\theta_d^2 \\ +4(x_s - x_r)(z_{ref} + (x_s - x)\tan\theta_d)\sin\theta_d\cos\theta_d \end{aligned} \tag{3.30}$$

The source and receiver locations given in Equation 3.27 and 3.28 are plugged into 3.30, giving an expression for the ray path distance squared as a function of z, ϕ_d, ι_d, z_{ref}, and θ_d. Since the source and receiver arrays are assumed to extend over entire surface, the x position of the image point is taken to be the origin with no loss of generality.

The square root of Equation 3.30 is equated to the migration raypath 3.29

$$s_{sr}(z, \phi_d, \iota_d, z_{ref}, \theta_d) = s_{mig}(z, \phi_d, \iota_d) \tag{3.31}$$

leading to a quadratic equation for z with the following solution:

$$\frac{z}{z_{ref}} = \frac{\cos\theta_d(\sin\theta_d\sin\phi_d\cos\phi_d \pm \cos\iota_d\sqrt{\cos\phi_d^2 - \cos\theta_d^2\sin\iota_d^2}}{\cos\theta_d^2\cos\iota_d^2 + \sin\theta_d^2\cos\phi_d^2} \tag{3.32}$$

The roots of Equation 3.32 are complex when $\sin\phi_d^2 > \cos\iota_d^2$. This corresponds to the case when at least one of the reflected or incident rays is downgoing, and so can't reach the surface.

In the special case of a flat reflector, $\theta_d = 0$, and Equation 3.32 describes ellipses in $[z, \sin\phi_d]$ space for each value of ι_d:

$$\left(\frac{z}{z_{ref}}\right)^2 + \left(\frac{\sin\phi_d}{\cos\iota_d}\right)^2 = 1 \tag{3.33}$$

as plotted in Figure 3-14. All the ellipses pass through the point where $z/z_{ref} = 1$, and $\sin\phi_d = 0$, and grow narrower in the $\sin\phi_d$ dimension as ι_d increases.

To better comprehend Figure 3-14, recall that the migration raypath scattering angles ι_d are those for which the integrand in Equation 3.7 is nonzero, and the location of the contours shows the part of the image which receives some energy contribution from the dataset Equation 3.5. The more closely the contours are spaced, the more energy that part of the image will be likely to have. The point where $z = z_{ref}$ and $sin\theta_d = 0$, corresponds to the location of the actual reflector. All contours overlap at this point, meaning that this point should have the most energy in the image.

For comparison, consider any other point on any isochron. At these points there are no reflectors in the earth, but there will be energy in the image because, for that depth and imaged plane dip, there is a source receiver pair for which the migration traveltime equals the specular raypath traveltime.

Theoretically, all points within the ellipse are imaged, and with infinite surface arrays on a flat earth would contain some energy. Realistically, seismic surveys are not designed to sample large incidence angles. Reflection amplitudes become critical, usually at about 30^o. Also, large scattering angles tend to involve long ray paths, becoming increasingly difficult to measure. For this reason, as well as due to the spacing of the ι_d contours, most energy in the image is expected to lie near the $\iota_d = 0$ ellipse.

Figure 3-15 contains an image made from synthetic data with a single horizontal reflector, with ι_d contours. The horizontal axis is ϕ_d in degrees instead of the less intuitive $\sin\phi_d$. The energy lies mostly along the $\iota_d = 0$ contour as expected, and is brightest at the point corresponding to the actual reflector depth and orientation.

In the case of a dipping reflector, the contours of ι_d are no longer ellipses. The more steeply the reflector dips, the further the contours are from ellipses, in more than just shape. For example, Figure 3-16 has ι_d contours from Equation 3.32 plotted over a vector image of a single reflector dipping at 20^o. The peak energy is at the point with $z/z_{ref} = 1$, $\phi_d = 20^o$, but the curve is slightly asymmetric in intensity as well as shape. The left branch of the curve, with negative ϕ_d, is slightly brighter and broader than the right branch.

3.4.4 Surface seismic isochrons in 3D

The example in 2D showed that the energy of reflected events in the surface seismic vector image lies predominantly along the $\iota_d = 0$ contour. It is possible to make contours in 3D for any value of ι_d, but it isn't necessary, and much troublesome algebra can be avoided by setting $\iota_d = 0$ initially. Therefore, $\mathbf{s}$ and $\mathbf{r}$ are equal to $\mathbf{p}$ and the source and receiver have the same location $\mathbf{x_s}$.

In 3D, the reflector is described by its depth z_{ref} at the image point and the orientation of its normal, a two valued angle $\theta = [\theta_a, \theta_d]$. The imaged plane is similarly described by a two valued angle $\phi = [\phi_a, \phi_d]$.

Equation 3.22 gives the ray path length between a surface source and a surface receiver given a planar reflector. If $x_s = x_r$ and $y_s = y_r$:

$$s_{sr} = 2d\cos\theta_d \tag{3.34}$$

where d is the depth of the reflector at the source location:

$$d = z_{ref} - x_s \cos\theta_a \tan\theta_d - y_s \sin\theta_a \tan\theta_d \tag{3.35}$$

Equations 3.34 and 3.35 give a specular ray path length of:

$$s_{sr} = 2z_{ref}\cos\theta_d - 2\sin\theta_d(x_s\cos\theta_a + y_s\sin\theta_a) \tag{3.36}$$

This distance is evaluated at the source and receiver locations defined by the imaged plane:

$$\begin{aligned} x_s &= -z\cos\phi_a\tan\phi_d \\ y_s &= -z\sin\phi_a\tan\phi_d \end{aligned} \tag{3.37}$$

and set equal to the migration ray path length Equation 3.20 with $\iota_d = 0$:

$$s_{mig} = \frac{2z}{\cos\phi_d} \tag{3.38}$$

with the result:

$$\frac{z}{z_{ref}} = \frac{-\cos\theta_d\cos\phi_d}{1 + \sin\phi_d\sin\theta_d(\cos\phi_a\cos\theta_a + \sin\phi_a\sin\theta_a)} \tag{3.39}$$

In the 2D case where $\theta_a = \phi_a = 0$,

$$\frac{z}{z_{ref}} = \frac{-\cos\theta_d\cos\phi_d}{1 + \sin\theta_d\sin\phi_d} \tag{3.40}$$

which, with some trig manipulation, is the same as the 2D result Equation 3.32 with $\iota_d = 0$.

3.5 Downhole seismic array isochrons

A different approach is needed to map isochrons in borehole seismic vector images, since the source array has a fixed (x, y) location, but varies in depth.

The approach taken here is to fix the source depth and to calculate the isochrons one shot depth at a time. (The consequences of this assumption will be discussed in Section 3.6.4.) Since the isochrons are mapped one shot depth at a time, there is only one raypath which illuminates each image point and plane. The incidence angle ι will not be an independent variable as it was in the case of surface seismic arrays.

Another difference between surface array and borehole array isochrons, caused by the fixed (x, y) location of the source, is that the shape of the isochrons will be different at different image (x, y) locations. Therefore, the origin is taken to be the shot location instead of the image location. The depth of the model reflector will still be measured at the origin, but now this will be at the source, and not at the image point.

3.5.1 Downhole seismic array isochrons in 2D

Figure 3-17 shows the geometry of the raypaths. As mentioned above, this is different from the surface seismic case because the incident angle is determined by the imaged point and plane and the source location. Equations 3.14 through 3.20 from the surface seismic derivation still hold, but each imaged plane will have only one specular ray, and one corresponding value of ι.

The borehole seismic isochrons are found numerically by equating specular and migration ray path lengths according to Equation 3.21 in 2D and Equation 3.22 in 3D.

In 2D, an image point at $(x,\ z,\ \phi_d)$ and a reflector with dip angle θ_d and depth

z_{ref} at the origin has migration and specular ray path lengths from Equation 3.21:

$$\begin{aligned} s_{mig}^2 = (x_s - x_r)^2 + z_s^2 + 4d(d - z_s)\cos{\phi_d}^2 \\ +4(x_s - x_r)(d - z_s)\sin\phi_d \cos\phi_d \end{aligned} \tag{3.41}$$

$$\begin{aligned} s_{sr}^2 = (x_s - x_r)^2 + z_s^2 + 4z_{ref}(z_{ref} - z_s)\cos{\theta_d}^2 \\ +4(x_s - x_r)(z_{ref} - z_s)\sin\theta_d \cos\theta_d \end{aligned} \tag{3.42}$$

where d is the depth of the imaged plane at the source x location:

$$d = z + (x - x_s)\tan\phi_d \tag{3.43}$$

The source location (x_s, z_s) is fixed, and the receiver location x_r is found by solving for the incidence angle ι_d. Eq. 3.27 can be rearranged:

$$\iota_d = \arctan\left(\frac{x_s - x}{z_s - z}\right) - \phi_d \tag{3.44}$$

leading to the receiver location.

$$x_r = x + z\frac{x - (z_s - z)\tan 2\phi_d}{z_s - z + x\tan 2\phi_d} \tag{3.45}$$

Setting the traveltimes in Eq. 3.41 and 3.42 equal:

$$\begin{aligned} 4d(d - z_s)\cos{\phi_d}^2 + 4(x_s - x_r)(d - z_s)\sin\phi_d\cos\phi_d \\ = 4z_{ref}(z_{ref} - z_s)\cos{\theta_d}^2 + 4(x_s - x_r)(z_{ref} - z_s)\sin\theta_d\cos\theta_d \end{aligned} \tag{3.46}$$

which, using Equations 3.43 and 3.45, is solved numerically for z.

The roots of Equation 3.46 are isochrons in the 2D borehole seismic vector image space. Figure 3-18 shows a 2D borehole seismic image and its isochron according to Equation 3.46. The asymmetry of the image is caused by the array: the cube in the upper left shows the dipping reflector, the shot location, and the line of surface receivers. The image is over the range of depths shown as a vertical line. Some planes dip away from the source enough that reflected rays never reach the receiver array. These are the negative dips and large positive dips, where the image is blank.

3.5.2 Downhole seismic array isochrons in 3D

In 3D, the same process is followed, with slightly more complicated expressions. The image point (x, y, z, ϕ_a, ϕ_d) and reflector with orientation $\theta = (\theta_a, \theta_d)$ and depth z_{ref} at the origin has ray path lengths:

$$\begin{aligned} s_{mig}^2 &= (x_r \cos\phi_a + y_r \sin\phi_a)^2 + z_s^2 - 4d(z_s - d)\cos{\phi_d}^2 \\ &+4(x_r \cos\phi_a + y_r \sin\phi_a)(z_s - d)\sin\phi_d \cos\phi_d \end{aligned} \tag{3.47}$$

$$\begin{aligned} s_{sr}^2 &= (x_r \cos\theta_a + y_r \sin\theta_a)^2 + z_s^2 - 4z_{ref}(z_s - z_{ref})\cos{\theta_d}^2 \\ &+4(x_r \cos\theta_a + y_r \sin\theta_a)(z_s - z_{ref})\sin\theta_d \cos\theta_d \end{aligned} \tag{3.48}$$

where d is the imaged plane depth at the source x location:

$$z_{ref} = z + (x - x_s)\cos\phi_a \tan\phi_d + (y - y_s)\sin\phi_a \tan\phi_d \tag{3.49}$$

The incidence angle is found by defining A_s and B_s from Equation 3.15:

$$A_s = \frac{x_s - x}{z_s - z} = \frac{s_1}{s_3} \tag{3.50}$$

$$B_s = \frac{y_s - y}{z_s - z} = \frac{s_2}{s_3} \tag{3.51}$$

and solving for $\tan \iota_d$:

$$\begin{aligned} \tan \iota_d &= \frac{\cos \phi_a \sin \phi_d - A_s \cos \phi_d}{A_s \cos \iota_a \sin \phi_d + \cos \iota_a \cos \phi_a \cos \phi_d - \sin \iota_a \sin \phi_a} \\ \tan \iota_d &= \frac{\sin \phi_a \sin \phi_d - B_s \cos \phi_d}{B_s \cos \iota_a \sin \phi_d + \cos \iota_a \sin \phi_a \cos \phi_d + \sin \iota_a \cos \phi_a} \end{aligned} \tag{3.52}$$

These are set equal to each other to solve for ι_a:

$$\begin{aligned} &\cos \iota_a (B_s \cos \phi_a - A_s \sin \phi_a) \\ &= \sin \iota_a (B_s \sin \phi_a \cos \phi_d + A_s \cos \phi_a \cos \phi_d - \sin \phi_d) \end{aligned} \tag{3.53}$$

The receiver position according to Equation 3.19, with the receiver depth set to 0, is

$$\begin{aligned} x_r - x &= -z \frac{r_1}{r_3} \\ y_r - y &= -z \frac{r_2}{r_3} \end{aligned} \tag{3.54}$$

Equations 3.52 and 3.53 are used to eliminate ι_a and ι_d from r_1, r_2, and r_3 in Equation 3.54. The results are expressions for x_r and y_r in terms of x, y, x_s, y_s, ϕ_a, and ϕ_d.

Equating the migration ray path length Equation 3.47 and the specular ray path length Equation 3.48 leads to an expression for the borehole seismic vector image isochrons. The solution, found numerically, describes a surface in depth z in terms of variables ϕ_a, and ϕ_d, with x, y, x_s, y_s, z_s, z_{ref}, θ_a and θ_d fixed.

Figure 3-19 shows a vector image from a 3D borehole seismic array and a single reflector. The actual reflector has a 20^o dip at an azimuth of 0^o.

3.6 Examples of Transformed images

The previous section derived the shape of reflection events in vector images, called vector image isochrons. In this section, the isochrons are used to transform the vector image, collapsing the energy of reflection events to the point corresponding to the actual orientation and position of the reflector as described in Section 3.3.3. After the transform, vector image events are more compact and symmetrical, and lead to spatial images with fewer artifacts.

3.6.1 Transformed surface seismic images

Examples in Section 3.4.3 showed that the energy in surface seismic vector images is located along the $\iota_d = 0$ contour, so only this contour is used in the transform.

Figure 3-20 shows the VII transform of the 2D surface seismic vector image in Figure 3-15. The energy has been focused to the point corresponding to the reflector. Figure 3-21 is the VII tranform of the dipping reflector image in Figure 3-16. The energy has been similarly focused, this time to the reflector dip of 20^o.

3.6.2 Transformed borehole seismic images

Figure 3-22 shows the VII transform of the 2D borehole seismic image in Figure 3-18. The energy has been focused to the proper reflector location, although there is a "tail" to one side. When the transformed vector image is summed into the final spatial image, which is a sum horizontally across the image in Figure 3-22, energy in this tail will cancel out.

Figure 3-23 shows the VII transform of the 3D borehole seismic image in Figure 3-19. The energy has been focused into the proper depth, dip and azimuth of the reflector, which had a dip of 10^o at an azimuth of 0^o.

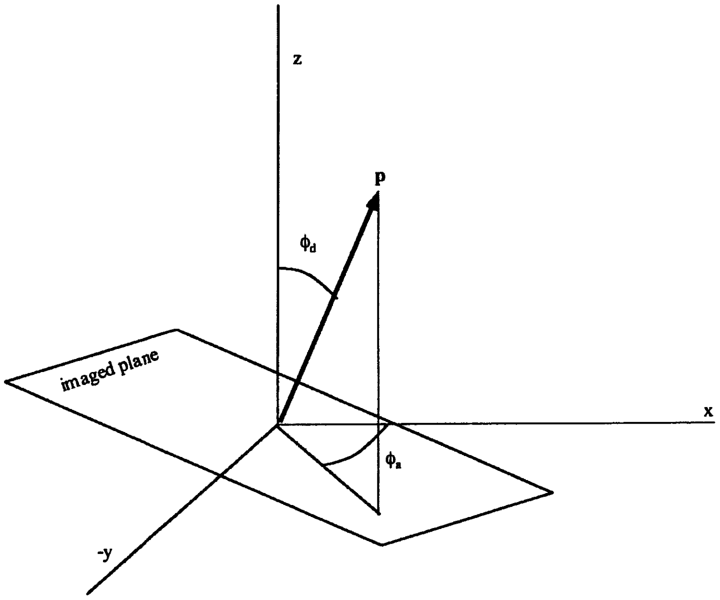

Figure 3-11: The geometry of the imaged plane. The angles ϕ_a and ϕ_d describe the orientation of **p**, the normal to the imaged plane.

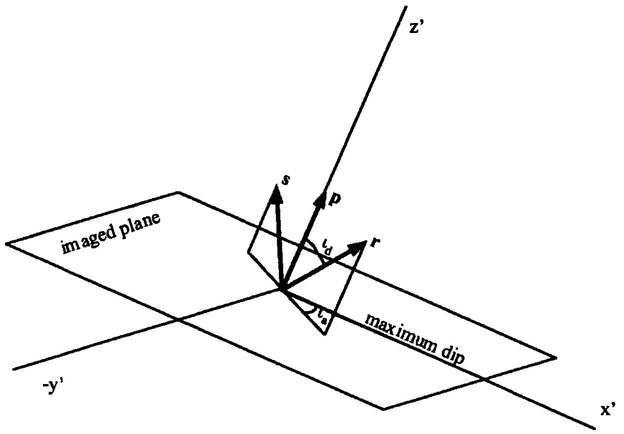

Figure 3-12: The prime coordinate system in which the reflector is horizontal. **p** is the image plane normal, ands and **r** are the normals to the incident and reflected rays. The angles ι_a and ι_d describe how the energy is incident on the plane.

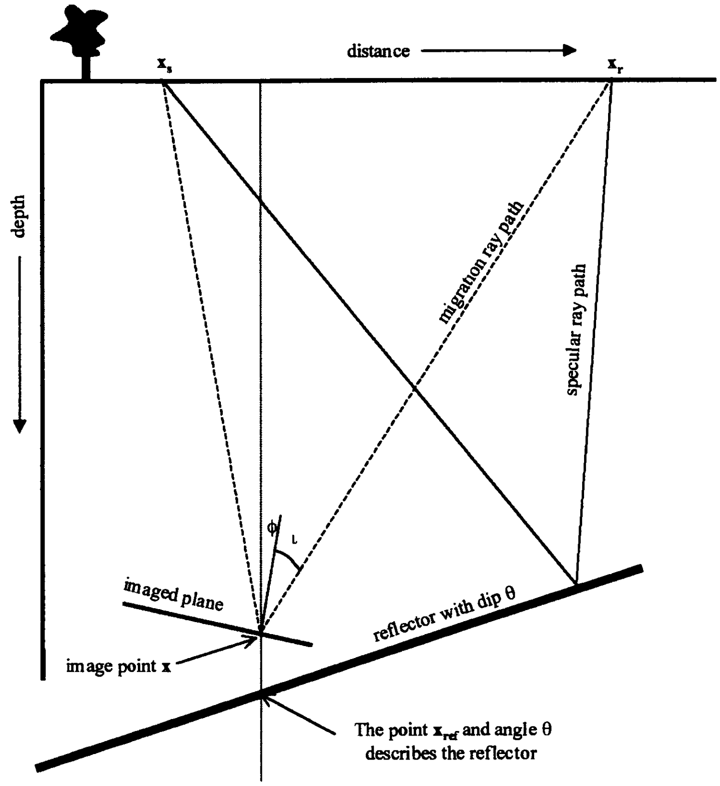

Figure 3-13: The principle used to derive the vector image isochrons for surface seismic arrays, see Section 3.4 for discussion.

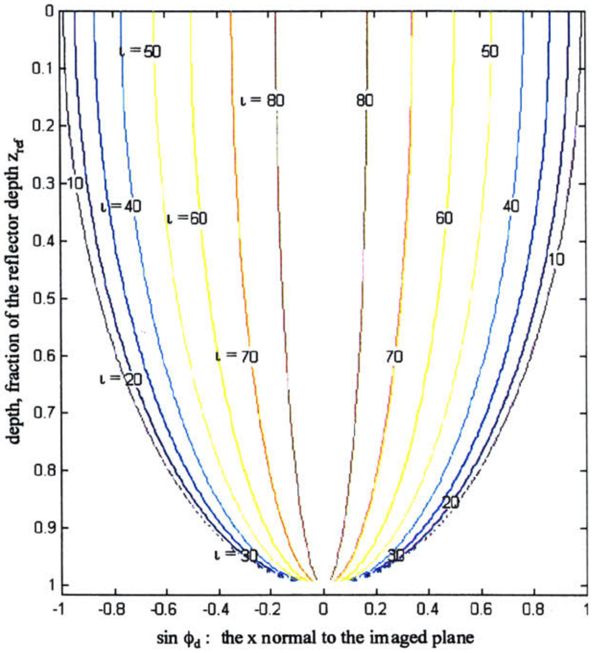

Figure 3-14: Contours of the migration incidence angles which will contribute to the image integral. The image will have the most energy where the contours are most closely spaced. This is at the point A which corresponds to the actual reflector position and orientation.

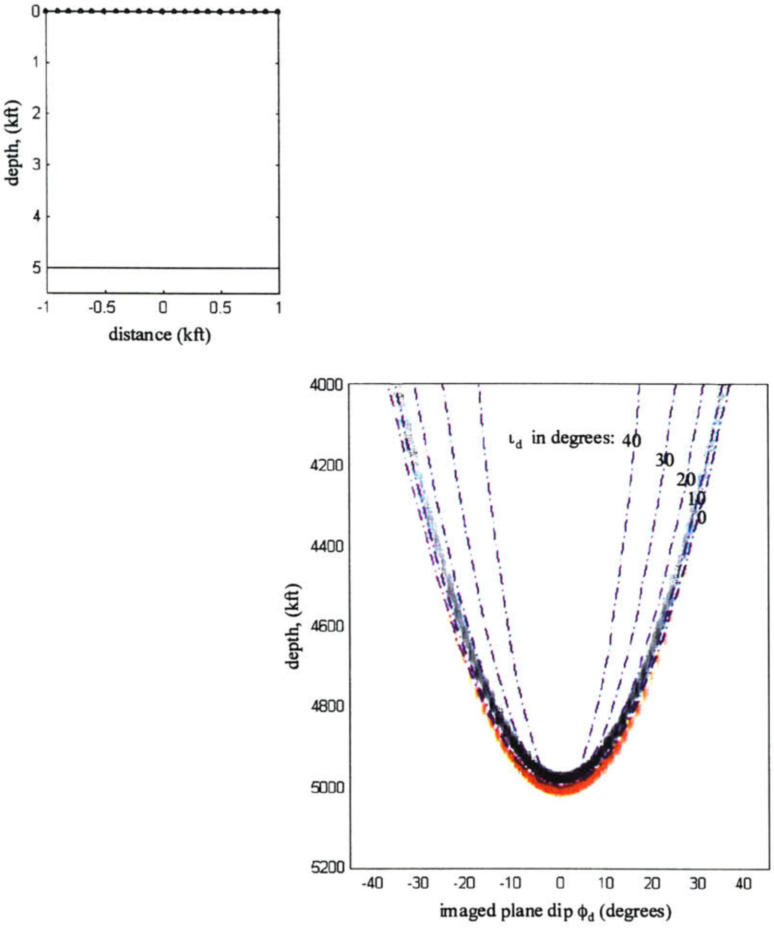

Figure 3-15: A vector image made with 2D synthetic surface seismic data with a flat reflector. The contours are isochrons for various values of the migration incidence angle.

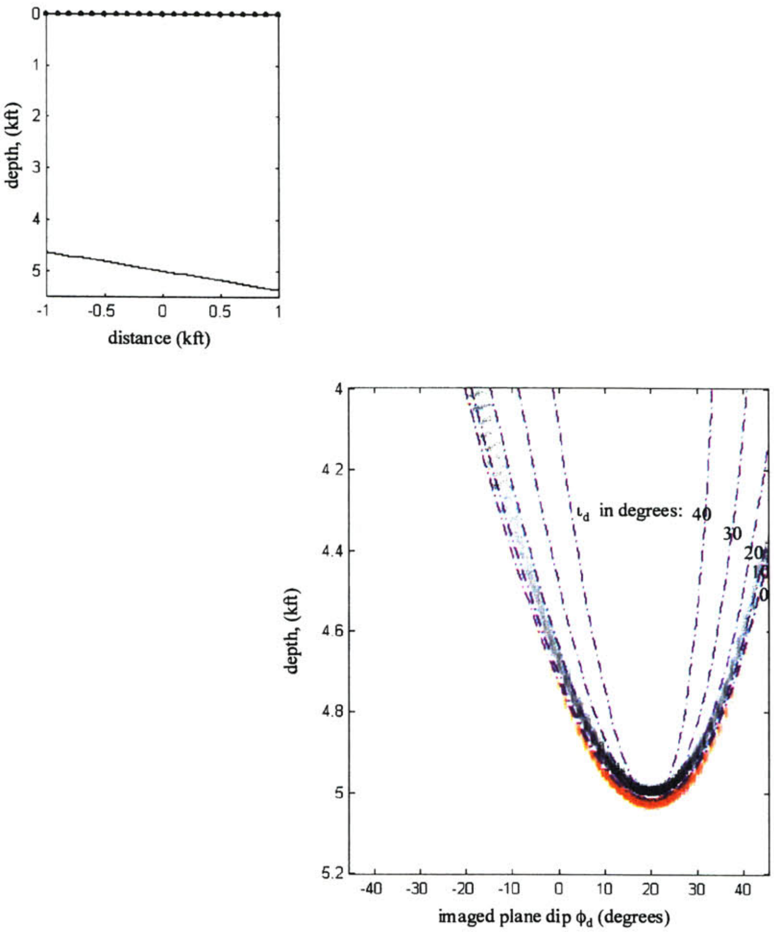

Figure 3-16: An image made with synthetic 2D surface seismic data for a reflector dipping at 20^o, with contours of the migration incidence angle ι_d.

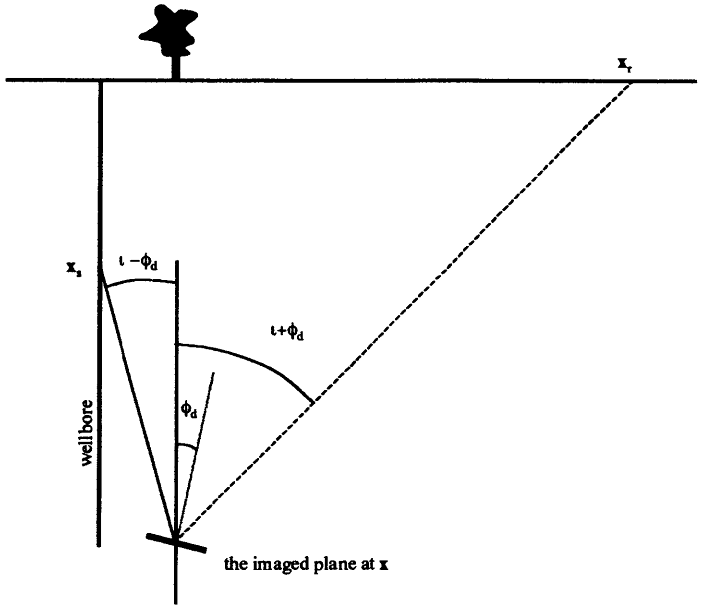

Figure 3-17: The geometry for borehole seismics. The source location is fixed, so that each imaged point and plane is imaged by a single receiver.

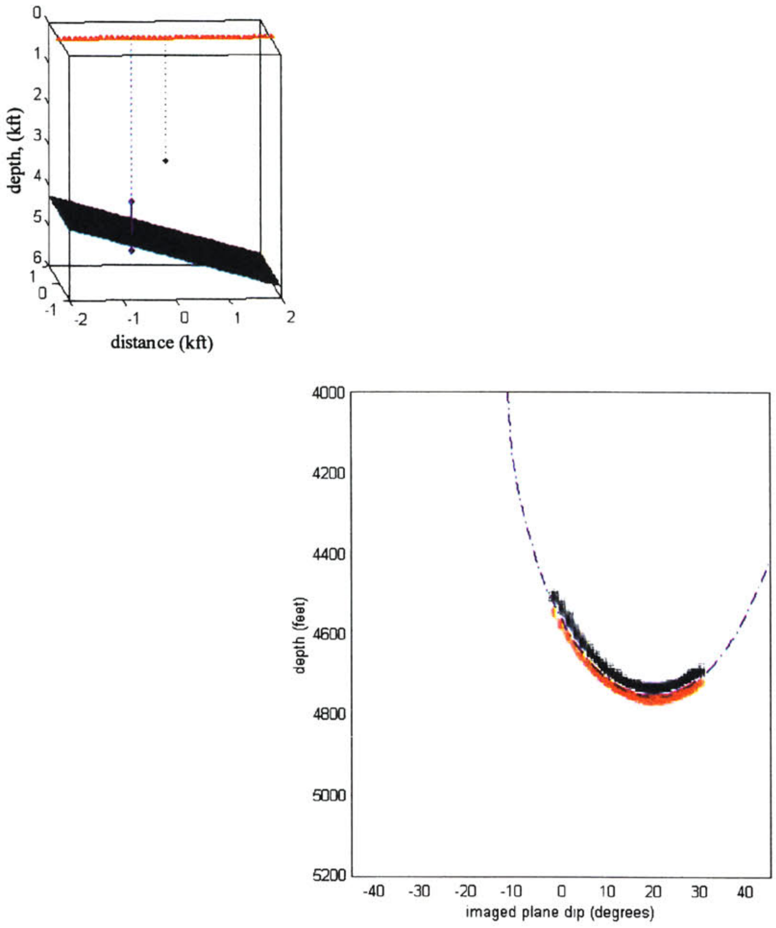

Figure 3-18: A vector image from a 2D single shot synthetic borehole seismic survey. The overlain isochron is the solution to 3.32, found numerically.

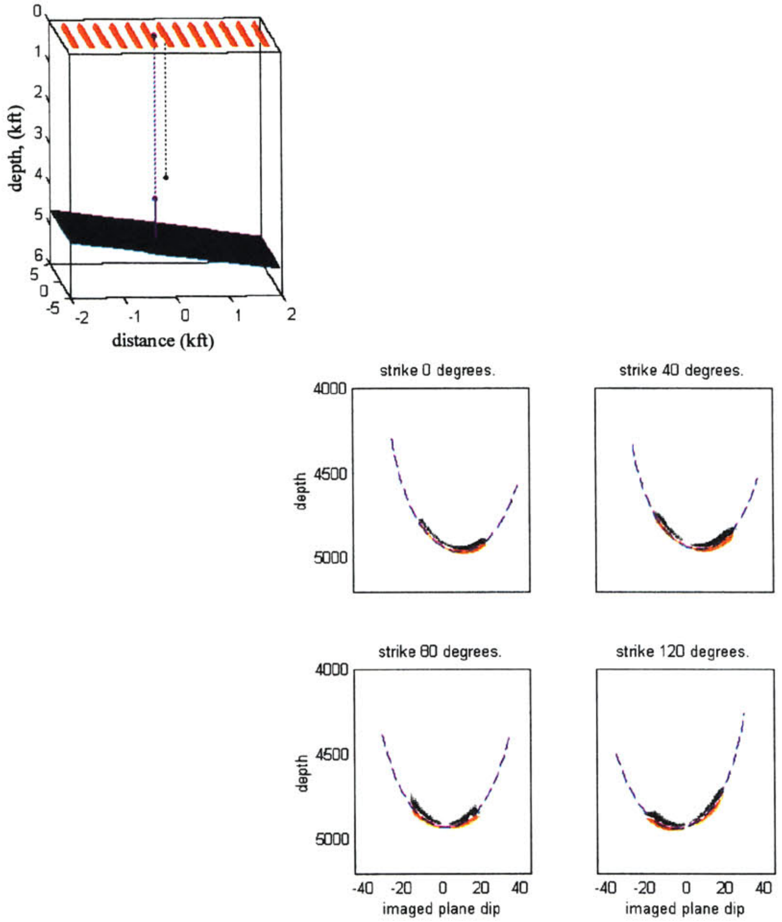

Figure 3-19: A vector image from a single shot synthetic 3D borehole seismic data; the dashed curves are vector image isochrons. The image x, y location is offset 200 feet (60 meters) from the shots in the well. The actual reflector has a dip of 10^oat a 0^o azimuth.

As an added test, a second 3D RVSP synthetic was made for a reflector with a non-zero azimuth. Figure 3-24 shows that the energy has been focused into the vector image slice with the azimuth of 100^o, which was the azimuth of the reflector normal in the model.

3.6.3 Multiple Reflectors

The 2D example used in Section 3.2 to compare surface seismic and borehole seismic arrays has the vector image shown in Figure 3-25. It transforms as shown in Figure 3-26. The final scalar image was shown in Figure 3-10.

The cause of the array artifacts can be seen in Figure 3-25. At the edges of the illumination, the events cut off sharply. The sum across imaged planes, given in Section 3.3.4, is a horizontal sum across the image. With a limited aperture array, there will be artifacts at the depths where the energy cuts off. An aperture limit will smooth out many of these edges, but at the cost of losing dipping reflectors. Further out from the well, these "edges of illumination" in the image will near zero dip, so the artifacts in the image will be present even with a narrow aperture.

3.6.4 Multiple shot depths in the borehole array

Figure 3-27 shows a 2D image made with a sparse array of downhole sources. The contribution of each shot to the image can be seen, and fits isochrons calculated by equating Equations 3.47 and 3.48 for the various shot depths. The image point is fairly close to the source array in depth, so there is a noticable difference between the isochrons for the different shot depths.

The ideal way to image in this case would be to migrate, transform, and sum one shot location at a time, then add the resulting images. However, since most of the energy lies where the isochrons for the various shot depths are close together, transforming once for a midlevel shot depth may be sufficent in many cases.

Transforming one shot at a time would be most necessary when the image location is far to the side of the well and near the shots in depth, as the isochrons in these cases are more spread. This can be tested by making an isochron plots before imaging.

3.6.5 Curving ray paths

In order to estimate the error caused by assuming straight rays, a flat reflector is imaged in two earth models shown in Figure 3-28. The first model has constant velocity, the second has a velocity which increases linearly with depth. The blocked velocity log from the Michigan test site is also shown. The slope of the velocity in Model 2 has been chosen to estimate the conditions at the test site.

Figure 3-29 shows images for the two models. The top plots show the ray paths for a single shot location. The isochron for Model 1 fits the image as expected, the isochron for Model 2 does not fit the image.

However, it does fit for imaged plane dips near the dip of the reflector. This suggests that inaccuries due to the assumption of straight ray paths can be minimized by limited the scope of the transform. For instance, the transform could sum along the isochron for a window of 10^o from the imaged plane dip being evaluated. This is indicated by the dashed lines.

3.6.6 The Resolution of the VII image

Figure 3-30 illustrates the reason for the loss of resolution in the VII image. The wavelet is stretched, similar to normal moveout (NMO) stretching, when the imaged plane dip doesn't equal the reflector dip. The stretching increases as the imaged plane dip is further from the reflector dip, so putting a limit on the scope of the VII transform, as discussed in the previous section, should improve the resolution of the

VII image.

3.7 Michigan Synthetics

The VII imaging method is put to a more rigorous test with a 3D synthetic data. A constant velocity 3D model, shown in Figure 3-31, was constructed to resemble the basic structure at the Michigan test site. Synthetic data was calculated for three surface receiver arrays: the crescent shaped random array used in the 1998 field study (discussed in Appendix A and Chapter 4), the intended full array, and a regular array which covers the same ground as the full array. These three arrays are shown in Figure 3-32.

Figures 3-33 through 3-35 show images made with the various arrays. In all cases, the VII transform has "cleaned up" array artifacts. The area within the reef is emptied of migration smiles, making it possible to see the internal structure of the reef (if it had any).

The images made with the regular and random arrays are nearly identical. Careful examination, maybe more than is possible with images on paper, show that the image made with the random array has a slightly more energy located on the reflector than in the artifacts, most notably on the deepest reflector in the GRT image. A large difference was not expected between these images, since the artifacts are due to the overall aperture of the array and not the spatial distribution of the receivers.

The VII method has evened out the reflectors slightly; the brightest part of the reflector extends further out from the shot locations. The shape of the top of the reef is not obvious with either method because the step in the reef is smaller than the wavelet. But the VII image is easier to interpret than the GRT image because of the absence of array artifacts.

3.8 Derivation: an expression for ray path length in 3D

An expression is needed for the traveltime of a reflected ray in 3D given a constant velocity earth, a source location $\mathbf{x_s} = [x_s, y_s, z_s] = [0, 0, z_s]$, a receiver location $\mathbf{x_r} = [x_r, y_r, z_r] = [x_r, y_r, 0]$, a planar reflector described by its depth at the origin d the azimuth θ_a and dip θ_d of its normal.

This problem is solved in a rotated coordinate system where the reflector is flat, so that the source, receiver and image point are all in the same vertical plane. Then the expression 3.21 from Wyatt and Wyatt (1981) is applied.

The rotation into the prime coordinate system where the reflector is flat is given in Equation 3.13. The inverse rotation is

$$R'_{zy} = R'_z R'_y = \begin{bmatrix} \cos\phi_d & 0 & -\sin\phi_d \\ 0 & 1 & 0 \\ \sin\phi_d & 0 & \cos\phi_d \end{bmatrix} * \begin{bmatrix} \cos\phi_a & \sin\phi_a & 0 \\ -\sin\phi_a & \cos\phi_a & 0 \\ 0 & 0 & 1 \end{bmatrix} \tag{3.55}$$

In the prime coordinate system, the source and receiver coordinates are:

$$x'_r = R'[x_r, y_r, 0] \tag{3.56}$$

$$= \begin{bmatrix} (x_r \cos\theta_a + y_r \sin\theta_a)\cos\theta_d \\ -x_r \sin\theta_a + y_r \cos\theta_a \\ (x_r \cos\theta_a + y_r \sin\theta_a)\sin\theta_d \end{bmatrix} \tag{3.57}$$

$$x'_s = R'[0, 0, z_s] = [-z_s \sin\theta_d, 0, z_s \cos\theta_d] \tag{3.58}$$

The depth of the reflector in the primed coordinate system is:

$$\begin{aligned} d' &= R'(d - x\cos\theta_a \tan\theta_d - y\sin\theta_a \tan\theta_d) \\ &= d\cos\theta_d \end{aligned} \tag{3.59}$$

In the prime coordinate system the reflector has zero dip, and since the source is at the x, y origin, $z'_s = z_s$, and the distance formula Eq. 3.21 becomes:

$$s_{sr}^2 = (x'_s - x'_r)^2 + z_s^2 + 4d'_o(d'_o - z_s) \tag{3.60}$$

Plugging Eq. 3.56 and Eq. 3.58 into Eq. 3.60:

$$\begin{aligned} s_{sr}^2 = ((x_r - x_s)\cos\theta_a + (y_r - y_s)\sin{\theta_a}^2 + z_s^2 + 4d^2\cos{\theta_d}^2 \\ +4(z_s - d)((x_r - x_s)\cos\theta_a + (y_r - y_s)\sin\theta_a)\sin\theta_d\cos\theta_d \end{aligned} \tag{3.61}$$

If the azimuth angles are set to zero, Eq. 3.61 equals the 2D expression Eq. 3.21.

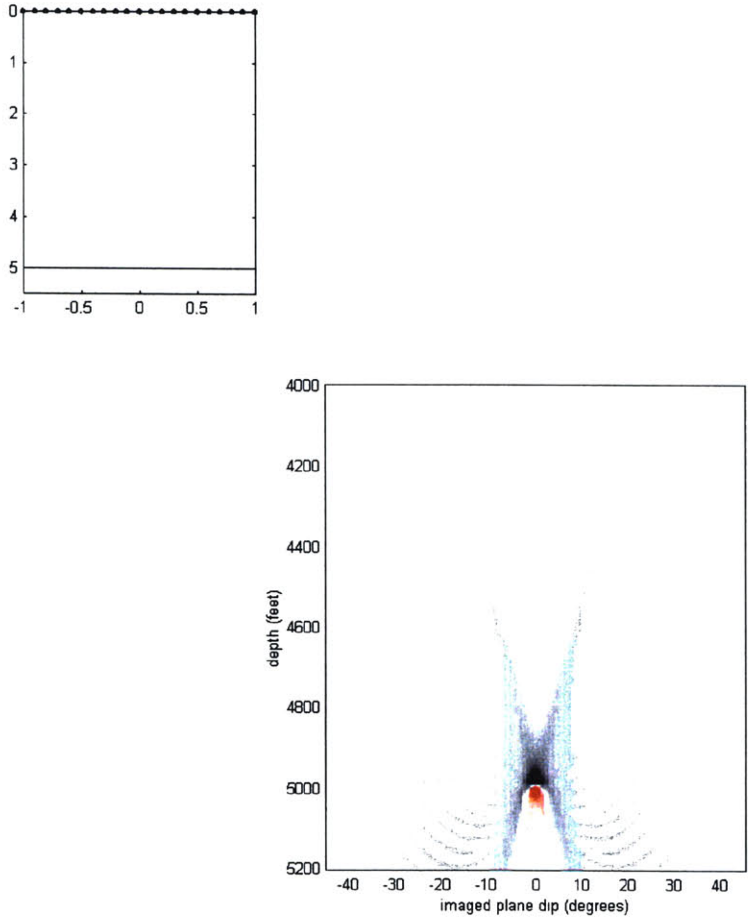

Figure 3-20: The transform of the 2D surface seismic image in Figure 3-15. Aliasing causes the "rippling" effects between 5000 and 5200 feet depth.

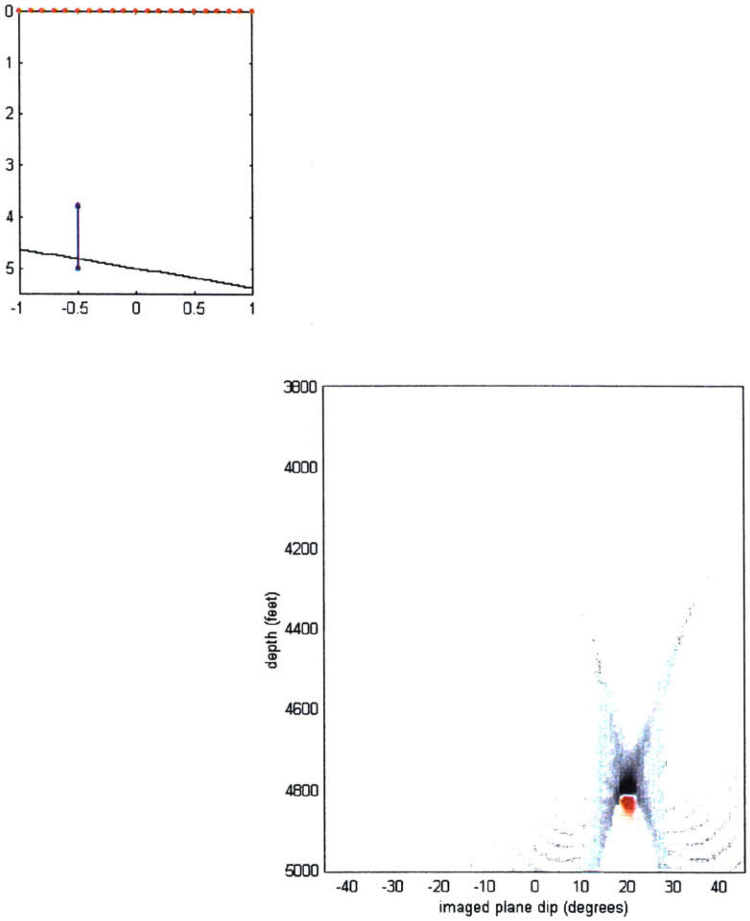

Figure 3-21: The transform of the 2D surface seismic image in Figure 3-16.

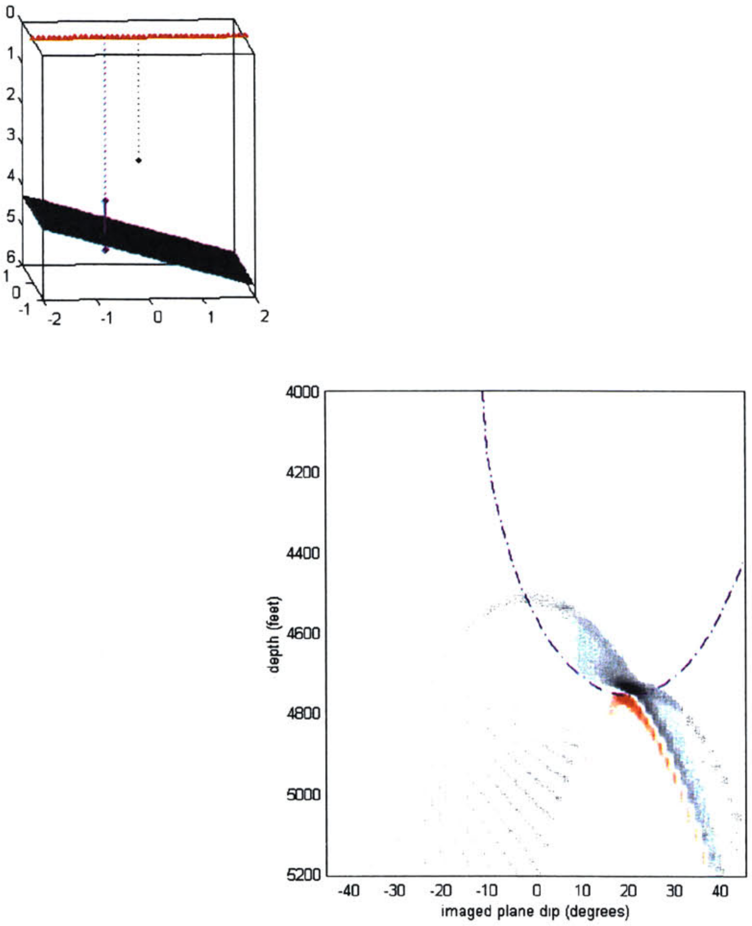

Figure 3-22: The transform of the 2D borehole seismic image in Figure 3-18.

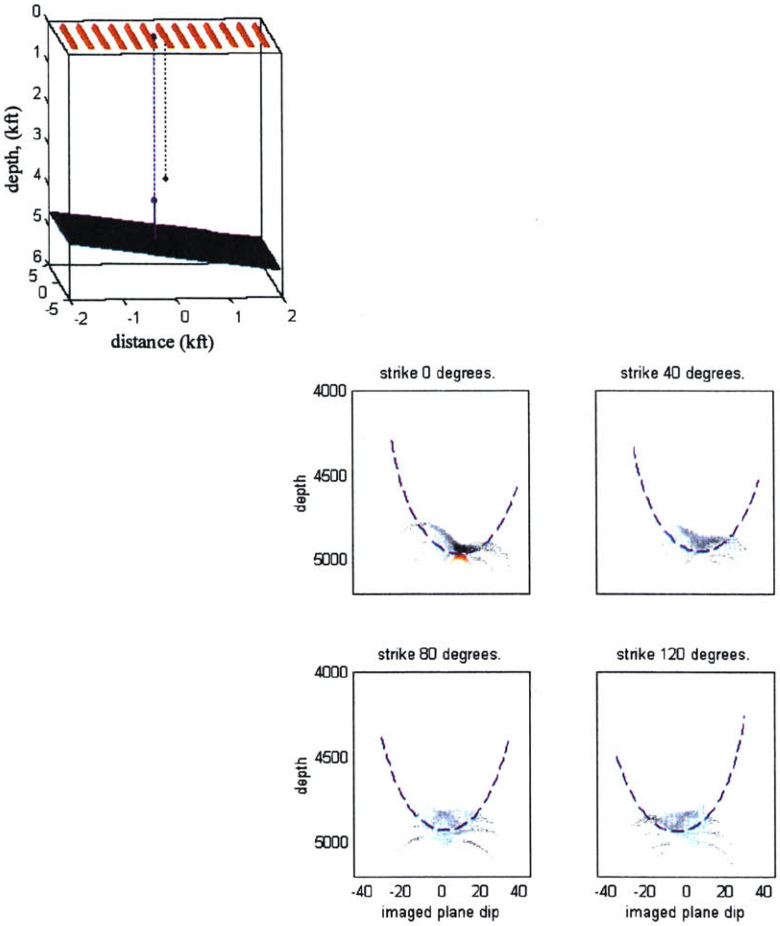

Figure 3-23: The transform of the 3D borehole seismic image in Figure 3-19.

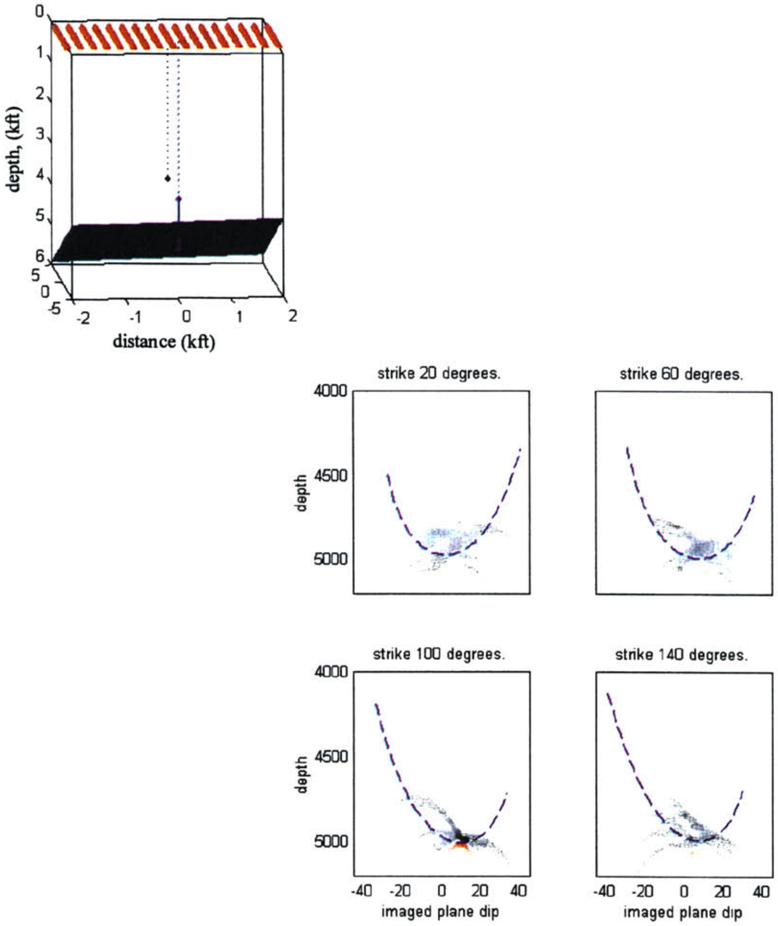

Figure 3-24: A transformed 3D borehole seismic image, similar to the image shown in 3-23, but with reflector has an azimuth of 100^o.

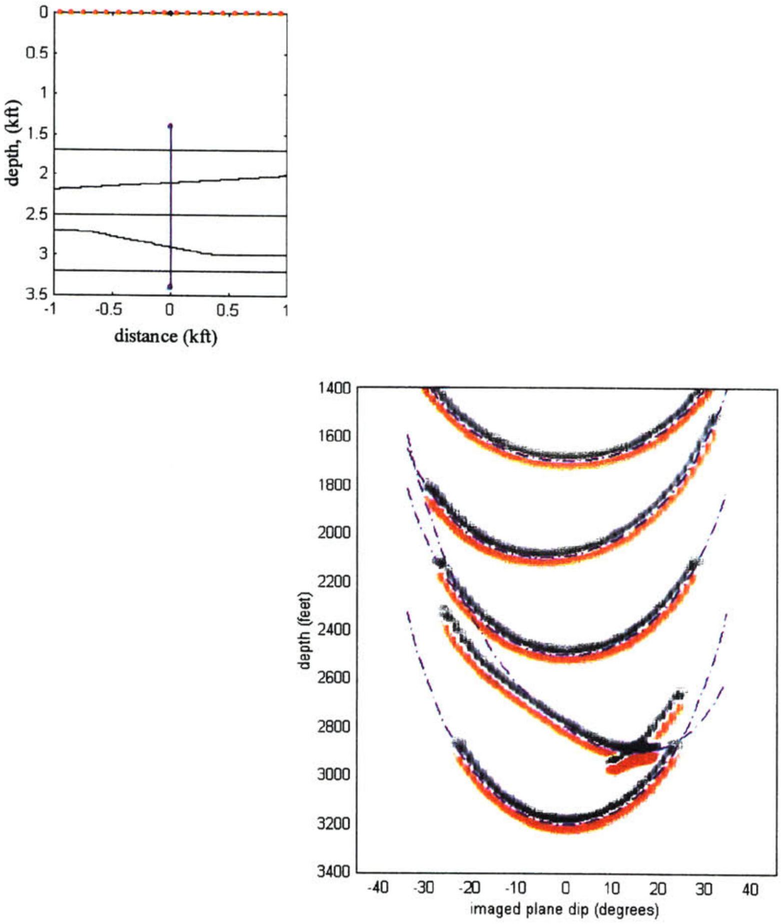

Figure 3-25: The vector image of the synthtic example used in Section 3.2.

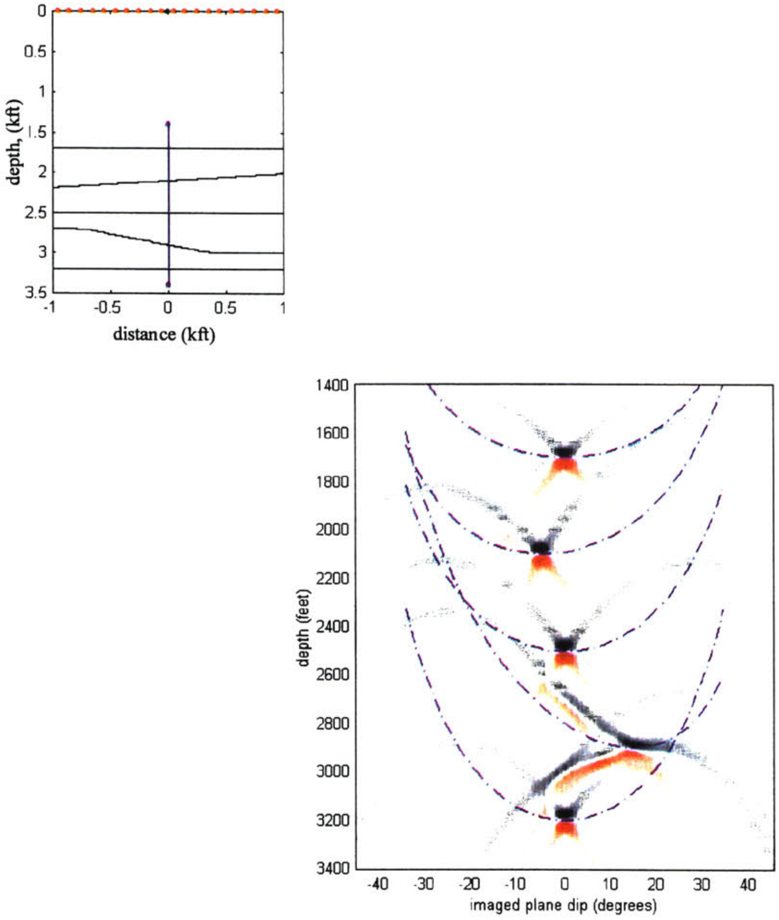

Figure 3-26: The transformed vector image from Figure 3-25. The final image was shown in Figure 3-10.

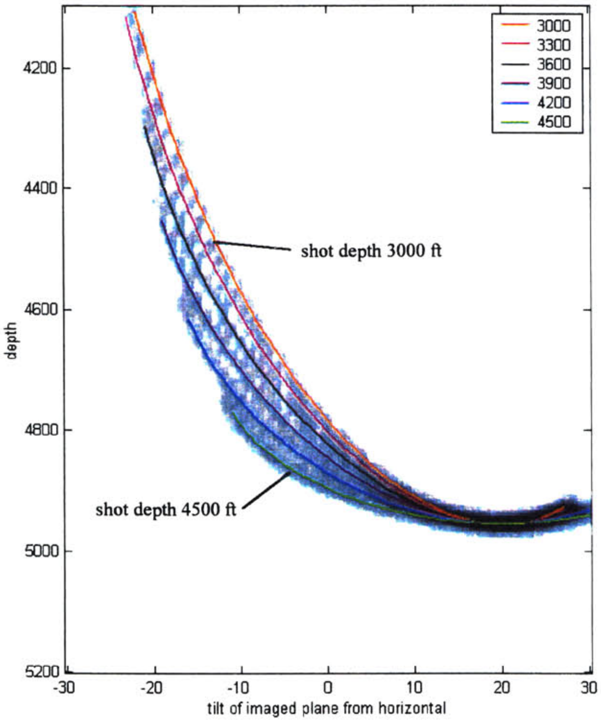

Figure 3-27: A vector image from synthetic 2D borehole seismic data, in grayscale. The overlain curves are vector image isochrons for different shot depths.

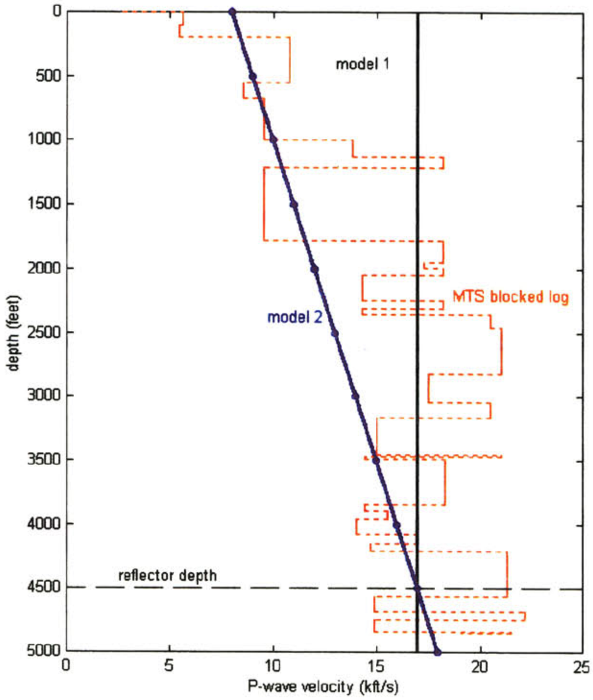

Figure 3-28: Two models used to estimate inaccuracies due to the assumption of straight ray paths. Model 1 is constant velocity, Model 2 is chosen to approximate conditions at the Michigan test site, shown in dashed lines.

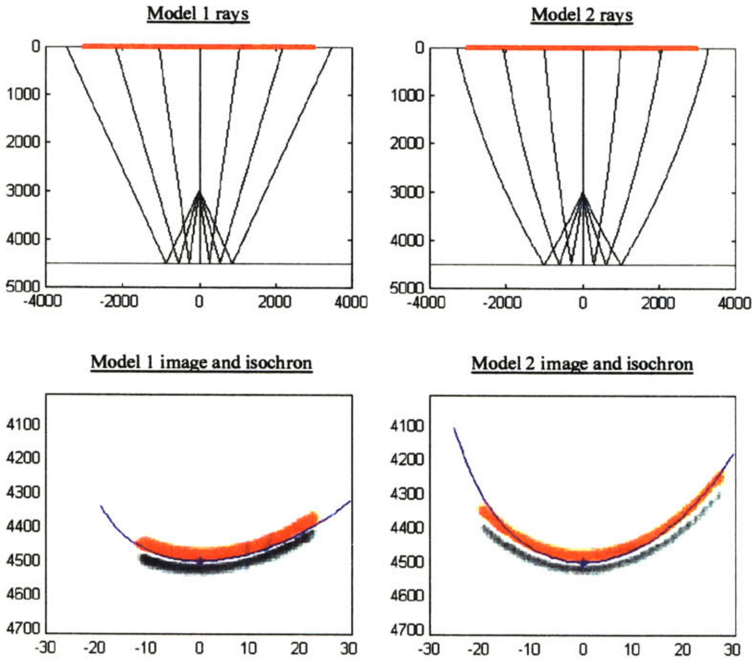

Model 1 rays

Model 2 rays

Model 1 image and isochron

Model 2 image and isochron

Figure 3-29: Images made from the models in Figure 3-28. The misfit due to the curving rays can be minimized by limiting the extent of the transform.

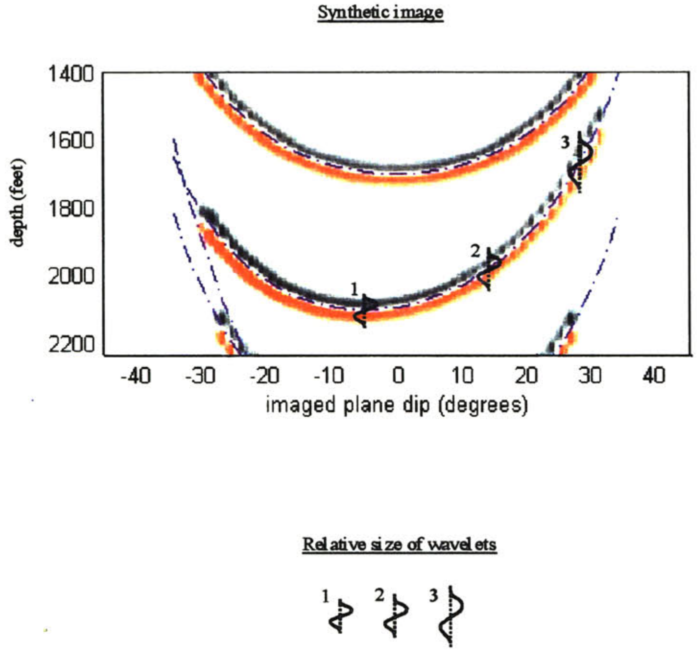

Figure 3-30: A portion of the untransformed vector image in Figure 3-25 shows how the wavelet stretches, causing the loss of resolution in VII images.

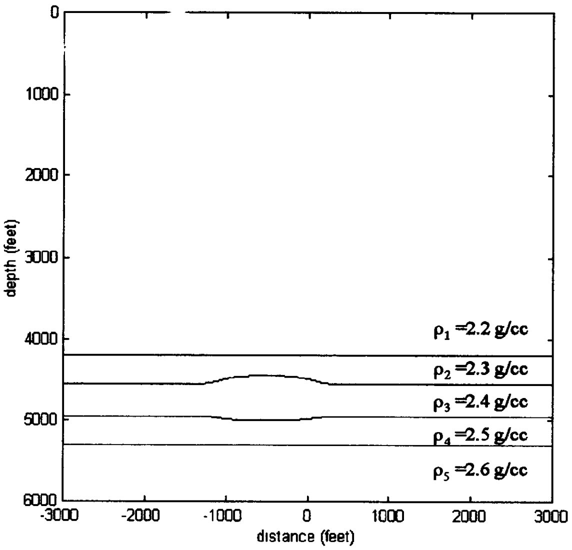

Figure 3-31: North-south slice through the model used to create the 3D synthetic data. The velocity is constant.

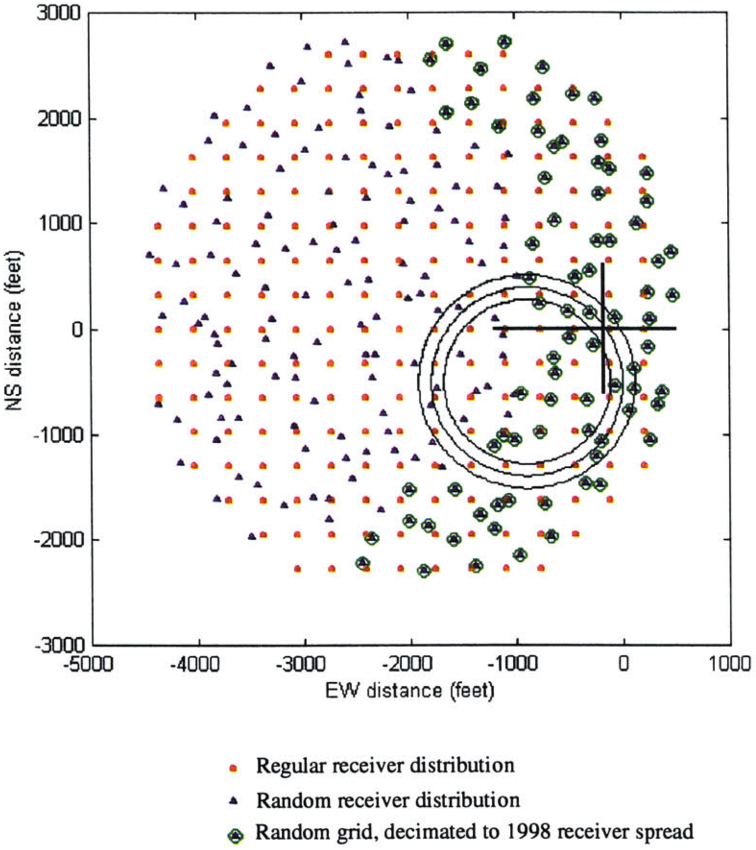

Figure 3-32: Array geometries for the 3D synthetic data. The reef outline is shown as black circles, and the heavy black lines show the location of image slices. The wellhead is at 0,0.

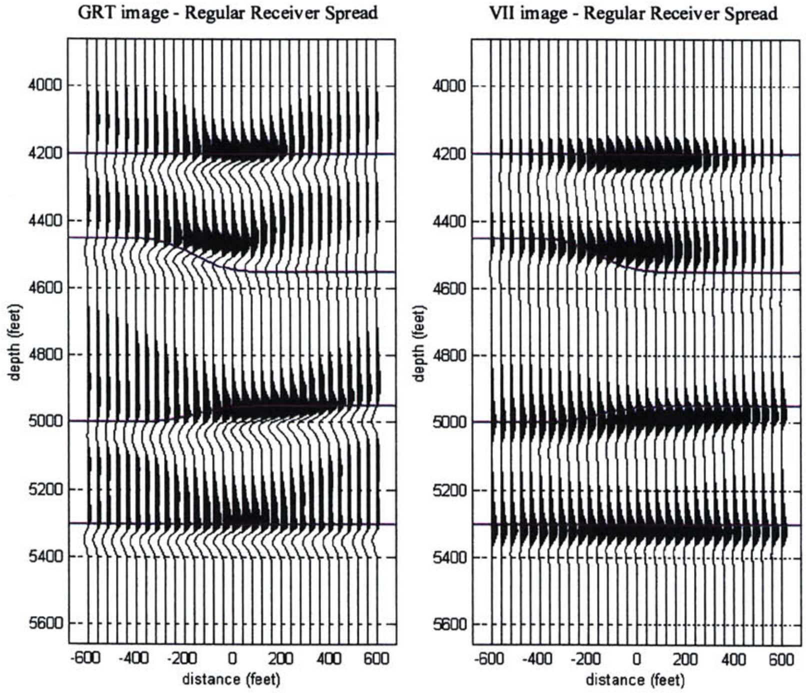

Figure 3-33: A north-south slice of the image with the regular array, to the left is the conventional image, to the right is the image made with the VII transform.

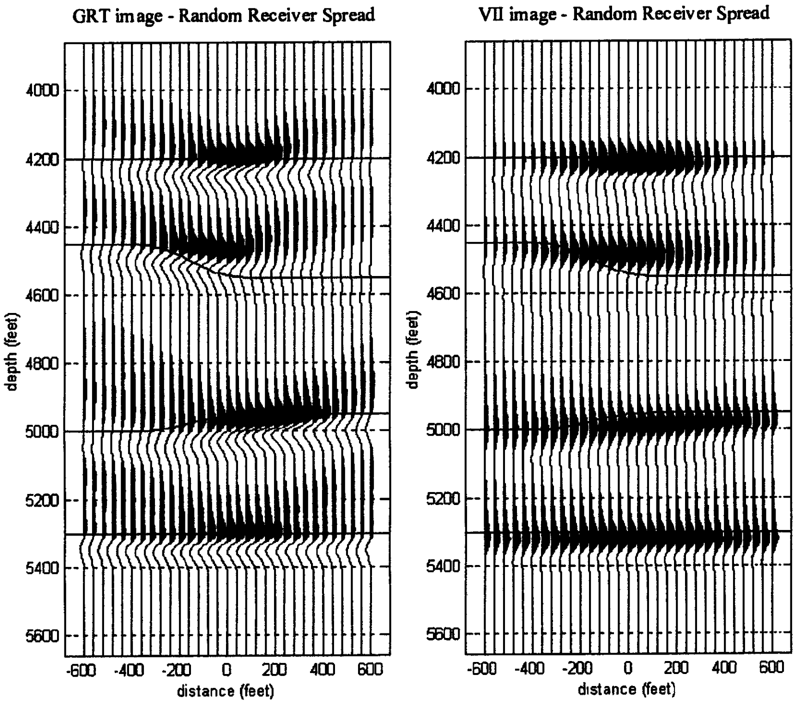

Figure 3-34: A north-south slice of the image with the random array, to the left is the conventional image, to the right is the image made with the VII transform.

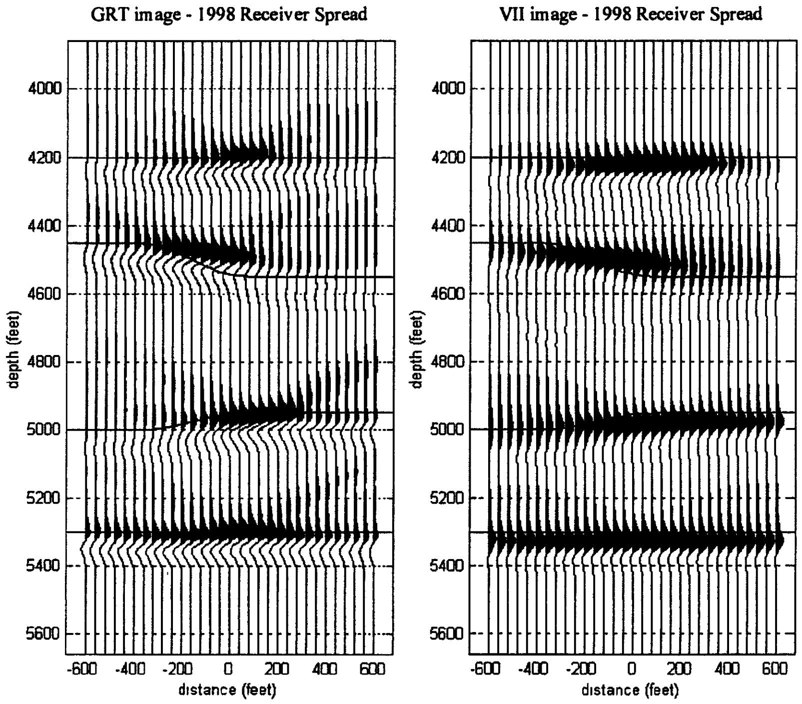

Figure 3-35: A north-south slice of the image with the random array, decimated to have the same coverage as the 1998 Michigan field data, to the left is the conventional image, to the right is the image made with the VII transform.

Chapter 4

Field data imaging results

4.1 Introduction

This chapter presents field data images made with the reverse VSP data collected in a 1998 research program by the MIT-ERL Reservoir Delineation Consortium. The focus of this chapter is on displaying imaging results and evaluating the new vector image isochron (VII) imaging method. For reference, Appendix A contains a discussion of the Michigan test site and the goals of the 1998 study, Chapter 2 goes through the processing steps applied to the field data, and Chapter 3 derives the VII imaging method.

This chapter is separated into three sections. The first contains this short introduction, the second shows images made with the GRT imaging method of Miller et al. (1987), which is referred to as the conventional method, and the third section shows images made with the VII method.

In Section 4.2, which contains the conventional migration images, issues such as fold correction, the resolution of the array, aperture limitation, and the difference between using 1D and 3D earth models for the traveltime calculation are addressed.

At the end of Section 4.2, the conventional images are compared to previous results from the Michigan test site, showing that the downhole source, array geometry, and processing scheme of the 1998 MIT-ERL research program have combined to produce images of unprecedented resolution for this region of northern Michigan. However, array artifacts make the images difficult to interpret. The geophone array is very limited, as discussed in Section 2.2 and shown in Figure 2-3.

Section 4.3 shows images made with the (VII) imaging scheme and compares them to their GRT migration counterparts. Although there is some cost in resolution, images made with VII migration show better continuity along reflectors and indicate clearly which structures are illuminated, allowing for more dependable interpretations.

4.2 GRT migration results

The map on Figure 4-1 shows the location of the image slices which will be shown in this chapter relative to the approximate position of the reef. The focus will be on the three north-south slices, since the array is very narrow in the east-west direction and resolution is poor on those slices, as discussed in Section 4.2.3.

4.2.1 Geologic interpretation

Before discussing issues related to the migration method, structural details of the imaged portion of the test site should be identified. Detailed discussion of the test site geology is left to Appendix A; for reference, Figure A-11 shows a cartoon of the test site lithology.

Figure 4-2 is a velocity model of the structure of the reef and surrounding layers deduced from previous studies. The separation of the reef into two parts is due to a channel which was seen in the a 1984 surface seismic study (Figure A-7). A few offset VSPs have also suggested the presence of this channel. Fine structural details, such as the pinchout of an anhydrite between the A2 salt and the A2 carbonate, are based on the fact that the A2 salt is present in off reef well logs but absent over the reef. The exact details of the pinch out are purely hypothesized.

Several interfaces are marked at the right edge of the middle slice: Event A at 4200 feet is carbonate stringers in a shale. Event B is the most obvious indicator of the presence of the reef: it is the interface between the B salt and the A2 carbonate which overlies the reef, stepping down off the reef to the north. The bottom of the reef E, which isn't expected to be a strong reflector, is at about 5000 feet. All events beneath the reef bottom are expected to be flat, such as the top of the Cabot Head shale marked F.

Events C and D are the tops of the A2 salt and the A1 anhydrite, which are high velocity contrasts in the off reef structure and pinch out over the reef. The A1 anhydrite has been conjectured to extend laterally into the reef (Jodry, 1969). If it does, it could be a barrier in fluid flow, trapping hydrocarbons in pockets within the reef.

Events A through F will be marked in all the figures in this chapter, and allow for comparison between the results of the different imaging schemes.

Figure 4-3 is a image formed by conventional Kirchhoff migration of the 1998 RVSP field data with a 15^o aperture limitation (the aperture limit is imposed on the dip of the imaged plane) and traveltimes calculated in the 3D earth model. There is a general trend in the image for events to dip upward at the edges: this is due to the limited nature of the imaging arrays. These "smiles" can be followed through the image, interfering with what are known to be flat reflectors, making detailed interpretation difficult.

The shallow reflectors, such as Event A, are flat and fairly even. Event F, however, shows an interruption at about -300 feet distance, which is likely due to an artifact from a deeper reflector.

The location of the reef can be clearly seen in the step of event B, but the reef bottom is not visible. Events C and D appear to dip downward into the reef, and appear to extend as far into the reef as the array can illuminate, or least until the upcurving artifactrs at the southern (left) edge of the image interfere.

No images previously produced at the Michigan Test Site have had high enough resolution in 3D to pick up a detail like the extent of the A1 salt, Event C.

4.2.2 The Fold correction

Figures 4-4 and 4-5 show the fold of the survey, found by ray tracing through a flat layered earth model; Figure 4-4 has vertical north-south slices through the image cube, and Figure 4-5 has a horizontal slice at the reef top depth.

This fold map can be used to even out the brightness of the reflectors in the final image by dividing the image by the fold map. Portions of the image with low fold, less than 10 reflections per 25x25 foot (8x8 meter) bin, are cropped.

Figure 4-6 is a medium aperture conventional migration image of the reef, without the fold correction. This should be compared to Figure 4-3, which is the same image with the fold correction applied. The shallowest reflectors show the most obvious difference: they are evened out and can be followed further from the wellbore when the correction has been applied. The illumination of the deep reflectors was less uneven to begin with, so they are less affected by the correction.

Unless otherwise stated, all conventional migration images in this chapter will have the fold correction applied.

4.2.3 East-West versus North-South slices

Figure 4-7 shows east-west (EW) slices of the image cube at the locations marked on Figure 4-1. This is the same medium aperture conventional migration image which was shown in Figure 4-6. The edge of the reef can be seen in these slices: the B salt - A2 carbonate reflector is at 4500 feet in the southern slice (at -100 NS), then steps down to just below 4600 feet in the northern slice (at +140 NS).

However, the array is so narrow in the EW direction that only a small part of the earth is illuminated, so that each slice is dominated by migration "smiles." For this reason the EW slices of the image are not very informative. Most imaging results will be shown as NS slices.

4.2.4 Aperture limitations

Figures 4-8 and 4-9 are north-south (NS) slices of images made by conventional Kirchhoff summation migration of the Michigan RVSP data, with traveltimes found in a flat layered earth. The three figures were made with aperture limits of 30^o and 5^o, as compared to 15^o in Figure 4-3. The aperture limit is a limit in the imaged dip which can contribute to the image.

Figure 4-8 has a wide migration aperture of 30^o, and migration artifacts (smiles) are a problem. The edges of the image are dominated by up-curving events. These events are suspiciously similar to the artifacts seen in the synthetic examples of Chapter 3, artifacts which were found to be directly caused by the borehole array geometry and the assumptions made in Kirchhoff migration.

Figure 4-3 narrows the aperture to 15^o. In this image the wedge shape of the reef top is clearly visible, and the step down off the reef is fairly continuous.

The image in Figure 4-9 was created with a narrow migration aperture of 5^o. Event F shows more continuity then in the previous images, since the narrow aperture prevents energy from deeper reflections from interfering. In general, reflection events appear fairly flat in this image, except in the furthest west slice, at -180 feet EW, which has a step in event B and a clearly downsloping event C.

The medium aperture results in the best image, including enough dipping energy to produce a meaningful image without begin taken over by sloping artifacts.

4.2.5 GRT migration with the 3D earth model

Figures 4-10 through 4-12 are comparable to Figures 4-8 through 4-9 except the travel times and ray angles were calculated in a 3D earth model. The additional computation time is considerable: a few days as opposed to the few hours needed for migration with the flat layered model. Figure B-3 shows the diffence in traveltimes for the two earth models.

Comparison of Figure 4-10 to Figure 4-8 shows that, as expected, the reflectors above the reef are unchanged by the use of the 3D model. Event E below the reef, which well logs and previous studies show to be flat, is flatter when the 3D earth model is used. Since velocities in the reef are higher than the non-reef structures, the image made with the flat layered model had pulled up event E.

The medium aperture image in Figure 4-11 shows increased continuity in almost all reflectors as compared to the wide aperture image. In particular, all the reflectors between events E and F are improved. These reflectors were difficult to follow through the image made with the flat layered model, as in Figure 4-3.

The narrow aperture image in Figure 4-12 doesn't have much reflected energy within the reef. This is due to the curvature of the rays as they pass through the top of the reef, and is especially obvious in the narrow aperture image. The rays that image horizontal planes are focused in a narrow region of the 3D earth model. This is an extreme case to illustrate the tradeoff of limited aperture: artifacts are removed, but so is much desired energy.

4.2.6 Comparison to previous results

Figure 4-13 shows how this image compares with a previous study at the Michigan test site. The VSP on the left was collected in 1983, and imaged the western edge of the reef with maximum signal frequencies of around 100 Hz. The VSP image shows a flat reflector at 4100 feet, a stepping reflector at the top of the A2 carbonate, a reflector within the reef, and some events below the reef which tend to curve up at the edge of the image.

The reverse VSP image on the right not only has much higher resolution than the VSP, but is only one slice in a three dimensionsal image cube. This comparison speaks highly for the field methods, borehole source, and processing scheme applied to the data.

4.2.7 GRT migration: summary

Because of the high frequency content of the data, conventional migration of the Michigan RVSP data yields images of good resolution. The limited nature of the geophone array yields very little resolution in the east-west slices of the image cube, but the north-south slices illuminate a corner of the reef, showing structural details which have not been seen before in 3D.

The migration aperture, or limit on the dip of imaged planes, is vital to the quality of the image. Too wide an aperture allows artifacts in the image, masking reflectors. Too narrow an aperture can remove the desired reflected energy, leaving blank spots in the image. An aperture of 15^o works well with this data.

The presence of flat reflectors beneath the reef structure provide a test of the validity of the model used to migrate the data. Traveltimes calculated with a 1D model do not include high velocities within the reef, so the deep reflectors are not flat. Images produced with the 3D model show improvement in this respect.

However, the images are difficult to interpret because of the incompleteness of the receiver array. Even the central portion of the image with the highest fold shows artifacts which interfere with reflectors.

4.3 Results with the VII method

This section shows images made with the new migration method outlined in Chapter 3 of this thesis. Images are made with traveltimes in a 1D and 3D earth model, and shown with and without the fold correction, although the fold correction isn't expected to apply to the VII images as well as it did the GRT images. The examples in Section 3.7 showed that the VII method evens the illumination of the image.

4.3.1 VII Migration with the 1D earth model

Figure 4-14 and 4-15 show north-south slices of the image, 4-14 before the fold correction, 4-15 after. The image was formed by migrating all the data into a vector image, then transforming once for an average value of source depth. As discussed in Section 3.6.4, not transforming for multiple shot depths will have the most adverse effect of the portion of the image closest to the shots in depth.

In both 4-14 and 4-15, Event F in the deepest part of the image, furthest from the borehole array, is now a single flat reflector, not broken up by artifacts from deeper reflectors as it was in the conventional migration images (Figure 4-8). The shallow event A, however, is worse than it was in the conventional images.

The fold correction has a similar effect as it did the conventional migration images, making the reflectors easier to follow to the edges of the iamge grid, and providing a way of knowing where to crop the image.

Note that all the events seem to slope down to the north. Well logs show that there is essentially no dip in the layers surrounding the reef, as interfaces tend to be about 10 feet (3 meters) deeper in the Stech well to the west than in the Burch well in the east.

The wells exist in an east to west line, so provide no direct measurement of layer dips in the north-south direction. But basinward is south, so a dip down to the north is not likely. It is more likely that the apparent dip of events in Figures 4-14 and 4-15 are due to not including the relatively high velocities of the reef structure in the migration.

4.3.2 Migration with the 3D earth model

Figures 4-16 and 4-17 show the VI migration image with traveltimes in the 3D earth, without and with the fold correction. As in the conventional migration images, ray tracing through the high velocities in the reef has flattened out Event F and all the reflectors beneath the reef.

Event A and all the reflectors above the reef are not as flat as they were in the conventional migration image. As discussed above, this may be due to not transforming for each shot depth separately, or it could be a problem caused by the constant velocity earth assumption involved in the derivation of the vector image isochrons. In any case, this portion of the image grid is actually above some of the shot points, as the borehole array extends to 4500 feet and the top of the image grid is 4000 feet. For this reason, the top of the image is the most prone to error caused by the assumptions made in the derivation of the vector image isochrons.

4.3.3 The VII imaging method: summary

Figure 4-16 and 4-17 show north-south slices of the image, 4-16 without and with the fold correction. The image was formed by migrating all the data into a vector image, then transforming once for an average value of source depth.

In general, all reflectors have lost a degree of sharpness. This is an unfortunate effect of the VII transform: it inherently involves running a mean filter over the image. Also, bright reflectors, such as the reef top and Event F, have become much brighter, so that dim reflectors wuch as those between Events E and F are more difficult to see.

In both 4-16 and 4-17, Event F in the deepest part of the image, furthest from the borehole array, is now a single flat reflector, not broken up by artifacts from deeper reflectors as it was in the conventional migration images. The shallow event A, however, is worse than it was in the conventional images. As discussed in Section 3.6.4, not transforming for multiple shot depths will have the most adverse effect of the portion of the image closest to the shots in depth.

The poor quality of the shallow reflector could also be an effect of the assumption of constant velocity made in the isochron derivation. This would cause more error at the top corners of the image grid where the raypaths are less vertical, therefore have more curvature.

The fold correction has a similar effect as it did the conventional migration images, making the reflectors easier to follow to the edges of the image grid, and providing a way of knowing where to crop the image. However, the VII method has already evened out thei mage a little, so the fold correction does a little too much.

Event C is slightly flatter in the VII image than it was in the GRT image. Event E fades out and begins to curl up at the western (left) edge of the image, suggesting that this is the limit of the illumination of the array. It seems likely then that Event

C also extends into the reef, at least as far as the array can illuminate.

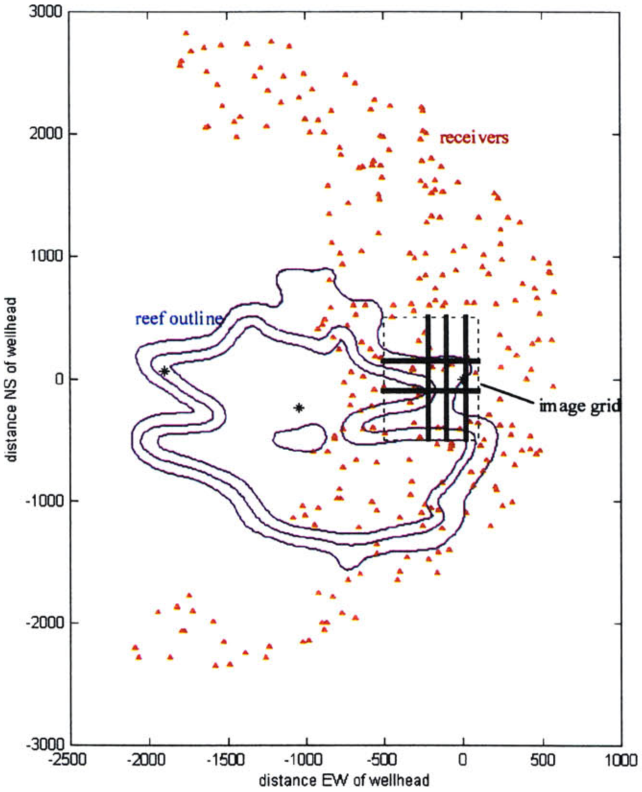

Figure 4-1: Location of field data image slices, shown in heavy black.

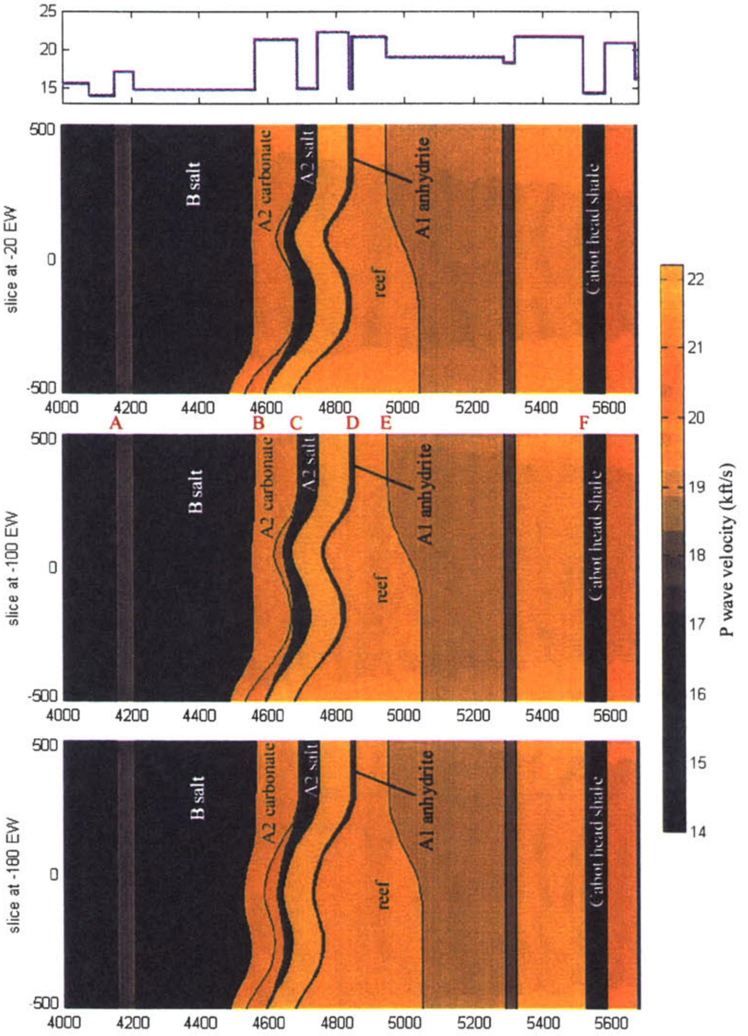

Figure 4-2: Earth structure from well logs and previous studies.

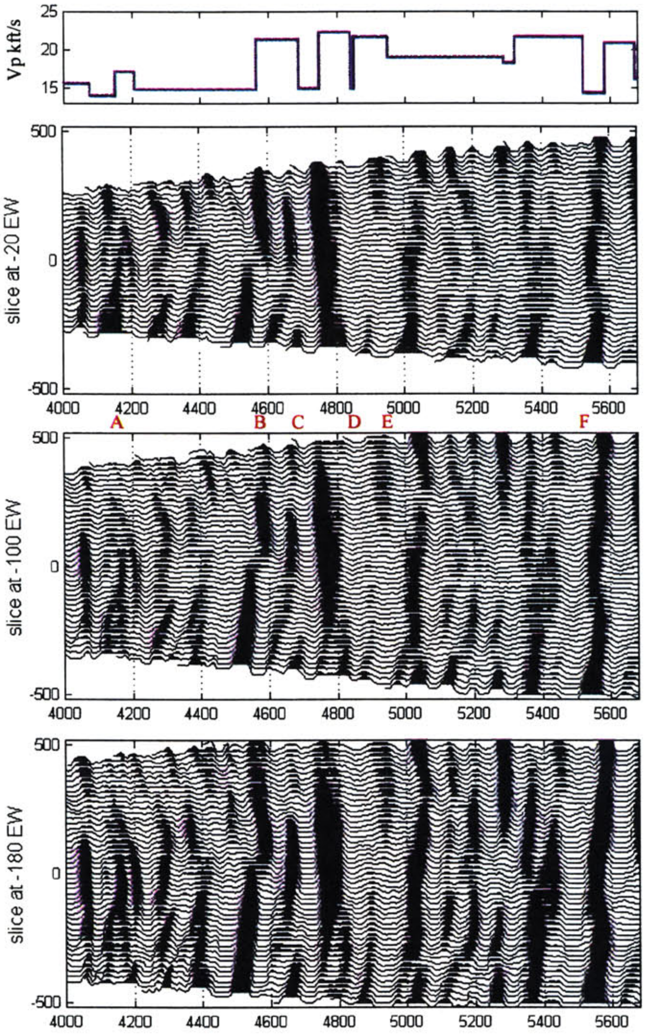

Figure 4-3: Medium aperture(15^o) conventional migration image with a flat layered velocity model.

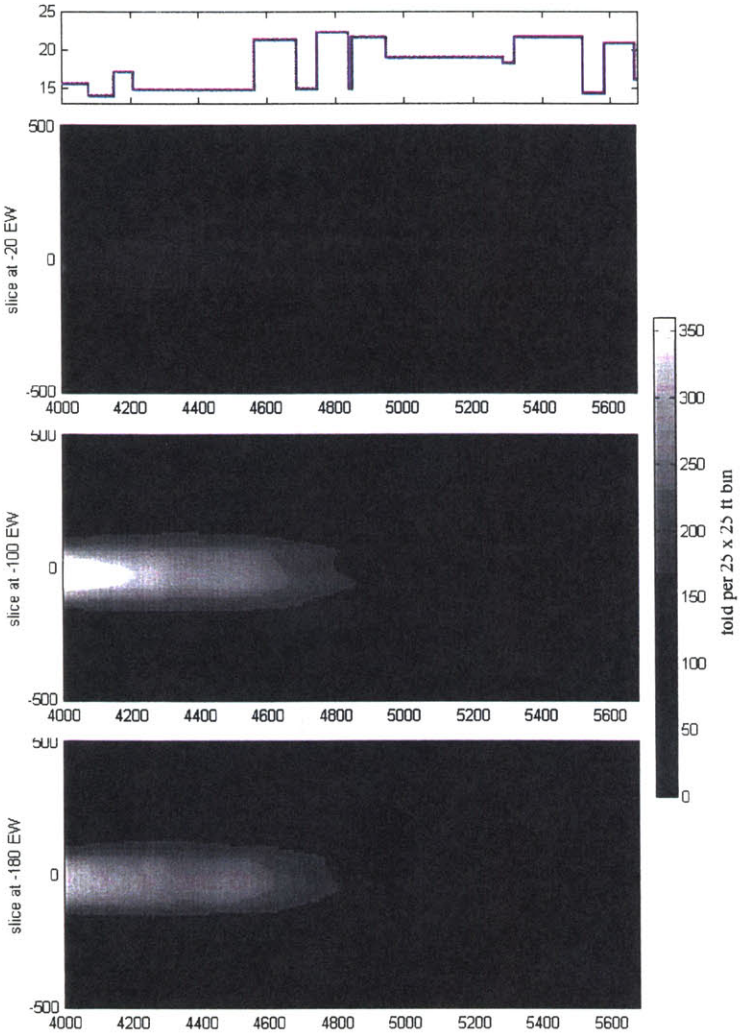

Figure 4-4: Fold map used for array illumination correction.

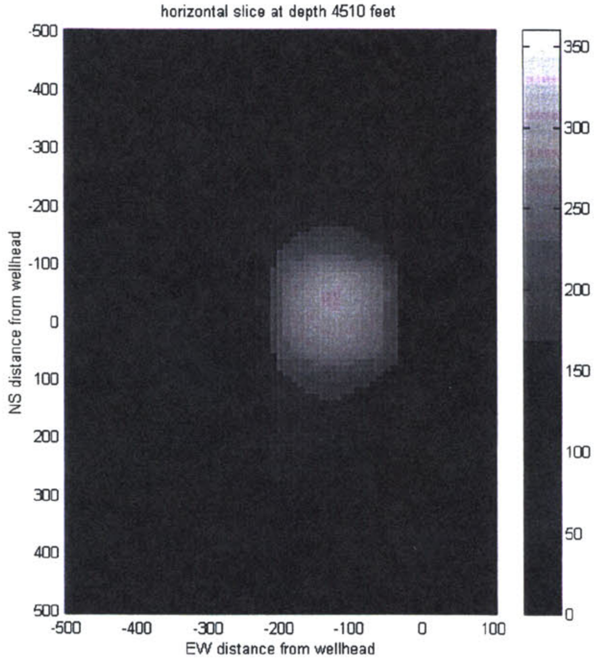

Figure 4-5: Horizontal slice through the fold map.

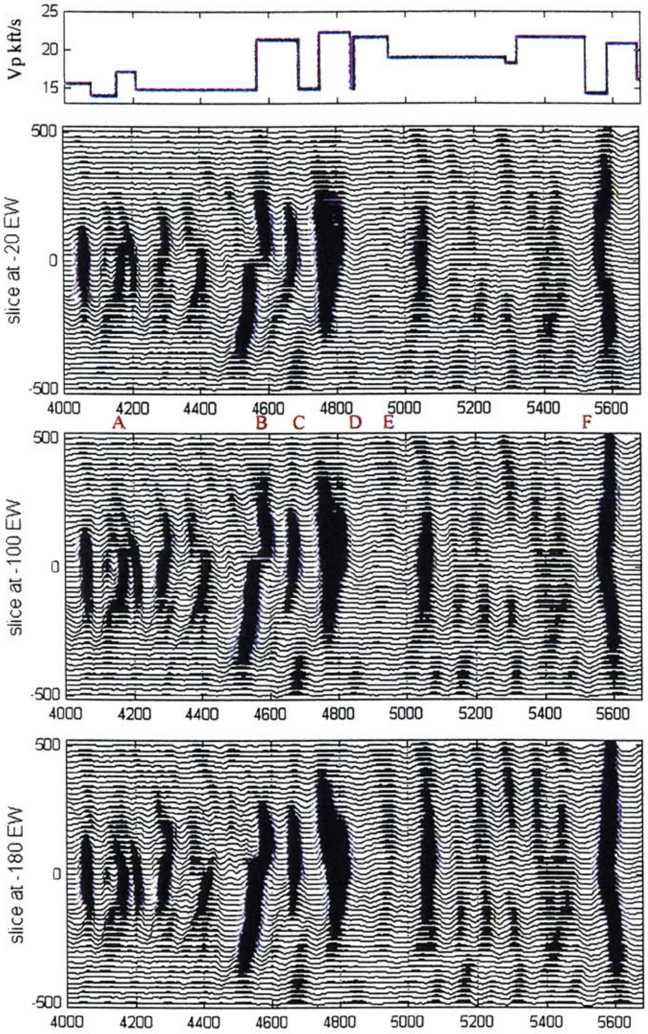

Figure 4-6: The image from Figure 4-3 without the fold correction.

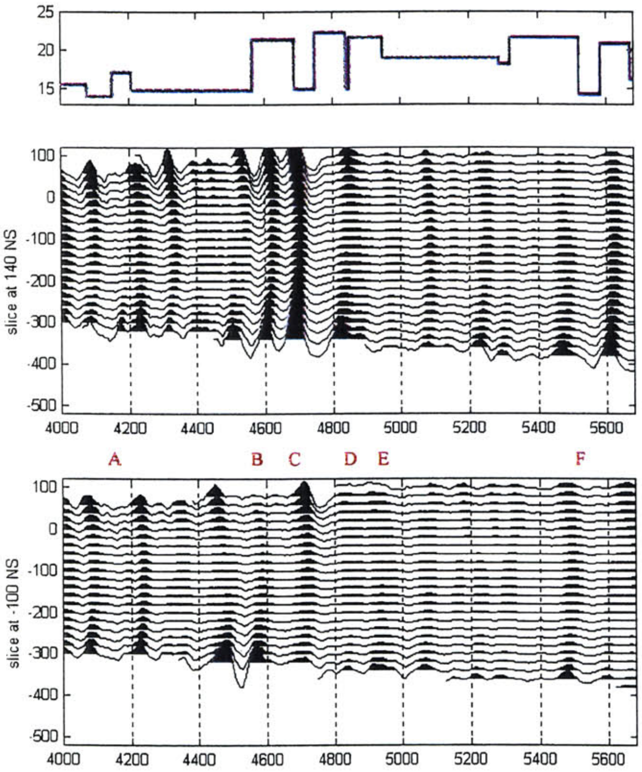

Figure 4-7: EW slices of the medium aperture image. Because the receiver array is very narrow in this direction, the image is narrow and poorly resolved.

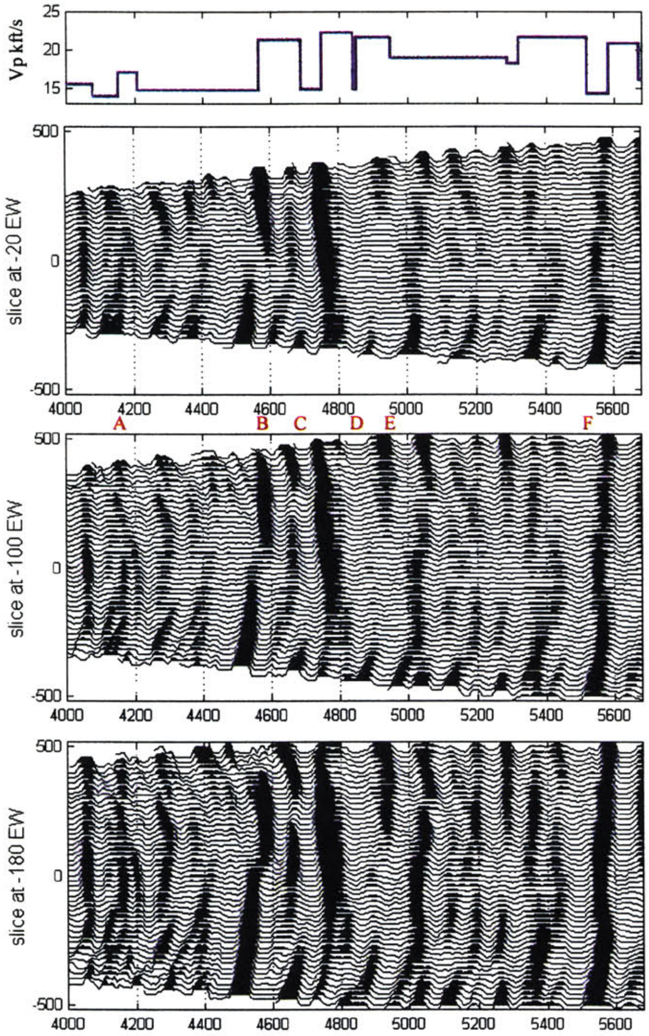

Figure 4-8: Wide aperture (30^o) conventional migration image with a flat layered velocity model.

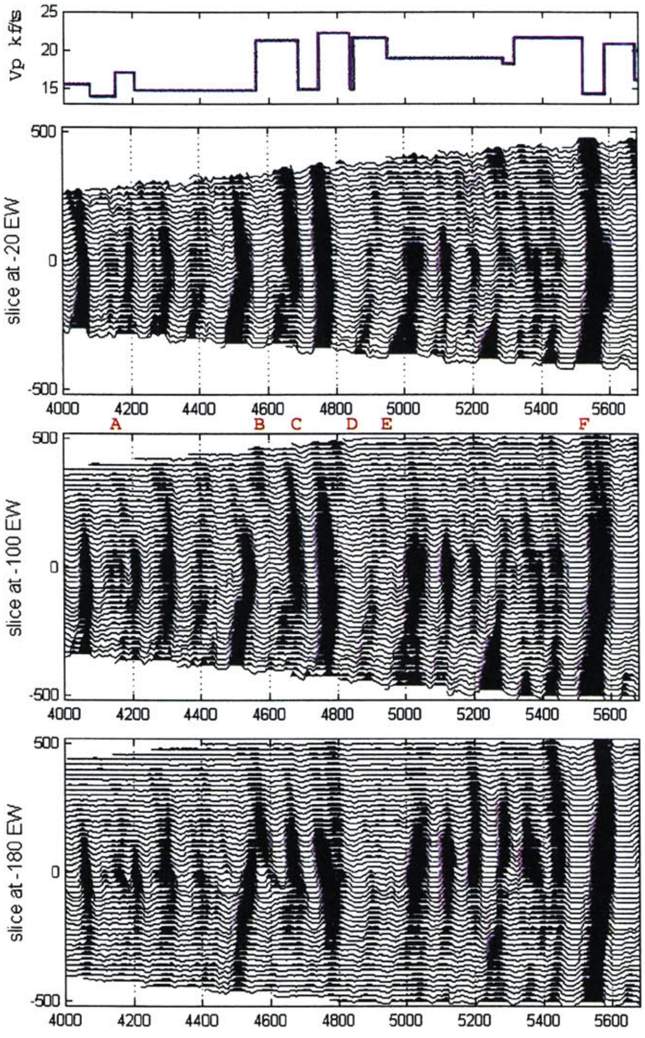

Figure 4-9: Narrow aperture (5^o) conventional migration image with a flat layered velocity model.

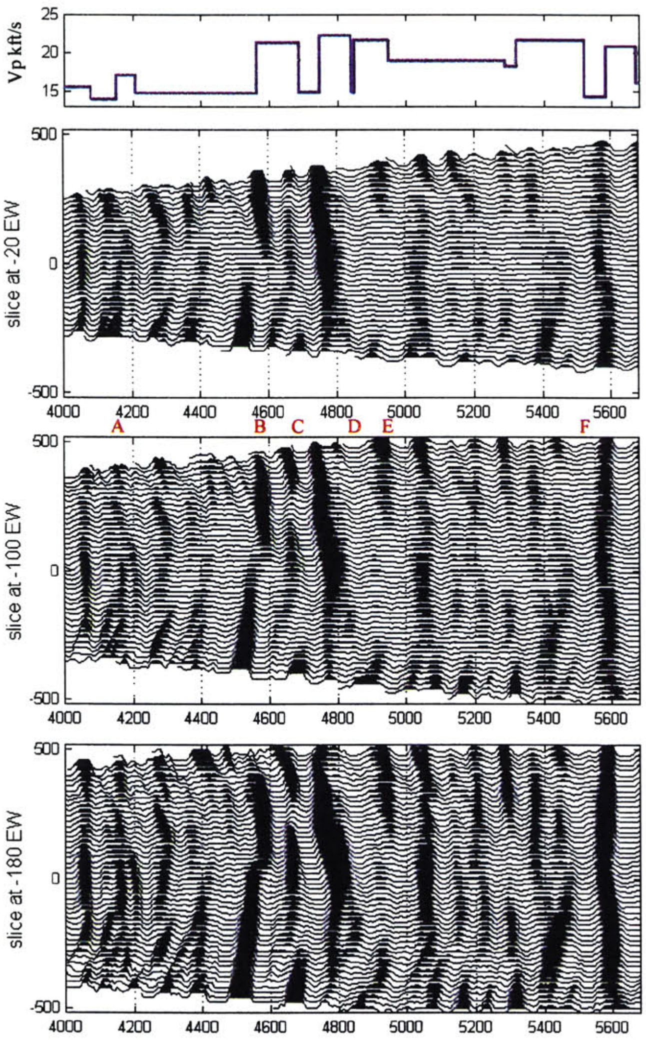

Figure 4-10: Wide aperture (30^o) conventional migration image with the 3D velocity model.

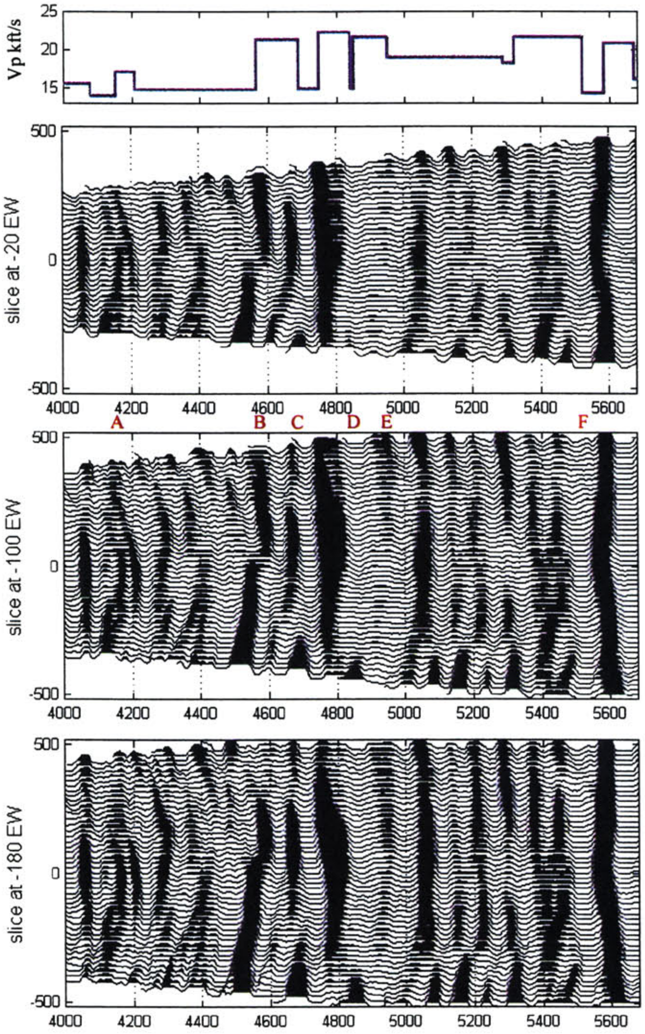

Figure 4-11: Medium aperture (15^o) conventional migration image with the 3D velocity model

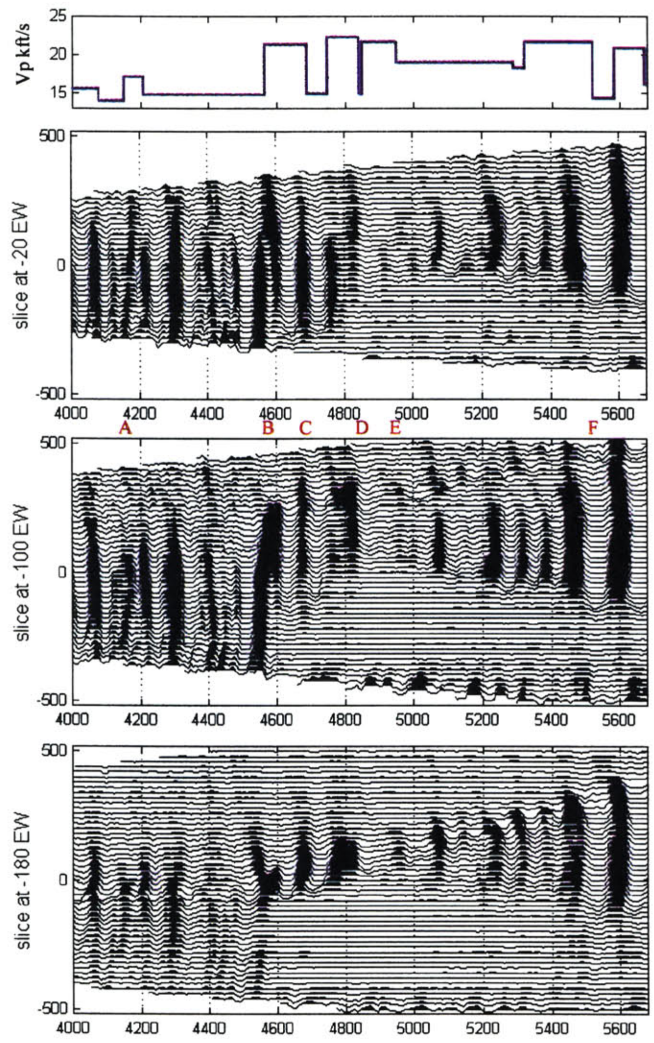

Figure 4-12: Narrow aperture (5^o) conventional migration image with the 3D velocity model.

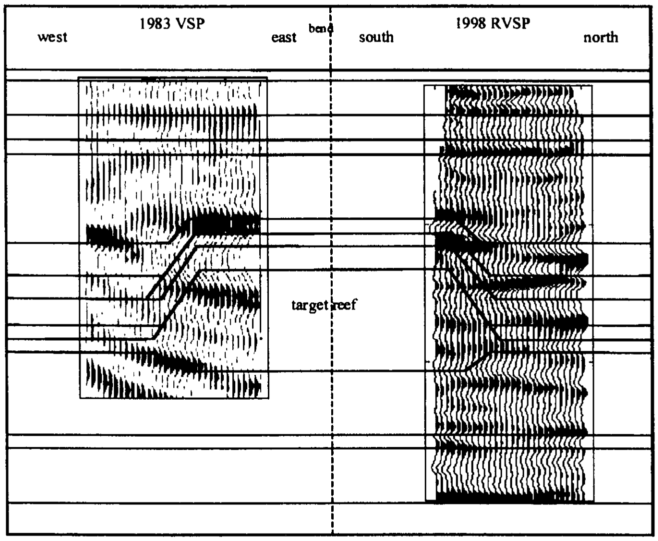

Figure 4-13: Comparison of the 1998 RVSP image with a VSP image from data collected in 1983.

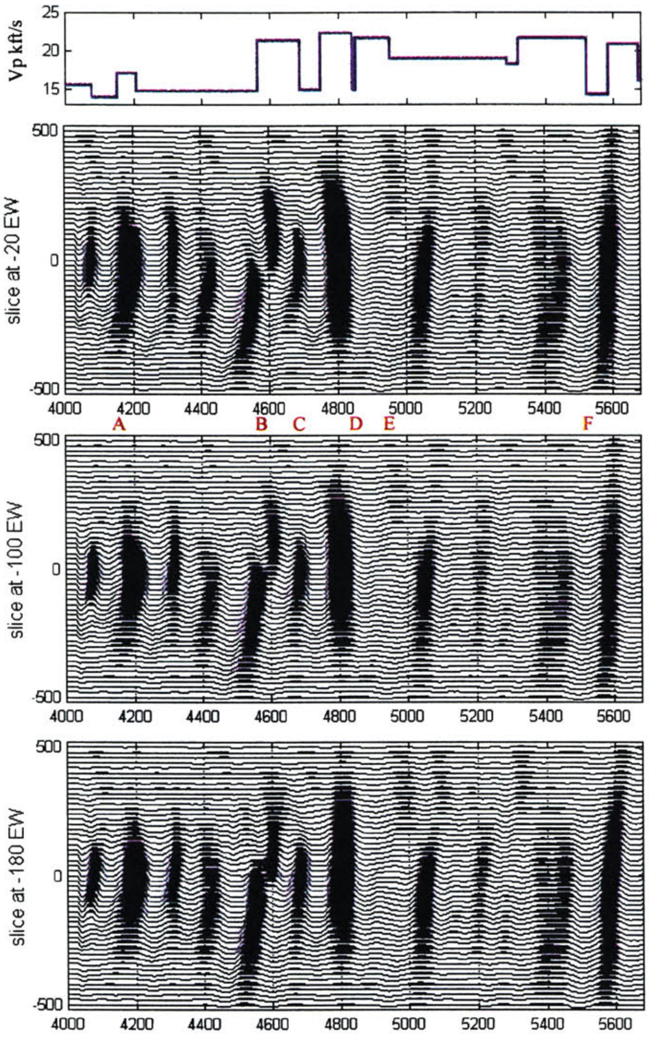

Figure 4-14: The VII image made with the flat layered velocity model, with no fold correction.

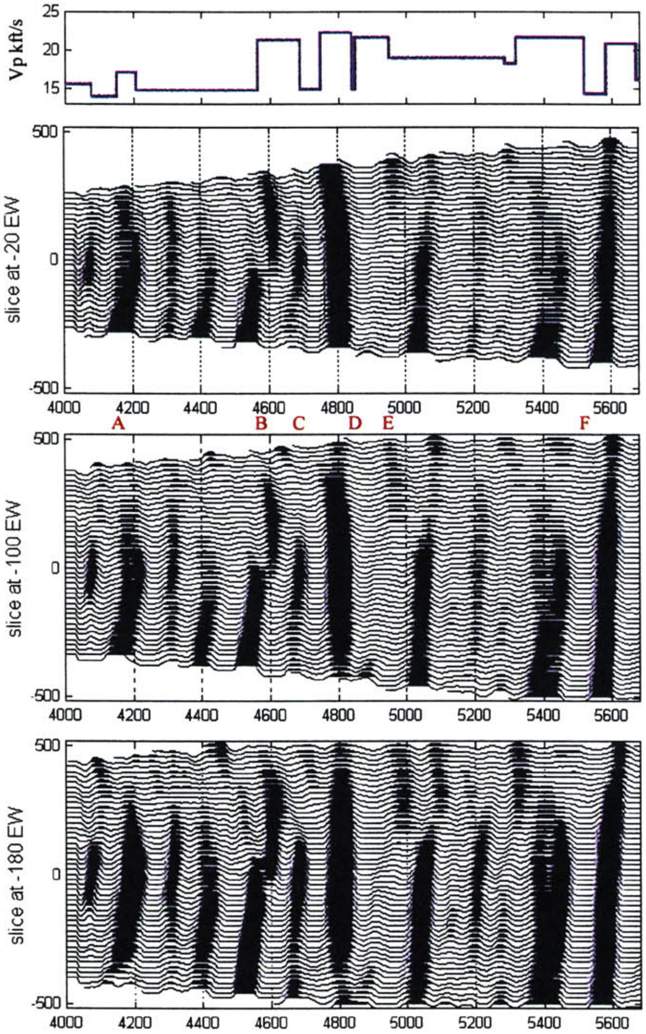

Figure 4-15: The VII image made with the flat layered velocity model, with the fold correction applied.

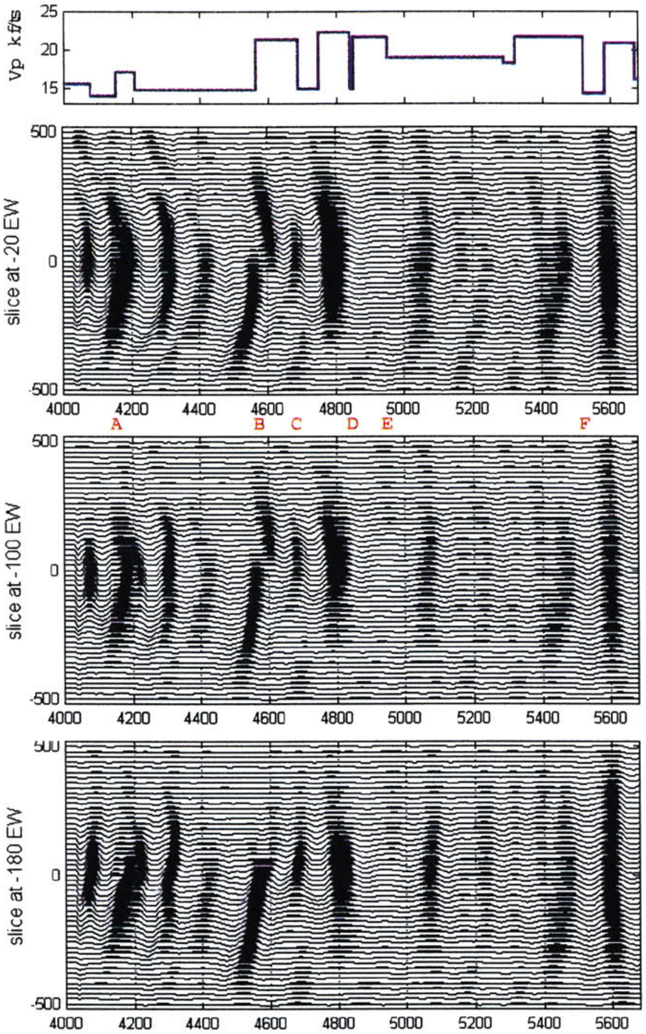

Figure 4-16: The VII image made with the 3D velocity model, without the fold correction.

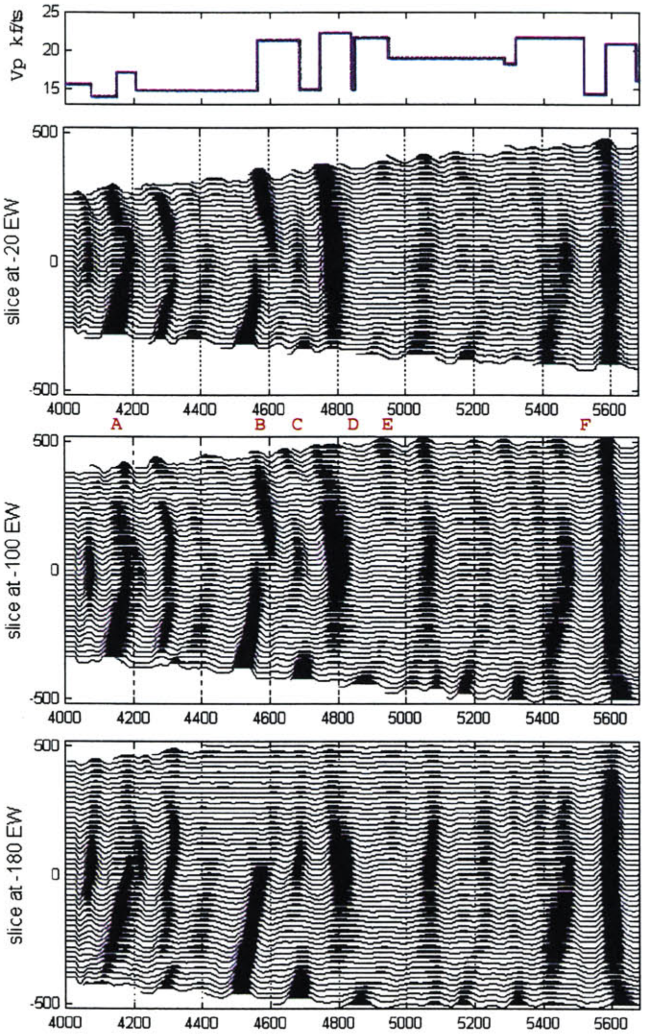

Figure 4-17: The VII image made with the 3D velocity model, with the fold correction applied.

Chapter 5

Conclusions and Future Work

5.1 Conclusions

This thesis presented a data processing and imaging scheme tailored to the needs of downhole seismic data. The scheme is applied to a 3D reverse vertical seismic profile (RVSP) dataset measured over a hydrocarbon bearing pinnacle reef in northern Michigan, a dataset which presented many challenges due to the survey geometry.

Reverse VSP geometry is itself fairly rare, RVSP in 3D with a random distribution of surface geophones is unprecedented. Therefore, there were no commercially available processing tools for this dataset, and new processing tools had to be developed and tested.

The data processing sequence presented in this thesis took advantage of the repeatibility of the new downhole source, handling the data in common-receiver gathers instead of the usual common-source gathers. In fact, the data was treated like several single offset VSPs during the processing sequence, and issues related to the 3D geometry did not need to be addressed until the final imaging step.

A short sequence of processing steps, including amplitude corrections, deconvolution, wavefield separation, and application of statics, followed by the GRT migration method of Miller et al. (1987), provided a high resolution image of a portion of the target reef at 4600 feet (1400 meters) depth. The high resolution of the image was largely due to the downhole source, which generated a high powered signal at frequencies up to several hundred Hertz.

However, the limited nature of the receiver array caused artifacts resembling migration smiles in the image. These artifacts were partially suppressed by limiting the dip aperture of the migration, but this also limited the reflector dips in the image.

To maximize the imaging capibilities of the data, a second approach complimenting the GRT method was developed. This approach, termed vector image isochron (VII) migration, produced images of lower resolution than the GRT images, but without the array artifacts. This allowed the artifacts to be identified, aiding interpretation of the GRT images.

The VII scheme is an extension of the GRT migration process of Miller et al. (1987), but involves forming an image which depends on the imaged plane orientation, transforming the image based on the array geometry, then finishing the GRT summation over plane orientations. Images made with VII migration show more continuity along reflectors than images made with the conventional method, without the loss of energy on dipping reflectors which results with conventional aperture limitation. VII images also show more even illumination than conventional images, although an effect similar to NMO stretching reduces the resolution of the VII image as compared to the GRT image.

When used as compliments of eachother, GRT and VII images provide 3D information about the subsurface structure which far surpass surface seismics in terms of resolution. These images are directly tied to depth, and are not limited to a slice as are crosswell studies. The combination of the new downhole source with the processing and imaging schemes in this thesis provide a valuable new tool for the task of reservoir modeling.

5.2 Future work

Regarding the field work in this thesis, plans are underway to return to the Michigan Test Site for a more extensive study which would include 3D surface seismics, VSPs, and a multiwell RVSP. The new study hopes to explain conclusively the high frequency content of the RVSP data by providing VSPs and RVSPs with identical (but reversed) geometries. Also, the image quality could be greatly improved by expanding the extent of the receiver array and reducing the surface noise by use of adaptive filtering and receiver station grouping.

The new imaging method currently has two obvious limitations. First, a constant velocity earth is assumed in the derivation of vector image isochrons, which causes inaccuracies in portions of the image grid which are the shallowest and furthest out from the shot locations in the wellbore, involving the most ray curvature. VII field data images of the shown in Chapter 4 of this thesis could be improved by deriving vector image isochrons which depend one additional parameter: a slope of velocity with depth.

Second, the transform of borehole seismic data assumes that the shot depth is fixed. This requires that the data be migrated and transformed one shot depth at a time, a time consuming process. In many cases a mean value of shot depth can be used to transform the entire image. This is a good approximation when the image grid is deeper than the shots, so there is not a large angular difference in the raypaths from the shot locations to any point in the grid.

An aspect of the imaging process which has not been tested is the sensitivity of the solution to the velocity model. The field data presented in this thesis was collected in a region where the earth model is well known, but usually the structure of the earth is not known. The imaging method should include steps for determining the migration velocity model, as well as testing the sensitivity of the image to the velocity model and making conclusive statements about the uncertainty of the solution. This is especially important for the imaging method in this thesis, as arrays with uneven illumination will have varying resolution in different portions of the subsurface.

There are practical aspects of the method which can also be improved on. Foremost, the expressions for vector image isochrons in borehole seismic vector images should be described explicitly instead of found numerically to speed up the tranformation process. This would make it practical to migrate and transform RVSP data one source location at a time.

If the method could be implemented by putting an appropriate weighting term into the GRT migration integral, this would avoid the informative but costly (in disk space) step of forming the vector image.

As always, the most useful thing to be done with the new method is to test it on as many datasets as possible, most desirably on datasets with limited array apertures. This includes VSPs, RVSPs, the edges of surface seismic studies, single well imaging schemes, and, if isochrons are derived for two vertical arrays, crosswell data.

Another interesting possibility is to image the shallow crust using earthquake data. The method in this thesis is tailored towards limited aperture arrays, random geometries, and deep source locations. It is the ideal method to be applied to displacements recorded by a spread of seismometers from clusters of earthquakes, forming a 3D image of the deep crust and shallow mantle.

Bibliography

H. Ahmed. Investigation of azimuthal anisotropy from offset VSP data - a case study. *First Break*, 8:449–457, 1990.

L. Aleotti, F. Poletto, F. Miranda, P. Corubolo, F. Abramo, and A. Craglietto. Seismic while-drilling technology: use and analysis of the drill-bit seismic source in a cross-hole survey. *Geophys. Prosp.*, 47:25–39, 1999.

F. Aminzadeh. A Recursive method for the separation of ungoing and downgoing waves of the vertical seismic profile. *Geophysics*, 51:2206–2218, 1986.

N. A. Anstey. *Resolution, bandwidth, and money*, page Session:G.3. Soc. Of Expl. Geophys., 1980.

A. H. Balch, M. W. Lee, J. J. Miller, and R. T. Ryder. The use of Vertical-Seismic-Profiles in seismic investigations of the Earth. *Geophysics*, 47:906–918, 1982.

D. C. Barton. The seismic method of mapping geologic structure. *Geophys. Prosp.*, 1:572–624, 1929.

W. B. Beydoun and M. Mendes. Elastic ray-born modeling and inversion. In *MIT-ERL Reservoir Delineation Consortium Report*, 1987.

V. Cerveny, I. A. Molotkov, and I. Psencik. *Ray Method in Seismology.* Universita Karlova, 1977.

W.F. Chang and G. A. McMechan. Reverse-time migration of offset vertical seismic profiling data using the excitation-time imaging condition. *Geophysics*, 51:67–84, 1986.

H. W. Chen and G.A. McMechan. 3D Prestack depth migration for salt and subsalt structures using reverse-VSP data. *J. Seis. Expl.*, 1:281–291, 1992.

S. T. Chen and E. A. Eriksen. *Direct logging of formation P and S-waves in cased holes using a multipole tool*, page Session:DEV1.6. Soc. Of Expl. Geophys., 1988.

Jon F. Claerbout. Toward a unified theory of reflector mapping. *Geophysics*, 36: 467–481, 1971.

P. B. Dillon. Vertical seismic profile migration using the Kirchoff integral. *Geophysics*, 53:786–799, 1988.

P. B. Dillon and R. C. Thomson. Offset source VSP surveys and their image reconstruction. *Geophysical Prospecting*, 32:790–811, 1984.

W. G. Dillon and T. W. Spencer. Improved interface detection for vertical seismic profile inversion. *Geophysics*, 53:1244–1247, 1988.

James P. Disiena, James E. Gaiser, and Dennis Corrigan. *Three-component vertical seismic profiles: Orientation of horizontal components for shear wave analysis*, page Session:S5.4. Soc. Of Expl. Geophys., 1981.

J. A. Dorr and D.F. Eschman. *Geology of Michigan.* The University of Michigan Press, Ann Arbor, MI, 1970.

C. Esmersoy. Inversion of P and SV waves from multicomponent offset vertical seismic profiles. *Geophysics*, 55:39–50, 1990.

E. I. Galperin. *Vertical Seismic Profiling.* Soc. Of Expl. Geophys., 1974.

J. Gazdag. Wave equation migration with the phase shift method. *Geophysics*, 43: 1342–1351, 1978.

T. Gut, W. Sollner, E. Luschen, and H. A. K. Edelmann. More reliable shear-wave data from VSPs using the CIPHER technique. *First Break*, 12:123–129, 1994.

J. Haldorsen, Miller D., and J. Walsh. Multichannel Wiener deconvolution of vertical seismic profiles. *Geophysics*, 59:1500–1511, 1994.

J. Haldorsen, Miller D., and J. Walsh. Walkaway VSP using drill noise as a source. *Geophysics*, 60:978–997, 1995.

B.A. Hardage. *Vertical Seismic Profiling, Part A: Principles.* Geophys. Press, 1985.

K. Hokstad, R. Mittet, and M. Landrø. Elastic reverse time migration of marine walkaway vertical seismic profiling data. *Geophysics*, 63:1685–1695, 1998.

P. Hubral and T. Krey. *Interval velocities from seismic reflection time measurements.* Society of Expl. Geophysicists, 1977.

P. J. Jackson, K.R. Onions, and A. R. Westerman. Use of inverted VSP to enhance the exploration value of boreholes. *First Break*, 6:233–246, 1989.

R. L. Jodry. Growth and dolomitization of Silurian reefs, St. Clair County, Michigan. *Bull. of the Amer. Assoc. of Petr. Geol.*, 53:957–981, 1969.

S. E. Johnstad and H. Ahmed. Applications of the VSP technique in the central area of the Oseberg Field. *First Break*, 9:361–373, 1991.

R. N. Jolly. Deep-hole geophone study in Garvin County Oklahoma. *Geophysics*, 18: 662–670, 1953.

T.H. Keho and W.B. Beydoun. Paraxial ray Kirchhoff migration. *Geophysics*, 60: 1540–1546, 1989.

P. Kennett, R. L. Ireson, and P.J. Conn. Vertical Seismic Profiles: their application in exploration geophyics. *Geophysical Prospecting*, 28:676–669, 1980.

M. Knecht and H. A. K. Edelmann. Processing shear-wave VSP data. *Geophys. Prosp.*, 35:955–972, 1987.

F. K. Levin and R. D. Lynn. Deep-hole geophone studies. *Geophysics*, 23:639–664, 1958.

L. R. Lines, A. Bourgeois, and J. D. Covey. Traveltime inversion of offset vertical seismic profiles - a feasibility study. *Geophysics*, 49:250–264, 1984.

R. D. Lynn. A low-frequency geophone for borehole use. *Geophysics*, 28:14–19, 1963.

Burton McCollum and Wilton W. Larue. *Utilization of existing wells in seismograph work*, volume 01, pages 119–128. Soc. Of Expl. Geophys., 1947.

M. A. Meadows and D. F. Winterstein. Seismic detection of a hyraulic frature from shear-wave VSP data at Lost Hills Field, California. *Geophysics*, 59:11–26, 1994.

K. J. Mesolella, J.D. Robinson, and A. R. Ormiston. Cyclic deposition of Silurian carbonates and evaporites in Michigan Basin. *AAPG Bulletin*, 58:34–62, 1974.

D. Miller, M. Oristaglio, and G. Beylkin. A new slant on seismic imaging: Migration and integral geometry. *Geophysics*, 52:943–964, 1987.

W. M. Moon, A. Carswell, R. Tang, and C. Dilliston. Radon transform wave field separation for vertical seismic profiling data. *Geophysics*, 51:940–947, 1986.

G. Omnes, C. Wu, and F. Baixas. Vertical Seismic Profiling; 3-D seismic reflection survey. Technical report, Compagnie Generale de Geophysique, 1984.

Gildas Omnes. Exploring with SH-waves. *J. Can. Soc. Expl. Geophys.*, 14(01):40–49, 1978.

B. N. P. Paulsson, J. W. Fairborn, and B. N. Fuller. Imaging of thin beds using advanced borehole seismology. *The Leading Edge*, 17:947–953, 1998.

M. A. Payne, E.A Eriksen, and T. D. Rape. Consideration for high-resolution VSP imaging. *The Leading Edge*, 13:173–180, 1994.

S. A. Reeckmann and G.M. Friedmann. *Exploration for carbonate petroleum reservoirs.* John Wiley & Sons, New York, NY, 1982.

E. D. Riggs. Seismic wave types in a borehole. *Geophysics*, 20:53–67, 1955.

G. D. Sharma. Geology of Peters Reef, St. Clair County, Michigan. *Bulletin of the Am. Assoc. of Petr. Geol.*, 50:327–350, 1966.

J. M. Smidt. VSP processing with full downgoing-wavefield deconvolution applied to the total wavefield. *First Break*, 7:247–257, 1989.

T. W. Spencer, G. A. Smith, and W. H. Cho. Vertical seismic profile polarization method for determining reflector orientation. *Geophysics*, 53:1169–1174, 1988.

R. H. Stolt. Migration by Fourier transform. *Geophysics*, 43:23–48, 1978.

R. Sun and G. A. McMechan. Nonlinear reverse-time inversion of elastic offset vertical seismic profile data. *Geophysics*, 53:1295–1302, 1988.

M. Suprajitno and S. A. Greenhalgh. Separation of upgoing and downgoing waves in vertical seismic profiling by contour-slice filtering. *Geophysics*, 50:950–962, 1985.

R. Turpening. need report title. Technical report, Massachusetts Institute of Technology, 1995.

R. Turpening and B. Paulsson. Proposal: Comprehensive test of the new downhole, hydraulic, axial vibrator. Technical report, Earth Resources Laboratory, Massachusetts Institute of Technology, 1996.

R. van der Pal, M. Bacon, and D. Pronk. 3D walkaway VSP, enhancing the seismic resolution for development optimization of the Brent field. *First Break*, 14:463–469, 1996.

J. W. Wiggins, P. Ng, and A. Manzur. The relationship between the VSP-CDP transformation and VSP migration. In *56th Annual SEG meeting, New Orleans, USA, Expanded Abstracts*, pages 565–568, 1986.

K. D. Wyatt and S. B. Wyatt. The determination of subsurface structure information using a vertical seismic profile. In *51st Ann. Internat. Mtg., Soc. Expl. Geophys., Expanded Abstracts*, pages 1915–1949, 1981.

Ozdogan Yilmaz. *Seismic data processing.* Soc. Of Expl. Geophys., 1988.

Changxi Zhou and Gerard T. Schuster. *Quasi-random migration of 3-D field data*, pages 1145–1148. Soc. Of Expl. Geophys., 1995.

L. J. Zimmerman and S. T. Chen. Comparison of vertical seismic profiling techniques. *Geophysics*, 58:134–140, 1993.

Appendix A

The MIT Michigan Test Site

A.1 Overview

A.1.1 The Michigan Basin

The Michigan basin is an intracratonic structural basin which has existed for at least 500 million years; it was an inland sea during the Upper Silurian Period, lined by barrier and pinnacle reefs (Dorr and Eschman, 1970). The basin's two main areas of production, northern and southern Michigan, are shown on Figure A-1 (Mesolella et al., 1974). The western and eastern portions of the basin lie under Lake Michigan and Lake Huron, and have not been developed because of environmental concerns.

In general, the barrier reef is barren and salt-plugged. Hydrocarbon production is from the pinnacle reefs, which contain mostly water near the barrier reef, changing to mostly gas towards the basin interior (Reeckmann and Friedmann, 1982). The oil-bearing pinnacle reefs lie in the middle of this range, as does the test site where the data used in this thesis was aquired, as shown in Figure A-2.

Figure A-3 illustrates the general lithological sequence of the basin edge. There are three main areas: non reef, barrier reef, and pinnacle reef. The pinnacle reefs are encased in the Salina group, which consists of interbedded carbonates and evaporites. The source rock is most likely deeper shales, such as the Cincinnatian and the Utica shales. The reservoir rocks are coral reef structures which have been dolomitized and leached.

A.1.2 Exploration history

The pinnacle reefs in the southern Michigan trend have been productive since before seismic exploration was widely used. Geologists surmised that the northern edge of the basin would contain similar reef structures, which led to wildcat drilling and early discoveries in northern Michigan. Geophysical methods were first used to remotely map reef locations in the 1960s, and lead to an improved ratio of successful drilling.

As discussed and illustrated in Section A.3.2, the primary use of seismic data in Michigan has been to locate reefs. The low frequency content of seismic data and the detrimental effects of an extensive and variable layer of glacial till has made it nearly impossible to determine anything about a reef's internal structure from surface seismic data. This is unfortunate, since reservoir management techniques cannot be applied without detailed knowledge of the reservoirs and how they change over time.

The high resolution of the RVSP data presented in this thesis, with frequencies three times previous surface seismics and twice previous VSP studies, allows the internal structure of the reefs to be seen. For this reason, questions about the reef's structure which were previously unanswerable are now important, and the geological history of the reef can now be reconsidered with more focus on detail. Such details are quite important: such as whether thin salt layers extend into the reef. If they do, they could be trapping pockets of hydrocarbons.

The geological history discussed in the following section is largely based on data from the southern Michigan reef trend. Details of how the northern reef trend differs from the southern trend are discussed at the end of Section A.2.

A.2 The geology of the pinnacle reefs

A.2.1 General geologic evidence

The observed structure suggests that the pinnacle reefs of the Michigan basin grew in a subtropical, humid climate. The alternating layers of carbonate and evaporite surrounding the reef are best explained by fluctuations in the depth of the inland sea covering the reefs. Periodically, lowering of sea level increased water salinity; during these periods reef growth stopped and evaporites were deposited.

Early models of the Michigan reef structure hypothesized that the pinnacle reefs were fully grown during Niagaran times, standing hundreds of feet above the ocean floor as the Silurian carbonates and evaporites were deposited. However, there is strong paleontological evidence of at least two separate phases of reef growth (Mesolella et al., 1974). Other evidence, such as the properties of the carbonate layers and the dolomitization patterns of the reef and carbonate groups, suggests that the reefs developed in a relatively shallow sea, standing just feet or a few 10s feet above the ocean floor. Reef growth would then have been simultaneous to carbonate mud deposition (Jodry, 1969).

Most Michigan pinnacle reefs, and the carbonates immediately surrounding the reefs, show a high degree of dolomitization (Sharma, 1966), (Jodry, 1969). The process of dolomitization, which requires a flow of magnesium rich water through the rock, has been important in developing porosity in most of the productive reefs. Both the reef and the surrounding carbonates were dolomitized, although the carbonates, lacking the solid framework of the reef structure, lost porosity during subsequent compaction.

The dip of the layers on the flanks of the reef can be accounted for entirely by 60% compaction of the carbonate mud surrounding the reef structure and the reef material's resistance to compaction (Jodry, 1969). In fact, such compaction may explain patterns of dolomitization in the reefs. Compaction would require the removal of water from the Niagaran group beneath the reef, but the water would not have been able to pass through the A1 evaporite. Water drainage through the reefs would have prevented the more saline Salinan water from entering the reef structure, and provided the magnesium for dolomitization of the reef (Jodry, 1969). This is illustrated in the first plot of Figure A-4.

A.2.2 The depositional history

There have been several proposed models of pinnacle reef formation, which are discussed in Mesolella et al. (1974). The model which seems to best fit observations begins during the period of Niagaran deposition, when the basin was characterized by open circulation and normal marine salinites (Mesolella et al., 1974). A belt of pinnacle reefs began to grow basinward of the barrier reef complex, standing tens of feet above the interreef areas.

Deposition of the Niagaran carbonate stopped during a relative lowering of sea level. The seawater increased in salinity and the A1 anhydrite was deposited as essentially flat-lying beds, shown in Figure A-4A.

The next era of reef development, which involves the portion of the reef which has been hydrocarbon-bearing, is shown in the Figure A-4B. Reef growth resumed when the sea deepened and salinity decreased, and the A1 carbonate was deposited as fairly flat layers in the interreef areas.

Figure A-4 does not illustrate the one possible structural detail which has been seen in well logs on the flanks of some reefs: the A1 evaporite may extend into the reef, separating the two portions of reef growth. This is important to reservoir development, as a layer of anhydrite in the reef would affect fluid flow within the reef as well as from the deeper source rocks to the reservoir rock.

The reef likely died during A1 carbonate deposition, Figure A-4C, possibly because it could not grow fast enough to stay above the carbonate mud, so that the reef top is buried in the A1 carbonate. During the next period of low sea level and high salinity the A2 Salt was deposited, followed by the A2 anhydrite. These layers were thicker than the A1 anhydrite and completely covered the reef structures.

After A2 carbonate deposition, Figure A-4D, the sea apparently entered another era of high salinity in which the B Salt was deposited over both the pinnacle reefs and non reef areas. The thick B Salt serves as a stratigraphic trap and provides a velocity contrast with the A2 carbonate which has been widely used to locate the pinnacle reefs.

A.3 Previous MIT studies

A.3.1 The Test site

The MIT test site is located in Manistee county, in the southwest portion of the northern Michigan reef trend near Lake Michigan (see Figure A-2). The target is a pinnacle reef at 4600-5000 feet which is under production by Shell. It has produced about 800,000 barrels of oil since 1978.

The layout of the test site is shown in Figure A-5. MIT owns three well; the Burch well is just to the west of the reef, the Stech well is to the east of the reef, and the third well to the south of the reef has been plugged. The Stech well is relatively new, being drilled, cased and cemented in 1990-1991. The productive Shell well is shown in the center of the reef.

Several studies of the reef have been done by MIT, including 2D and 3D seismics, several 2D VSPs, reverse VSPs, crosswell tomography, crosswell reflection imaging, and a full suite of well logs. Hence there is a store of knowledge on which to build.

A.3.2 Surface seismics

Early seismic studies in Michigan used the method of detecting pinnacle reefs illustrated in Figure A-6. The pinch-out of the A2 salt casues a change in the shape of the B Salt reflected wavelet over the reefs. This method was applied to a 3D surface shoot in 1983 to map the reef's location. Figure A-7 shows a slice of that 3D data set with the change in the wavelet shape marked. The reef outline determined by manually mapping the wavelet shape for all traces in the 3D dataset is shown in Figure A-8.

This map should is considered an estimate of the reef shape. For instance, we know from well logs that the western edge of the reef does not extend to the Burch well. But this map is the best estimate of the reef's location and shape which has yet been made in 3D, and agrees with the result in this thesis where the datasets overlap.

A.3.3 Other studies

Several VSPs shot in 1983 contain higher frequencies than the 1983 surface seismic, and show the A2 carbonate stepping up on the side of the reef. Figure A-9 is a CDP mapped VSP, shot at the surface point marked on Figure A-8 and receivers in the Burch well. The western edge of the reef is visible as a wedge at .73 seconds. The VSP data had a central frequency of 50 Hertz, with maximum signal frequencies up to 100 Hertz. This allows 1-2 wavelengths over the entire reef depth, so although the shape of the A2 reflector can be seen, this data still cannot resolve the reef's internal structure (Omnes et al., 1984).

The high frequency content of crosswell studies done in 1983 allowed the structure within the reef to be seen. Figure A-10 shows crosswell reflection imaging results with data collected using a piezoelectric source with frequencies in the 1.5 kHz range. The geological bottom of the reef is the bottom of the brown Niagaran at 5000 feet; this velocity contrast is too small to be seen in most surface seismic data. The producing zone is in the brown Niagaran at about 4700 feet.

Figure A-11 is a cartoon drawing of the reef structure developed from the VSPs and crosswell surveys. The MIT Burch and Stech wells shown to the east and west of the reef. The details of the layer pinch-outs are best guesses based on the geological model of the reef and well log data from this and other reefs. No wells are located the "layer pinch-out" region of this reef, and there has not yet been seismic data which illuminates this area with sufficient resolution to map the layer pinch-outs.

A.4 The 1998 Research Program

A.4.1 Motivation

Funded by the MIT Reservoir Delineation Consortium, the initial impetus for this study was to conduct a field test of the new Paulsson downhole source, providing a comparison of this source with other downhole sources previously used at the test site.

Another goal was to test the feasibility of using randomly located arrays: to define field methods necessary for the deployment of such arrays and to develop algorithms for the processing and imaging of random 3D RVSP and surface seismic data.

A.4.2 Field hardware

The receiver array was a System One surface recording system provided to ERL by the Input/Output Corporation. The maximum channel capacity of the system is about

3,500 channels, but only 2,000 were used to allow a sample rate of 1 millisecond. Because a low velocity glacial till layer overlies high velocity rocks in Michigan, all ray paths are vertical or near-vertical at the surface. For this reason, only vertical receivers were used (Turpening and Paulsson, 1996).

The 1998 survey included a 3D surface seismic using the same random receiver spread as was used in the RVSP. Because of battery failures in the receiver spread, the 3D surface seismic fold was too low and irregular to produce useful results, so will not be referred to in this thesis.

The RVSP study had two unique features which puts it on the leading edge of single well imaging efforts: the new downhole source developed by Paulsson Geophysical, (Paulsson et al., 1998), and the reverse VSP geometry in 3 dimensions.

A.4.3 The Paulsson downhole source

The industry has long been in need a strong, broadband source that is capable of both cross-well and RVSP usage in borehole environments. The Paulsson source, developed through a Cooperative Research and Development Agreement (CRADA) between Chevron, Sandi, Exxon, Gas Research Institute, E-Systems, Pelton CO., Conoco, and Amoco fills this need (Turpening and Paulsson, 1996).

The Paulsson source is a hydraulic axial vibrator. It has a 4.4" outside diameter, and is deployed with special heavy duty wireline and fiberoptic power and data cables. It clamps into the borehole and is best used in cased wells, but with some care can be deployed in uncased wells. It can be used in deep wells, being rated to over 200^o Celcius and 12,000 psi external pressure (Paulsson et al., 1998).

Figure A-12 shows the output of the tool. The dashed yellow curve is an older prototype tool and the solid blue curve is the output of the tool in a laboratory test. In the peak output range from 100 - 200 Hz, the force approaches 8000 lbs. The peak at 500 Hertz was caused by resonance in the laboratory equipment.

The 1998 Michigan RVSP was the first fully successful use of the P/GSI source in the field. This thesis shows that the source provided a high power, high frequency repeatable signature.

A.4.4 The random array

It is difficult to draw a conclusion about the effectiveness of the random receiver array on the image resolution from the 1998 Michigan RVSP data because of the non-ideal shape of the receiver array, but it is has been found that the random geometry is no hindrance to the processing sequence or the fieldwork.

Other studies have indicated that random arrays can achieve better results with the same number of sources and receivers as regular arrays, or the same results with fewer. For example, Figure A-13 shows images from Zhou and Schuster (1995), obtained by taking 1/4 subsamplings of a 3D data set. Plot A subsampled on a regular grid (RM), plot B used a quasi-random sampling (QM). Zhou and Schuster (1995) concludes that QM migration could be 5 times more efficient than RM because "the incoherent arrangement of sources and receivers leads to cancellation of grating lobes or aliasing artifacts." In effect, "QM migration has a built in anti-aliasing filter."

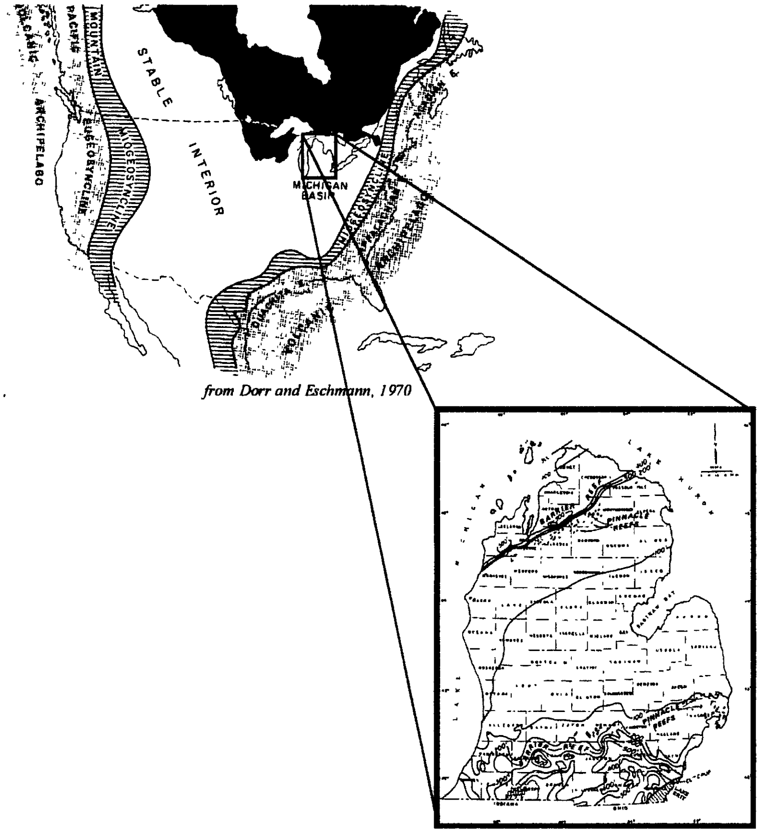

from Dorr and Eschmann, 1970

from Mesolella, et al., 1974

Figure A-1: The Michigan Basin.

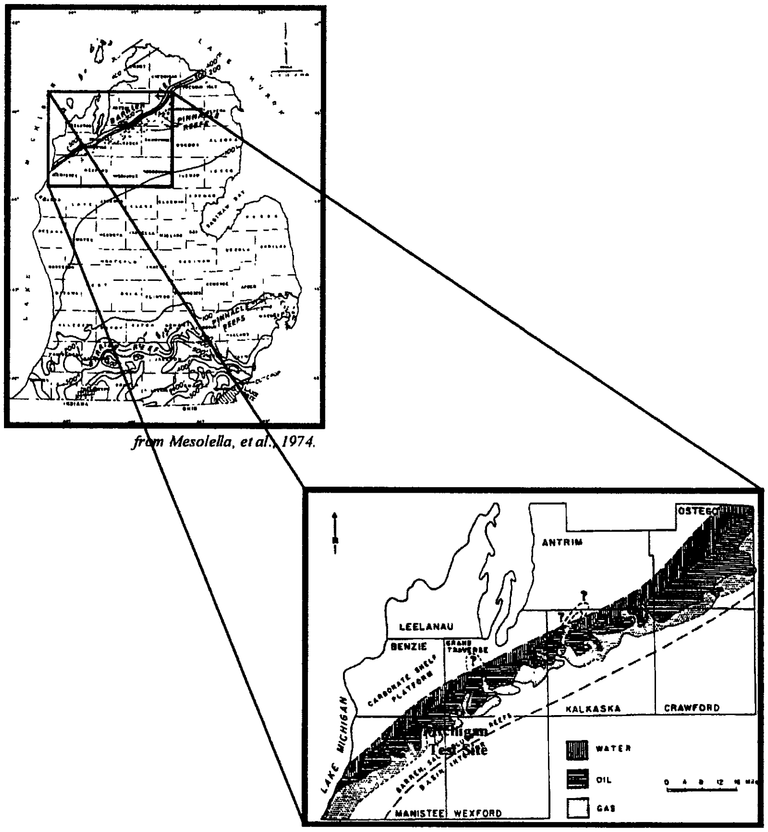

from Mesolella, et al., 1974.

from Reeckmann, et al., 1982

Figure A-2: The northern Michigan reef trend, and location of oil, water, and gas filled reefs within the trend.

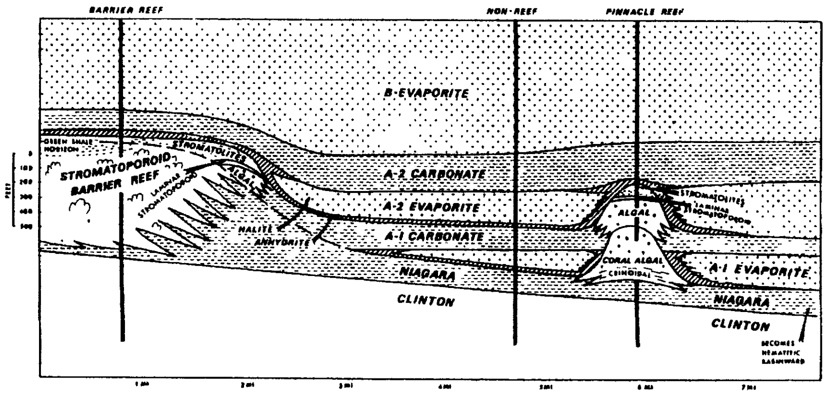

Figure A-3: Generalized cross-section of the barrier-pinnacle reef lithological sequences. From Mesolella et al. (1974).

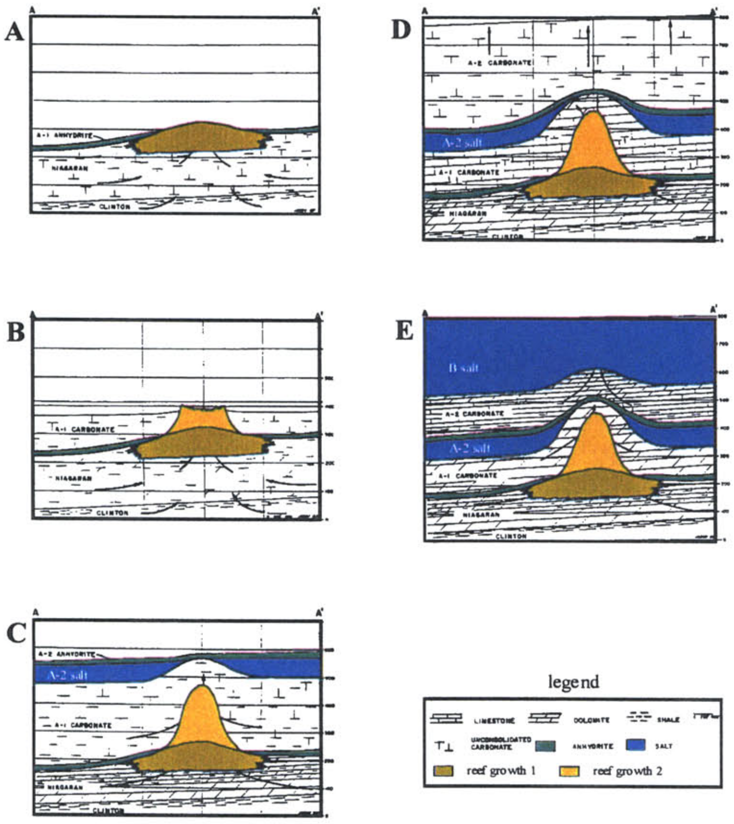

Figure A-4: The various stages of pinnacle reef growth and the deposition and compaction of the surrounded Salina rock groups. Black arrows indicate patterns of water flow during compaction of the groups surrounding the reef. (Figures from Jodry (1969).)

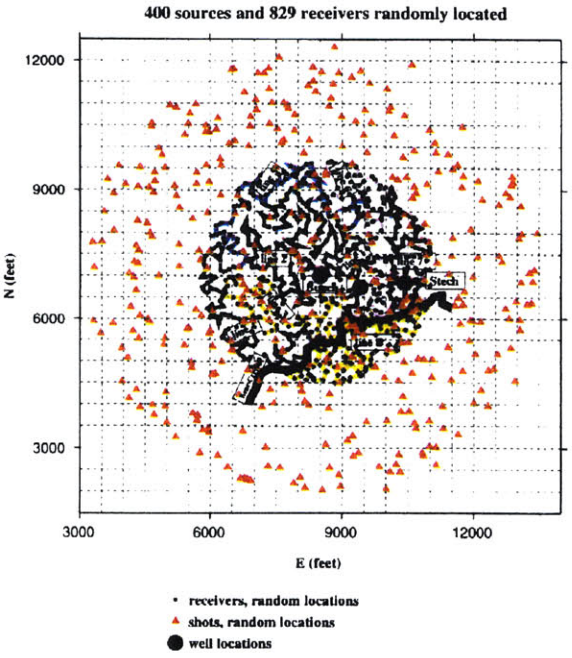

Figure A-5: The layout of the MIT Test Site.

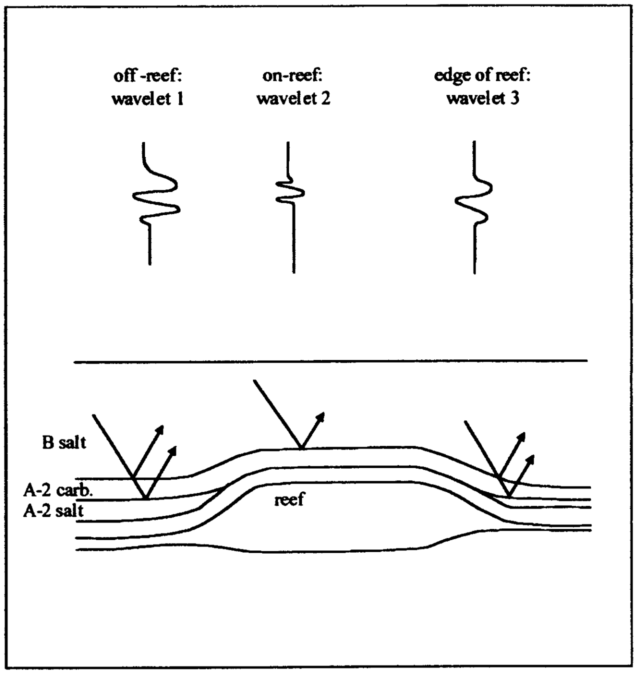

Figure A-6: Modeled reflection response for 40 Hertz wavelet. (needs to be redone because the top guy has to be from top of B salt.)

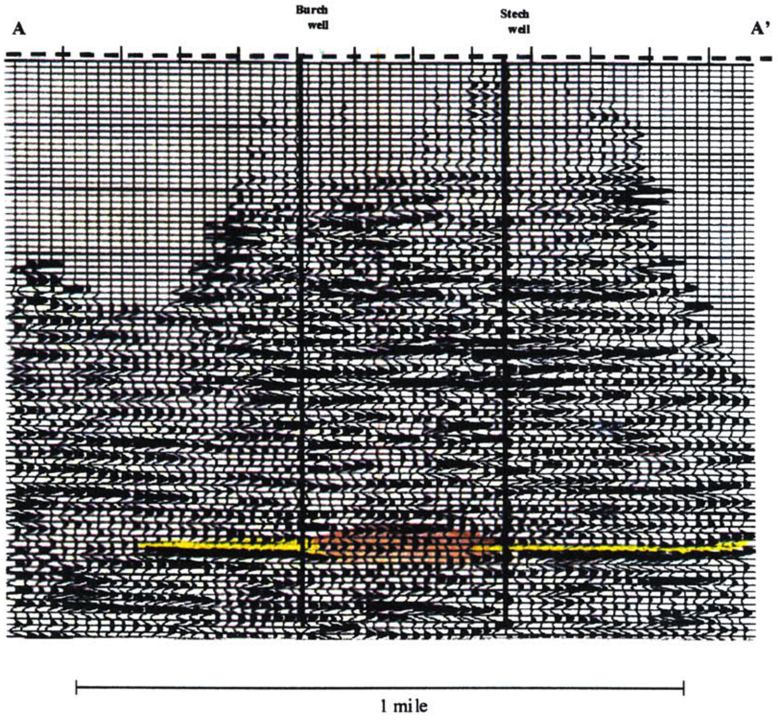

Figure A-7: A slice of the 3D dataset shot in 1983. The wavelet changes shape where the A1 layers pinch out over the reef.

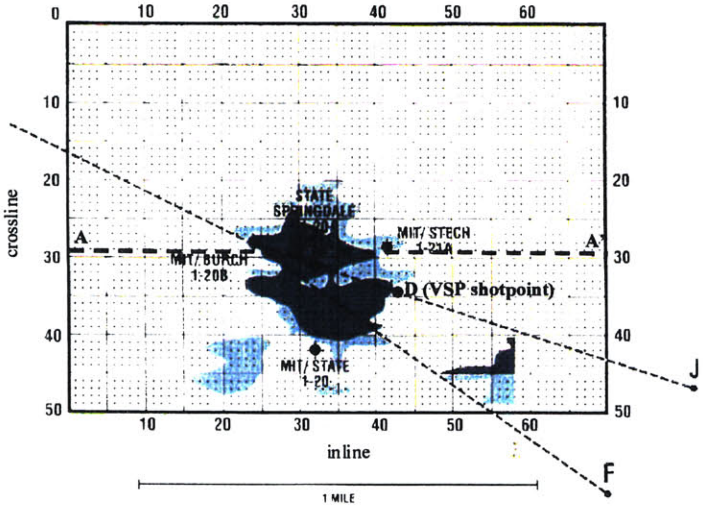

Figure A-8: Reef shape deduced from the change in the shape of the wavelet from of the B salt - A2 carbonate reflection. Dark green shows on reef (wavelet 2), light green is edge of reef (wavelet 3). Figure A-7 was at crossline 29, shown as A-A'.

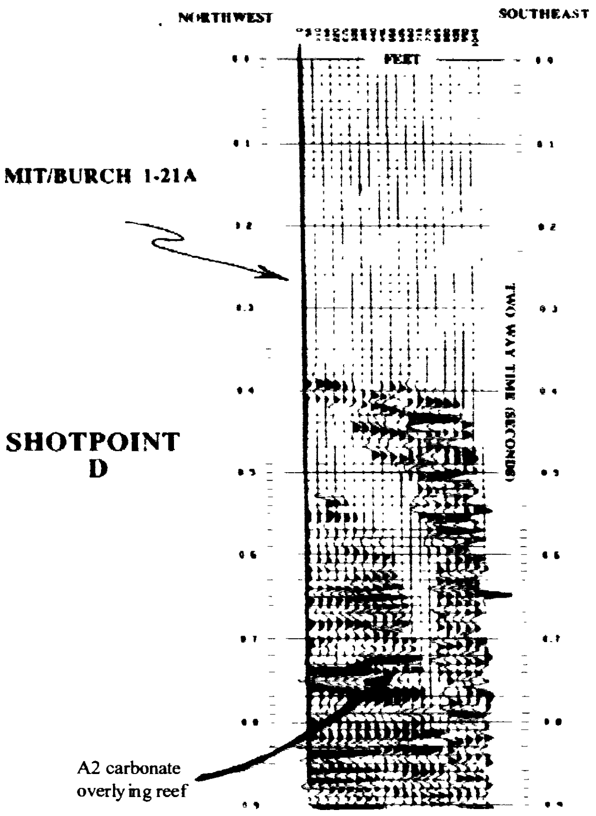

Figure A-9: Imaged generated with VSP data shot in 1983.

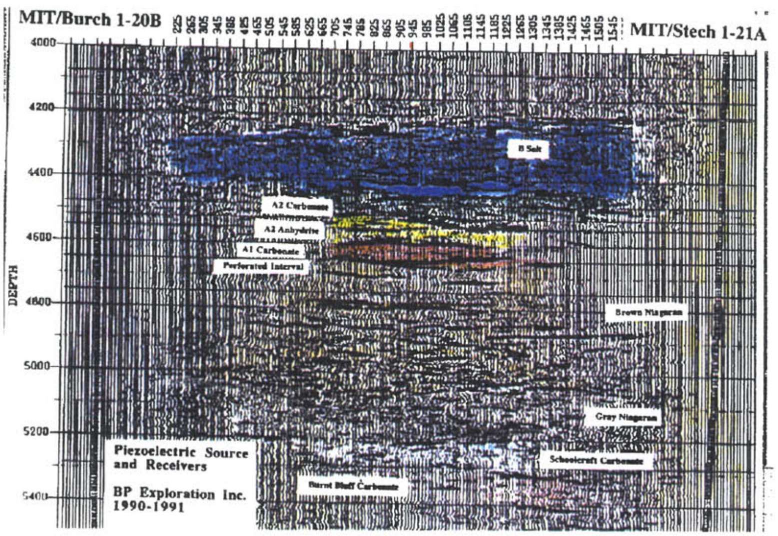

Figure A-10: Result of crosswell reflection seismic imaging.

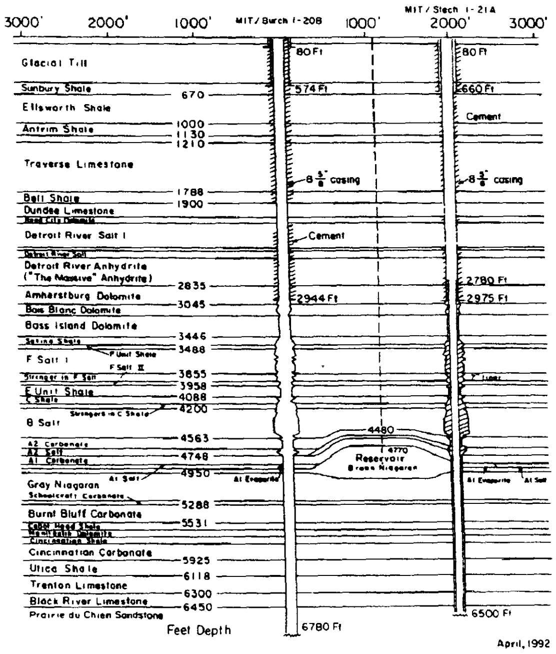

Figure A-11: The structure of the MIT test site according to previous studies.

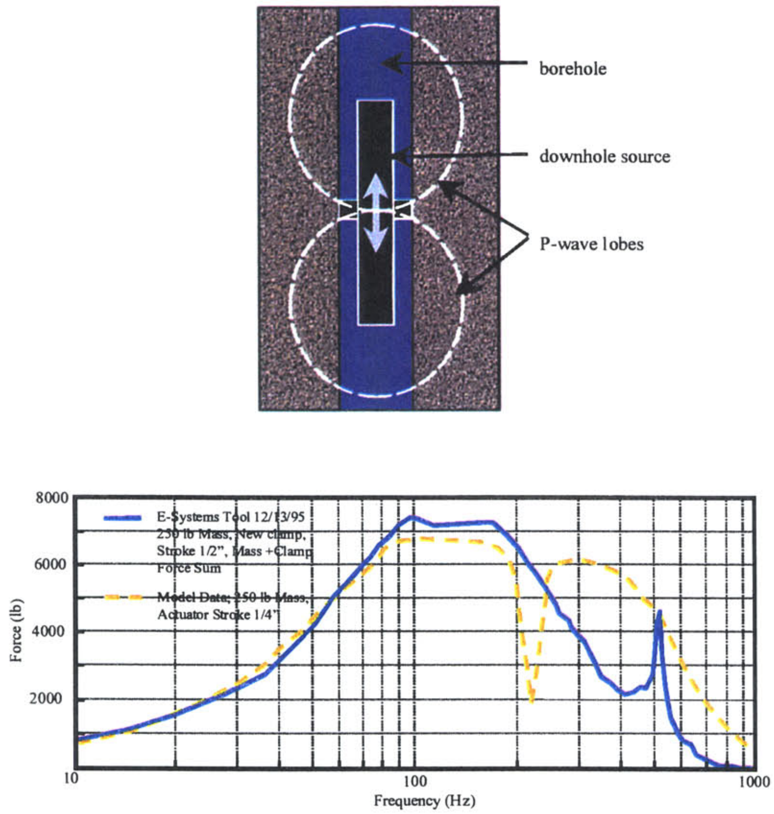

Figure A-12: The Paulsson downhole source.

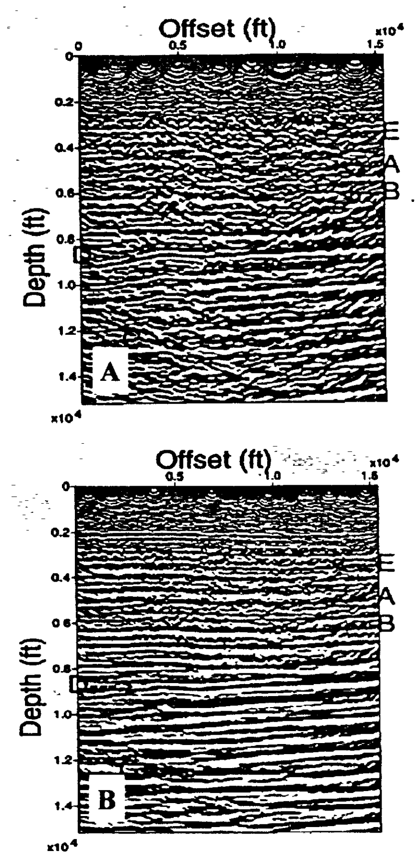

Figure A-13: Higher resolution with a random spread, from Zhou and Schuster (1995). Both plots were made by migrating a 1/4 subsampling of a 3D surface seismic survey. A used a regular subsampling while B was quasi-random. The random spread achieved higher resolution, with more continuity along the reflectors.

Appendix B

Ray tracing in 3D

B.1 Introduction

This appendix describes the ray tracing algorithm which was developed for the imaging process in this thesis, and is aimed towards those who wish to use the software. See Cerveny et al. (1977) for a discussion of ray theory, and Hubral and Krey (1977) for an example of using ray theory to find migration traveltimes.

There are limitations to the method which are discussed below. However, all the code is written in Matlab, which is, in the author's opinion, the easiest type of code to visualize, debug, and, if necessary, rewrite. It should be faster to adjust this software to different needs than to develop an all new ray tracing code.

The following section describes the method used to calculate traveltimes for the migration of the Michigan RVSP data. After that, the ray tracer is discussed more generally.

B.1.1 Travel times in a 1D earth model

The travel time calculation in a flat layered earth model consists of shooting a fan of rays from the surface to the depth of the deepest layer of the grid, as shown in Figure B-3. From these raypaths, the traveltimes, raypath distances, and ray angles within the grid can be interpolated for all of the surface receivers.

Traveltimes from the downhole shot locations were found by shooting similar rays of fans from each shot depth, and interpolating within the grid. For those shots located within the image grid, only the portion of the grid below the shot was used.

Because all the receiver traveltimes can be found from a single set of rays, this method is much faster than the 3D migration. The Michigan RVSP dataset of about 13,000 traces can be migrated with the 1D model into an image grid of over 350,000 elements in about two hours.

B.1.2 Travel times in a 3D earth model

A ray tracing method was used to take advantage of the characteristics of this data set. Because of the simplicity of the earth above reef depth at the test site, a single ray tracing was done from the surface of the earth to the top of the grid. The ray angle, travel time, and path length at this depth were stored as functions of the horizontal distance from the surface to the top of the grid.

For each receiver, an appropriate array of points at the top of the grid were chosen which would illuminate the entire grid. The initial angles, times, and distances were interpolated, then a 3D ray tracer took the rays through the reef structure.

To interpolate from ray coordinates to the regular image grid, travel times were first interpolated for each model layer. Layers with no velocity constrast were added to the model to aid in the interpolation. Then the traveltime was interpolated vertically, filling in between model layers.

Figure B-2 shows the travel time in a slice throught the reef structure in colorscale. Dashed lines show the wavefront every 5 millseconds. Figure B-1 shows the difference between the traveltime through the 3D model and the traveltime through the flat layered model. The difference is neglible above the reef structure, a good sign for the 3D ray tracing method.

B.1.3 Other methods

The travel times can be estimated by other methods. For example, Sayers, 1997 models the travel time by an effective anisotropc model. Model parameters a_i are fitted to the picked first break times t by a trimmed least squares method, where the model is:

$$\begin{aligned} t^2 &= a_1(x-x_r)^2 + a_2(y-y_r)^2 + a_3(z-z_r)^2 \\ &+ \tfrac{a_4(x-x_r)^4}{(x-x_r)^2+(z-z_r)^2} + \tfrac{a_5(y-y_r)^4}{(y-y_r)^2+(z-z_r)^2} \end{aligned} \tag{B.1}$$

for the source position $\mathbf{x}$, and the receiver postion $\mathbf{x_r}$. The a_1, a_2, and a_3 terms are elliptic, while a_4 and a_5 are anelliptic corrections.

B.2 The Ray tracing method

The ray tracing algorithm was developed expressly for the imaging process described in this thesis. The imaging method requires certain information within a 3D image cube:

- First break travel times
- First break ray arrival angles
- Distance traveled along the ray path

- Amplitude due to transmission/reflection (for synthetics)

Accordingly, the goal of the ray tracer is to find these 4 quantities. There are many aspects of wavefield propagation which are neglected, including wavefront spreading, caustics, and multiple arrivals.

The ray tracer outputs information only where rays intersect model interfaces. This information is interpolated to the regular grid needed for the imaging, as discussed in Section B.3. Layers with no velocity contrast can be added to the model to improve the interpolation.

The interpolation process does not allow for multiple arrivals, which is probably the biggest drawback of the method. Only the first arrival is calculated.

B.2.1 Geometry description

The ray tracer assumes that if the $+x$ direction is east, $+y$ is north and $+z$ is downwards, which means that the coordinate system is left-handed. Internally, the ray tracer reverses the sign of the z axis to make the system right-handed, then converts back before outputting the ray paths.

Azimuth angle is measured from the +x axis towards the $+y$ axis, and has the range of $[0^o, 360^o)$. Declineation angle is measured in degrees from the horizontal, with negative angles being downward. So -90^o is straight downward and $+90^o$ is straight up.

B.2.2 Model description and limitations

The model is defined as a multi-valued structure in Matlab-ese. For example, a three layer model could be:

```
    M(1) =
```

```
        x:       [-6000 2000]
        y:       [-5000 5000]
        z:       [2x2 double]
        vp:      3000
        vs:      1500
        rh:      2.4000
        name:    'glacial till'
        lith:    'till'
M(2) =
        x:       [-6000 2000]
        y:       [-5000 5000]
        z:       [2x2 double]
        vp:      8548
        vs:      4050
        rh:      2.5500
        name:    'Shale A'
        lith:    'shale'
M(3) =
        x:       [1x100 double]
        y:       [1x136 double]
        z:       [100x136 double]
        vp:      18200
        vs:      10500
        rh:      2.8000
        name:    'Sandstone B'
        lith:    'sandstone'
```

The x,y,and z fields describe the shape of the interface at the top of the layer with the specified velocities and densities. The last layer is assumed to be an infinite half space. Each layer is assumed to be constant velocity, so there is no ray bending. The lithology field is used in the plotting script lyrvelplt.

Layers can pinch out, but this should be done by making the layer become very thin (1 foot) so that layer overlaps are avoided. Currently there is no part of the program which checks for layer intersections, but the most likely error that would happen in this case is that rays would terminate falsely because they couldn't find the next layer.

If the reflection coefficient becomes complex, or if the ray leaves the defined grid, the ray is terminated. This information is output.

For imaging purposes, only direct rays (as opposed to reflected rays) are needed. But the code can calculate reflections. Direct rays are not allowed to bend back: it is assumed they progress from layer n to layer n+1 to layer n+2 etc. Therefore a model which is highly complex, where a ray may leave a layer and return to it, is outside the realm of this method. The layer interfaces need to be somewhat close to horizontal.

B.3 The Interpolation method

The ray tracer works in two iterated steps; 1) Propagate the ray to an interface; 2) Transmit the ray through the interface. These two steps are repeated until the desired layer is reached.

The output information can be a structure which contains information about the ray at each layer interface. This is useful for making raypath plots. Or, each quantity (traveltime, path length, amplitude, ray angle) can be output separately as matrices. These matrices are used to interpolate the ray information onto a regular grid.

B.4 The Scripts

The ray tracing programs are all written for Matlab 5.3. The ease of debugging and visualizing with Matlab outweighs the slightly longer runtime than one would have with, say, C++ or Fortran.

The scripts used in the ray tracer, as well as a README file which discusses the input and output arguments of each script, should be available at MIT-ERL, or by contacting the author.

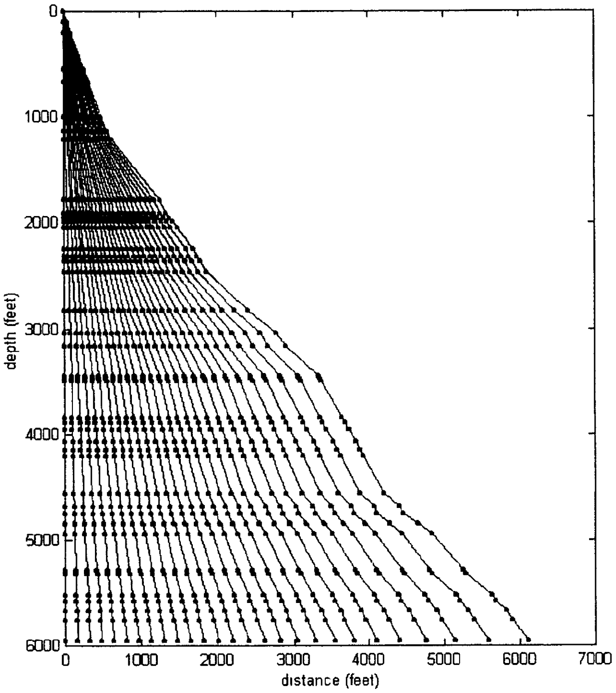

Figure B-1: Ray paths in a flat layered earth. This one set of rays is used to interpolate travel times, ray path distances, and ray arrival angles within the grid for each of the surface receivers.